DISSERTATION

# Paramagnetic States in Organic and Perovskite Solar Cells

## From Chemical Doping to Spin-Dependent Transport


Im Fachbereich Physik der Freien Universität Berlin eingereichte Dissertation zur Erlangung des
Grades eines Doktors der Naturwissenschaften (Dr. rer. nat.)

vorgelegt von

Ula Mehsen Hummadi Yasin

Juni 2019

*1. Gutachter:* Prof. Dr. Jan Behrends
*2. Gutachter:* Prof. Dr. Bernd Rech
*Tag der Disputation:* 17. September 2019

# Abstract

Organic and perovskite solar cells are promising candidates to produce a third generation of high performance, low cost photovoltaic devices. Higher power conversion efficiencies can be achieved, if the fundamental physics of charge transport processes under device operation is understood. In particular charge carrier interactions in their microscopic environment can influence transport and need to be investigated and identified.

This thesis presents a study on paramagnetic states in organic and perovskite solar cells using Electron Paramagnetic Resonance (EPR) spectroscopy in combination with the Electrically Detected Magnetic Resonance (EDMR) technique. Firstly, a doping study on the organic small molecule spiro-OMeTAD, typically used as a hole transport material in perovskite solar cells, is presented. A detailed multi-frequency EPR analysis revealed that the origin of the EPR spectrum of doped spiro-OMeTAD is due to the hole introduced by doping. Doping efficiencies of the most commonly used p-dopants Li-TFSI and FK209 were determined as less than 2% and $\sim$ 81%, respectively, indicating that FK209 is the main doping agent.

A bias-dependent transient EPR and EDMR study on fully processed and encapsulated polymer/fullerene blend bulk heterojunction solar cells was conducted. The combined detection allowed the identification of light-induced spin-species and their involvement in photocurrent influencing processes. We found different spin-dependent processes that dominate at different time scales after optical excitation.

Finally, paramagnetic states in perovskite materials and solar cells were investigated. Spin-dependent processes were detected in the organic transport layers of tin-based perovskite solar cells. Furthermore, from trEPR measurements signatures suggesting the existence of triplet excitons in a two-dimensional perovskite film were found.

# Kurzfassung

Organische und Perowskit-Solarzellen sind vielversprechende Dünnschichtsolarzellen, die eine leistungsstarke und kostengünstigen dritte Generation der Photovoltaik bilden. Ein besseres Verständnis der fundamentalen Transportprozesse der Ladungsträger unter Solarzellenbetrieb ist die Grundlage für weitere Erhöhungen im Wirkungsgrad der Energieumwandlung. Da die Wechselwirkung der Ladungsträger in ihrer mikroskopischen Umgebung den Transport beeinflusst, ist deren Charakterisierung besonders wichtig.

Die vorliegende Arbeit untersucht paramagnetische Zustände in organischen und Perowskit-Solarzellen unter Verwendung der Elektronen Paramagnetischen Resonanz (EPR) Spektroskopie in Kombination mit der Elektrisch Detektierten Magnetischen Resonanz (EDMR) Technik.

Im ersten Kapitel wird die Dotierung des organischen Halbleiters Spiro-OMeTAD, der typischerweise als Lochtransportmaterial in Perowskit-Solarzellen verwendet wird, untersucht. Mittels einer detaillierten Multifrequenz EPR-Analyse, wurde der Ursprung des EPR-Spektrums vom dotiertem Spiro-OMeTAD als Folge des durch Dotierung verursachten Lochs festgestellt. Dotiereffizienzen der am häufigsten verwendeten Dotanden Li-TFSI und FK209 wurden als weniger als 2% für Li-TFSI und $\sim 81\%$ für FK209 bestimmt, was darauf hinweist, dass FK209 der Hauptdotand ist.

Eine spannungsabhängige transiente EPR- und EDMR-Studie an vollständig verarbeiteten und verkapselten Polymer/Fulleren “Heterojunction” Solarzellen wurde durchgeführt. Die kombinierte Detektion ermöglichte die Identifizierung von lichtinduzierten Spinspezies und deren Beteiligung an photostrombeeinflussenden Prozessen. Es wurden verschiedene spinabhängige Prozesse, die nach der optischen Anregung auf verschiedenen Zeitskalen dominieren, bestimmt.

Schließlich wurden paramagnetische Zustände in Perowskit-basierten Materialien und Solarzellen untersucht. Spinabhängige Prozesse wurden in den organischen Transportschichten von Zinn-basierten Perowskitsolarzellen nachgewiesen. Zusätzlich wurde mittels transienten EPR-Messungen an einem zweidimensionalen Perowskitfilm Signaturen, die auf die Existenz von Triplett-Exzitonen schließen lassen, gefunden.

# Contents

# List of Symbols

| | |
|---|---|
| $\alpha$ | Auxiliary mixing angle |
| $\boldsymbol{\mu}$ | Magnetic moment |
| $\Delta\mathbf{g}$ | Shift from $g_e$ |
| $\Delta E$ | Energy difference |
| $\epsilon$ | Energy of electronic level |
| $\hbar$ | Reduced Planck constant, $\hbar = \frac{h}{2\pi}$ |
| $\left\|T_+\right\rangle, \left\|T_0\right\rangle, \left\|T_-\right\rangle$ | High-field triplet eigenfunctions |
| $\left\|T_x\right\rangle, \left\|T_y\right\rangle, \left\|T_z\right\rangle$ | Zero-field triplet eigenfucntions |
| $\mathcal{H}$ | Hamiltonian |
| $\mu_0$ | Magnetic constant, $\mu_0 = 4\pi \cdot 10^{-7}\,\mathrm{N/A}^2$ |
| $\mu_B$ | Bohr magneton, $\mu_B = 927.4009994(57) \cdot 10^{-26}\,\mathrm{J/T}$ |
| $\mu_n$ | Nuclear magneton, $\mu_n = 5.050783699(31) \cdot 10^{-27}\,\mathrm{J}\ /\mathrm{T}$ |
| $\mu_{\mathrm{e/h}}$ | Electron/hole mobility |
| $\nu$ | Frequency |
| $\psi$ | Electronic wavefunction |
| $\rho$ | Density |
| $\sigma_{\mathrm{e/h}}$ | Electron/hole conductivity |
| $\theta$ | Angle between $z$-axis and $xy$-plane |
| $\varepsilon_r$ | Dielectric constant |
| $\underline{\mathbf{D}}, \mathbf{D}$ | Anisotropic dipolar coupling tensor, diagonalized matrix |
| $\mathbf{A}$ | Hyperfine tensor |
| $\mathbf{B}$ | Magnetic field vector |

$\mathbf{g}$ $g$-tensor

$\mathbf{L}$ Orbital angular momentum

$\mathbf{r}$ Position vector

$\mathbf{T}$ Anisotropic component of $\mathbf{A}$

$A_x, A_y, A_z, A_\parallel, A_\perp$ Principal values of $\mathbf{A}$ for rhombic and axial symmetry

$a_{\text{iso}}$ Isotropic hyperfine coupling

$B_m$ Modulation amplitude

$C_t$ Conversion time

$c_{\text{calib.}}$ Calibration constant for the spin-counting routine

$D_x, D_y, D_z$ Principle values of $\mathbf{D}$

$DI$ Double integral

$e$ Elementary charge, $e = 1.6021766208(98) \cdot 10^{-19}\,\text{C}$

$g_e$ Free electron $g$-value, $g_e = 2.00231930436182(52)$

$G_R$ Receiver gain

$g_{\text{iso}}$ Isotropic $g$-value

$g_x, g_y, g_z, g_\parallel, g_\perp$ Principal values of $\mathbf{g}$ for rhombic and axial symmetry

$h$ Planck constant, $h = 6.626070040(81) \cdot 10^{-34}\,\text{Js}$

$I, m_I, \mathbf{I}$ Nuclear spin quantum numbers and nuclear vector

$J$ Exchange coupling constant

$k_B$ Boltzmann constant, $k_B = 1.38064852(79) \cdot 10^{-23}\,\text{J/K}$

$M$ Multiplicity

$m$ Mass

$n_B$ Boltzmann factor

$N_s$ Number of spins

$N_{\text{scans}}$ Number of scans

$P_{MW}$ Microwave power

$Q$ Q-factor

$S, m_s, \mathbf{S}$ Spin quantum numbers and spin vector

$U$ Bias voltage

$V_{\text{film}}$ Film volume

# Acronyms

**BHJ** Bulk Heterojunction

**CT** Charge Transfer
**cw** Continuous wave

**DFT** Density Functional Theory

**EDMR** Electrically Detected Magentic Resonance
**EPR** Electron Paramagnetic Resonance
**ETL** Electron Transport Layer

**FF** Fill Factor
**FK209** tris(2-(1H-pyraxol- 1-yl)-4-tert-butylpyridine)cobalt(III)-(TFSI)3

**HOMO** Highest Occupied Molecular Orbital
**HTL** Hole Transport Layer

**ITO** Indium Tin Oxide

**LCAO** Linear Combination of Atomic Orbitals
**Li-TFSI** lithium bis(trifluoromethylsulfonyl)-imide
**LUMO** Lowest Unoccupied Molecular Orbital

**MAPI** Methylammonium lead iodide

**OSC** Organic Solar Cells

**PCBM** phenyl-C61-butyric acid methyl ester
**PCE** Power Conversion Efficiency
**PEDOT:PSS** Poly(3,4-ethylenedioxythiophene) polystyrene sulfonate
**PSC** Perovskite Solar Cell

**Q-factor** Quality factor

**spiro-OMeTAD** 2,2',7,7-tetrakis(N,N-di-p-methoxyphenylamine)-9,9'- spirobifluorene

**$TiO_2$** Titanium oxide

**ZFS** Zero-field splitting

Chapter 1

# Introduction

Today, the burning of fossil fuels covers more than half of the world energy needs, driving the current global warming crisis with increasing emission of greenhouse gases. The consequences have manifested themselves in form of air pollution, climate change, and disruption of the ecosystem leading to more frequent occurrences of natural disasters. The global energy demand is therefore addressed with renewable resource technologies relying on wind, water and solar power that fulfill "green" and sustainable goals.

One of the promising strategies to produce clean energy while keeping up with the global energy demand is solar energy conversion into electrical power. The sun provides the earth with as much energy every hour as the world consumes in one year [1]. The prospect of utilizing the sun as the main energy source is granted, if photovoltaic devices can be produced, maintained, and operated at lower costs to sustain long-term global demand and consumption [2]. This can be achieved with stable, cheap, and high power conversion efficiency thin-film solar cells.

## 1.1 The Three Solar Cell Generations

The first generation of photovoltaic technology is based on single and multi-crystalline silicon wafers [3, 4]. These are currently the commercially available most efficient solar cells, in terms of incident-to-electrical power conversion. However, this technology is expensive as it requires the growth of high purity crystals, achieved by high temperature processing. The second generation technology are thin film solar cells comprising of cadmium-telluride (CdTe), copper indium gallium selenide (CIGS), or amorphous-silicon (a-Si). These can be produced with less material usage at lower costs. However, their power conversion efficiency is lower compared to their predecessors, the first generation crystalline silicon cells.

The discovery of conductive conjugated polymers in 1977 [5] gave way to the development of new concepts in semiconductor physics. This was followed by the first modern organic donor-acceptor solar cell introduced in 1986 [6] with 1% efficiency. The success of Organic Solar Cells (OSC) emerged after several breakthroughs in

material synthesis including the introduction of the highly soluble fullerene phenyl-C61-butyric acid methyl ester (PCBM) [7] and the concept of polymer donor and fullerene acceptor blended bulk heterojunctions [8]. More than 30 years later a record efficiency of 17.3% was reported by Meng et al. [9] while efforts to further boost performance are ongoing. The newer Perovskite Solar Cell (PSC) emerged from the concept of solid-state dye sensitized solar cells that used organic-inorganic lead halide perovskite compounds as light absorbers [10]. Although the reported device only delivered a 3.8% power conversion efficiency and was stable for just a few minutes, its interesting optoelectronic properties triggered considerable research in the field and led to the first solid-state perovskite photovoltaic device in 2012 [11]. The field has advanced dramatically ever since. To-date, perovskite solar cells achieve a record efficiency of more than 23% [12] realized only within 10 years after their discovery in 2009.

Organic and perovskite solar cells are both thin-film devices processed from solutions with low-temperature deposition methods. They are therefore promising technologies to produce a third generation of high performance, low cost photovoltaic devices. However, despite the major advances in organic and perovskite solar cells, gaps in material and device physics remain. A complete understanding of the fundamental processes on the microscopic level, concerning charge generation, dissociation, and transport paths, still needs to be established and are essential to develop strategies enhancing photovoltaic performance.

## 1.2 About this Thesis

The overall aim of this work is to shed light on fundamental processes in the range of materials and devices studied here, thereby contributing to the improvement of the fundamental understanding of the physics in OSCs and PSCs. In this thesis I focus on the investigation of charge carrier transport and interactions in organic materials used in photovoltaic devices with Electron Paramagnetic Resonance (EPR) spectroscopy and its particular detection mode of Electrically Detected Magentic Resonance (EDMR). EPR spectroscopy uses the magnetic property of charge carriers, namely their spin, to detect the charge carrier state and interactions within its microscopic environment. EDMR gives additional insight into spin-dependent processes the charge carriers might be involved in under device operation. Applying these spectroscopic methods to study organic materials and solar cells aids the investigation of material properties relevant for photovoltaic operation and charge transport. The thesis is structured as follows:

**Chapter 2** outlines the fundamental working principles of solar cells based on the description of a p-n junction. This is followed by the discussion of organic and

perovskite materials with focus on their application in photovoltaic devices. Furthermore, an overview of the physics under device operating conditions is given.

**Chapter 3** presents the principles of spin resonance required for the understanding of EPR and EDMR spectroscopy. Firstly, the interaction of a spin with an external magnetic field, its interaction with nuclear spins, namely the hyperfine interaction, and other electron spins, the spin-spin interaction, is described. Examples of the EPR spectra and their analysis is demonstrated. In the second part of the chapter, the consequence of the electron spin on the charge transport in disordered systems, giving rise to spin-dependent transport, is elucidated. This provides the basis for the concept of EDMR spectroscopy.

**Chapter 4** gives an overview on the preparation of the samples investigated and the experimental methods used in this work. A range of samples, including solution samples, micrometer-thick films prepared from solutions, as well as complete devices prepared on quartz substrates, are studied.

**Chapter 5** presents an EPR study on the doping of the hole transport material 2,2',7,7-tetrakis(N,N-di-p-methoxyphenylamine)-9,9'- spirobifluorene (spiro-OMeTAD), used for PSCs. Doping efficiencies of two commonly used additives lithium bis(trifluoromethylsulfonyl)-imide (Li-TFSI) and tris(2-(1H-pyraxol- 1-yl)-4-tert-butylpyridine)cobalt(III)-(TFSI)3 (FK209) were determined. In the second part of the chapter, the EPR spectrum of doped spiro-OMeTAD in the liquid phase and solid-state environment was analyzed with a multi-frequency EPR approach and DFT-based EPR simulations. The origin of the detected spectrum was identified as the hole introduced by doping and the spectral shape was a result of charge carrier distribution on the molecule.

**Chapter 6** demonstrates a bias-dependent transient (tr)EPR and trEDMR study on an polymer/fullerene bulk heterojunction solar cell. The combined detection allowed the identification of light-induced spin-species and their involvement in photocurrent influencing processes. We found different spin-dependent processes that dominate at different time scales after optical excitation.

**Chapter 7** presents "first results" from spin-dependent processes measured in the organic transport layers of tin-based PSCs. In addition, a two-dimensional perovskite film studied with transient trEPR spectroscopy revealed signatures suggesting the existence of triplet excitons. The challenges and limitations inflicted by the perovskite material within the framework of this thesis are elucidated. The potential of magnetic resonance techniques as a tool to study the perovskite class of materials is discussed.

**Chapter 8** summarizes the relevant results obtained and gives an overall conclusion and outlook on the presented work.

Chapter 2

# Fundamentals of Solar Cells

*In a nutshell, a solar cell converts incoming light into electric power by means of the photovoltaic effect. The process of energy-to-current conversion involves several steps on the microscopic scale in devices of different configurations. The devices discussed are bulk heterojunction solar cells consisting of mainly organic materials and organic-inorganic hybrid perovskite solar cells.*

*The fundamental principles of solar cell physics are best explained considering first and second generation solar cells, which are based on a device architecture that uses a p-n junction. Therefore as the first part of this chapter, the working principle of a p-n junction is described. The important current-voltage (I-V) parameters are summarized. This is followed by the introduction and description of the working principles of organic and hybrid perovskite solar cells and their I-V characteristics.*

## 2.1 p-n Junction

In a simple description, a p-n junction consists of a p-doped and an n-doped semiconductor [13–15]. The p-doped semiconductor has an excess of free holes, while the n-doped semiconductor has an excess in electrons. When the p- and n-type semiconductors are brought into contact, electrons will diffuse from the n- to the p-type, leaving behind positively charged ions. Similarly, the holes flow from the p-type to the n-type, leaving behind negatively charged ions. This diffusion is caused by the imbalance in charge-carrier concentration. As a result a depletion region is formed with fixed space charges on either side of the junction creating an electric field as illustrated in Figure 2.1a. In the depletion region the conduction band and valence band are bent such that the Fermi levels equate across the junction.

Absorption of a photon in a semiconductor creates an electron-hole pair that can potentially dissociate into a free electron and hole. The dissociation of the electron-hole pair is often attributed to the internal electric field of the depletion layer driving them in opposite directions. An alternative explanation for the separation and selective transport of electrons and holes is attributed to different conductivities for each of them in different regions of the device [16]. The conductivity should be large

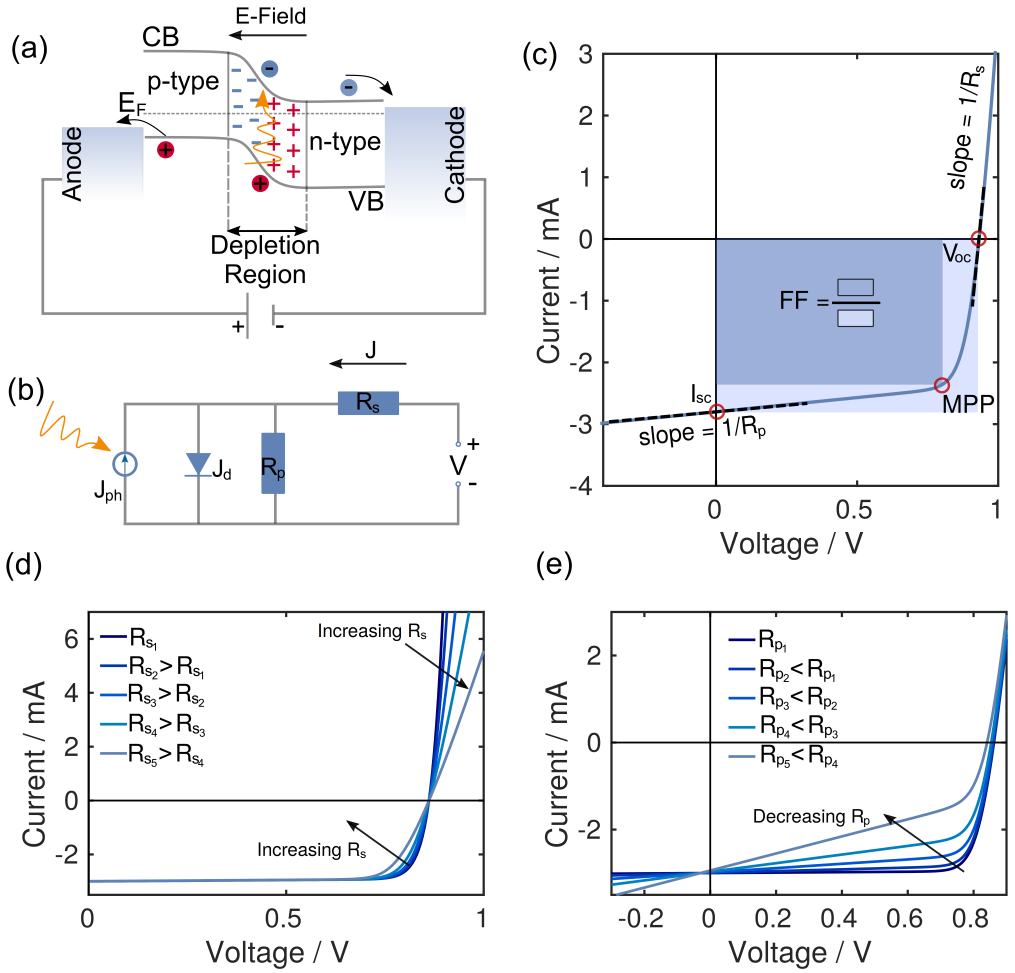


**Figure 2.1:** Fundamentals of a p-n junction: a) Schematic illustration of a p-n junction indicating charge diffusion to the respective electrodes, the resulting band bending and the depletion region b) electric circuit describing a solar cell, c) $I$-$V$ curve to the corresponding circuit of b) indicating the relevant parameters, d) the influence of the series resistance and e) the influence of the parallel resistance on the $I$-$V$ curve.

for electrons and small for holes in the n-type semiconductor and vice versa in the p-type semiconductor. After separation the charges are collected at the electrodes resulting in the generation of a photocurrent.

### 2.1.1 Shockley Equation

Without illumination, the diffusive flow of charge carriers across the depletion layer is described by the Shockley equation. The probability of a hole diffusing from the p-type region to the n-type region depends exponentially on the ratio between the built-in potential barrier that the hole needs to overcome and its thermal energy $k_B T$. The inverse applies for electrons. The total flow of hole (electron) current

from the p- (n-) to the n-type (p-type) area is then given by

$$I(V) = I_0\left(\exp\left(\frac{eV}{\eta k_B T}\right) - 1\right) \tag{2.1}$$

where $V$ is the applied voltage, $e$ is the elementary charge, $k_B$ is the Boltzmann constant and $T$ is the temperature. $\eta$ is the ideality factor which is 1 in the ideal case, but may have values between 1 and 2, if additional parasitic recombination processes take place. $I_0$ is the recombination current at forward bias. The above equation describes the behavior of an idealized ($\eta = 1$) diode under a negative (reverse) and positive (forward) bias.

### 2.1.2 *I-V* Characteristics

Illuminating the p-n junction results in a photocurrent $-I_{\mathrm{ph}}$, which is added to eq. 2.1

$$I(V) = I_0\left(\exp\left(\frac{eV}{\eta k_B T}\right) - 1\right) - I_{\mathrm{ph}} \tag{2.2}$$

giving the current-voltage ($I$-$V$) curve of a solar cell with a Shockley diode behavior shifted by a voltage-independent term $-I_{\mathrm{ph}}$.

In real devices parasitic losses play a major role and their impact is observed in the $I$-$V$ curves. The losses can be modeled as a series resistance $R_S$ and a parallel (shunt) resistance $R_P$ that are added to the Shockley solar cell model:

$$I(V) = I_0\left(\exp\left(\frac{e(V - IR_S)}{\eta k_B T}\right) - 1\right) - I_{\mathrm{ph}} - \frac{V - IR_S}{R_P} \tag{2.3}$$

This equation is known as the generalized Shockley equation. The equivalent circuit of this model is shown in Figure 2.1b. A series resistance can be caused by the contact resistance of the electrodes or the sheet resistance of the semiconductor bulk. The parallel resistance stems from alternative current pathways around the diode. Their impact on the $I$-$V$ curve is demonstrated in Figure 2.1d and e. For $R_P \gg R_S$, $R_P$ can be approximated from the inverse slope of the $I$-$V$ curve at reverse bias. For strong forward bias the internal resistance on the diode approaches 0, allowing the injected current to only go through $R_S$. Therefore the inverse slope in the $I$-$V$ curve at forward bias is a good approximation for $R_S$.

Figure 2.1c summarizes all the relevant parameters to be obtained from the $I$-$V$ curve of a solar cell. This includes the short-circuit current $I_{\mathrm{SC}}$, which is defined as the generated current without applied bias $V = 0$ and is a good approximation for the photogenerated current $I_{\mathrm{ph}}$. The $V_{\mathrm{OC}}$ is the applied bias which compensates for the built-in voltage of a solar cell resulting in a net current flow of zero. In the $I$-$V$

curve it is the point at which the voltage axis is intercepted. Furthermore, the Power Conversion Efficiency (PCE), giving the efficiency with which the solar cell converts the input energy into electrical energy, can be determined. For this purpose, the point at which $V \cdot I(V)$ has maximum power must be determined. This is the the maximum power point with power output $P_{\text{max}}$ and is obtained from the respective current and voltage values $V_{\text{MPP}}$ and $I_{\text{MPP}}$. The PCE is then defined as

$$\text{PCE} = \frac{V_{\text{MPP}} \cdot I_{\text{MPP}}}{P_0} \tag{2.4}$$

with $P_0$ as the incident-light power. In addition, the ratio of maximum power and $V_{\text{OC}} \cdot I_{\text{SC}}$ is defined as the Fill Factor (FF). It is obtained graphically from the largest area of a rectangle which will fit in the $I$-$V$ curve.

$$\text{FF} = \frac{V_{\text{MPP}} \cdot I_{\text{MPP}}}{V_{\text{OC}} \cdot I_{\text{SC}}} \tag{2.5}$$

When improving solar cell performance, one aims to achieve fill factors close to unity.

## 2.2 Organic Solar Cells

This section introduces the basic concepts of organic semiconductors and their application in solar cells. The working principles of Organic Solar Cells (OSC) and significant aspects in the $I$-$V$ characteristics are summarized and compared to inorganic solar cells. Only the operational principles of organic Bulk Heterojunction (BHJ) are considered.

### 2.2.1 Introduction to Organic Semiconductors

Organic semiconductors are materials containing mostly carbon (C) and hydrogen (H) atoms with semiconductor properties [14, 17–19]. They are based on $\pi$-conjugated systems: a chain of C atoms with alternating single and double bonds or repeating chemical units such as the aromatic ring and often include N, O, or S atoms.

As can be explained on the basis of a simple system of two chemically-bound carbon atoms, a double bond involves an $sp^2$ hybridization at each C atom. The $s$ and two $p$-orbitals hybridize to give three orbitals located in one plane and at angles of 120° to each other, which form $\sigma$ bonds. The remaining $p$-orbital, usually designated as $p_z$, is oriented perpendicular to the plane and forms the additional $\pi$-orbital. Since the electrons are shared by the atoms, they are equally probable to be found orbiting around one carbon atom as around a second. Therefore, they cannot be assigned to atomic orbitals, but instead need to be associated with molecular orbitals. Molecular orbitals can be approximated by a Linear Combination of Atomic

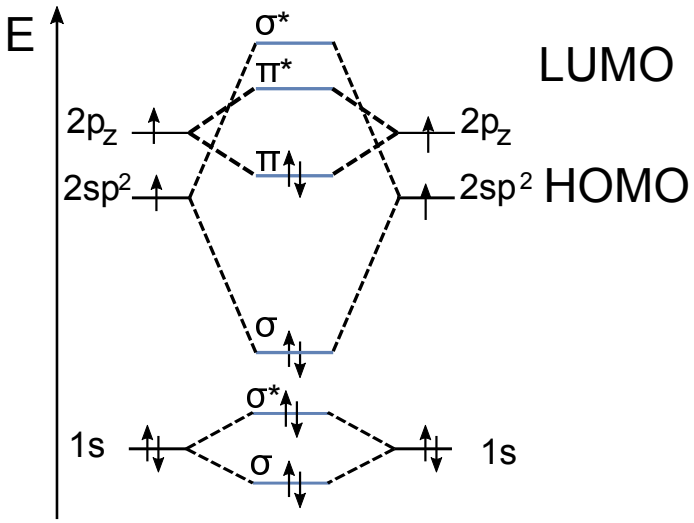


**Figure 2.2:** Energy level diagram illustrating the $\pi$ and $\sigma$ bonds from atomic orbitals in the carbon-carbon interaction. Figure adapted from [14].

Orbitals (LCAO). Figure 2.2 illustrates the resulting molecular orbitals, when considering the interaction of the $2sp^2$ hybrid and the $2p_z$ orbitals of two carbon atoms. As indicated above, the $sp^2$ hybridized atomic orbitals give rise to a bonding $\sigma$ and antibonding $\sigma^*$ molecular orbital, while the $p_z$ orbitals result in $\pi$ and $\pi^*$ molecular orbitals. The Highest Occupied Molecular Orbital (HOMO) is the $\pi$ orbital and the Lowest Unoccupied Molecular Orbital (LUMO) is $\pi^*$ orbital. From this picture it becomes clear that the fairly small energy difference between $\pi$ and $\pi^*$ implies that less energy is required for the excitation of electrons from the HOMO to the LUMO compared to excitation from $\sigma$ to $\sigma^*$. For large conjugated $\pi$ orbitals that extend over several carbon atoms, this energy lies in the visible spectrum [14]. While the transition $\sigma \rightarrow \sigma^*$ is typically in the ultraviolet spectral range.

If one considers a large chain of repeat units that are covalently bound such as in polymers, the conjugation length is typically limited, due to a disordered conformation with bends, kinks and coils. This divides the chain in segments of different lengths as chromophores with their own energy levels and HOMO-LUMO gaps. Chromophores contain well defined discrete energy levels. Averaging over all possible conformations will results in a broad distribution of energy values. Statistically this can be described by a Gaussian distribution which sums up to form a continuous density of states for the HOMO and LUMO levels. Large conjugation implies large delocalization and this in effect reduces the HOMO-LUMO energy gap $E_{\text{gap}}$.

Furthermore, chromophores are intermolecularly bound by van der Waals forces, causing interactions between neighboring chains to be weaker compared to inorganic semiconductors. Consequently, the electronic wavefunctions become weakly delocalized and optical excitations are then usually localized on one molecule or along an extended chain segment. This weak delocalization, moreover, impacts charge trans-

fer and mobility in conjugated polymers [19], as will be discussed in later sections. Therefore, the optoelectronic properties (e.g. energy levels, $E_{\text{gap}}$, and mobility) of conjugated polymers mostly rely on the repeat units that make up the conjugated backbone.

### 2.2.2 Working Principles of OSC

Many organic semiconductors exhibit absorption coefficients above $10^7\,\text{m}^{-1}$, making them promising compounds for thin-film photovoltaic applications [18]. In this section the working principles of an organic solar cell are elucidated with the example of an organic BHJ solar cell.

The absorption of a photon and the creation of an electron-hole pair (exciton) takes place on a chain segment of the polymer. The electron-hole pair is strongly Coulombically bound, due to a significantly low dielectric constant $\epsilon_r \approx 3-4$ [14]. This means that the binding energy of the electron-hole pair exceeds the thermal energy at room temperature [20] and an additional force is required to separate them. The nature of the exciton is of Frenkel type. In addition, due to the charge polarizing its environment causing distortions in its surroundings and due to the morphological disorder in the polymer, the exciton diffusion length is in the short range of $5-20\,\text{nm}$ [19, 21, 22]. Hence the BHJ concept was designed to overcome the drawbacks of short exciton diffusion lengths and their high binding energies [8]. The bulk photoactive layer entails the intermixing of donor and acceptor materials as a blend and thereby maximizes the donor-acceptor interfaces. The advantages are that the charge carriers are bound to encounter an interface within their diffusion length allowing most photogenerated charge carriers to be separated. Typically, the bulk material consists of a polymer donor blended with a fullerene acceptor. The device configuration is illustrated in Figure 2.3. The enlarged schematic of the photoactive layer summarizes the fundamental processes (i) exciton generation, (ii) diffusion to the interface and charge transfer, (iii) dissociation and recombination, and finally (iv) their transport to and extraction at the electrodes. These steps are introduced and followed by the discussion of the energetic landscape of the device.

#### (i) Exciton Generation

For simplicity we assume the absorption of an incident photon mainly occurs in the polymer and results in the generation of a strongly coupled electron-hole pair. The electrically neutral exciton in the polymer requires an electronegative acceptor material in order to dissociate in to free charges.

#### (ii) Diffusion and Charge Transfer

In the next step, the exciton diffuses towards the donor-acceptor interface. As it reaches the interface, the electron is transferred from the donor phase to the electronegative acceptor. Dissociation occurs only if the energy gain is larger than the

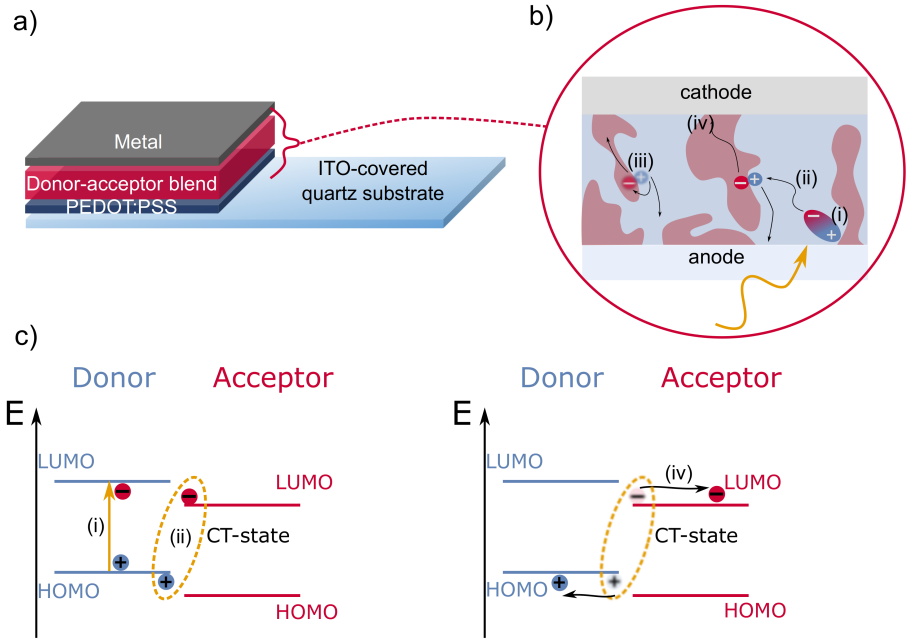


**Figure 2.3:** BHJ organic solar cell a) Illustration of the device cell configuration as used for this thesis, with the bulk material consisting of a blend b) of a donor (blue) and acceptor (red) material. The processes occurring during solar cell operation from (i) photon absorption and exciton generation, (ii) diffusion, (iii) dissociation and recombination, to (iv) extraction are illustrated. c) Schematic representation of processes (i),(ii), and (iv) on an energy level diagram of the donor-acceptor system. Figure adapted from [19, 20].

exciton's binding energy and is facilitated by the energy level difference of the HOMO ($\Delta E_{\mathrm{HOMO}}$) of the donor and acceptor, as well as between their LUMO ($\Delta E_{\mathrm{LUMO}}$) levels. Consequently, it becomes energetically favourable for the electron to be transferred to the acceptor molecule. However, recently it has been shown that organic BHJs based on non-fullerene acceptors do not require this energy offset for charge transfer from the donor to the acceptor to occur [23–25]. The exciton transfers into an intermediate state known as Charge Transfer (CT) state, where the hole resides on the polymer and the electron on the acceptor near the interface. The two charges are still bound, due to the weak screening of the electric field in organic semiconductors. In addition, the electron and hole polarize their environment, causing distortions in the molecular surroundings. Therefore the charge including its induced distortion is defined as a quasi particle, polaron.

### (iii) Dissociation and Recombination

At the CT state the polarons can evolve in two ways: they can either recombine or dissociate. As mentioned, the polarons are still Coulombically coupled at the CT state. In order to dissociate the pair, the Coulomb attraction needs to be overcome for instance by an electric field or the energetic disorder in organic semiconductors. This is manifested in the strong field and temperature dependent photocurrent of

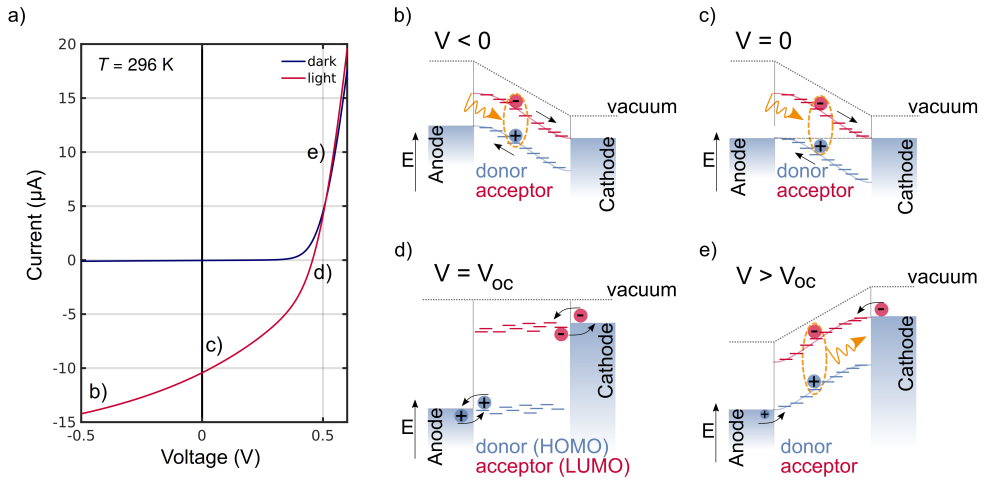


**Figure 2.4:** The working principles of a bulk-heterojunction OSC: a) the $I$-$V$ characteristics measured at room temperature under dark conditions and illumination and b)-e) schematic energy diagrams for different biasing conditions, where b) indicates reverse bias, c) without an applied voltage, d) under application of $V = V_{OC}$, and e) under forward bias $V > V_{OC}$. The implications of the biasing regimes are described in the text. Band diagram adapted from [14].

organic solar cells [20]. In the case of the Coulomb attraction prevailing, the charge carriers recombine. Recombination is a loss mechanism and is defined as the annihilation process of two charge carriers, namely an electron and a hole, which proceeds radiatively or nonradiatively.

#### (iv) Transport and Extraction

Once the exciton is dissociated and the electron and hole are spatially separated, they travel through the acceptor and donor materials towards the respective electrodes. As organic semiconductors are disordered materials with a short-range order, transport takes place by hopping of charge carriers from one localized state to the next.

The extraction of charges takes place at the contacts, where electrons leave the device at the cathode, while the holes are extracted at the anode. The generated photocurrent has a major impact on the $I$-$V$ characteristics and will be summarized in the next section.

### 2.2.3 $I$-$V$ Characteristics of Organic Solar Cells

Similar to the previously discussed p-n junction, in order to determine the power conversion efficiency of an OSC, the three characteristic points MPP, $I_{SC}$, and $V_{OC}$ are required. The $I$-$V$ curve of an BHJ OSC is shown in Figure 2.4 under dark conditions and under illumination. By comparison, the shape of the $I$-$V$ curves in

Figure 2.1c-e flattens towards reverse bias and takes on a more or less rectangular form in the fourth quadrant. This is different for OSCs, where the curve's shape is influenced by the shift in energy levels for specific applied voltages. The effect of the applied voltage on the energy levels is shown in Figure 2.4 b-e.

The scenario shown in Figure 2.4b occurs once applying a negative voltage $V < 0$, biasing the OSC in reverse. It causes the Fermi level of the cathode to be lowered with respect to the Fermi level of the anode. The HOMO of the donor and LUMO of the acceptor are tilted towards the electrodes such that the hole moves up in energy towards the anode and the electron moves down in energy towards the cathode and charge extraction can take place. The tilt of the energy levels is steeper than at $V = 0$ and the energy barriers at the electrodes will also be high enough preventing injection of charges into the solar cell.

Without any applied voltage ($V = 0$), short circuit conditions are reached (shown in Figure 2.4c) with the short circuit current $I_{SC}$. In an ideal device discussed in section 2.1.2, this will be the maximum generated photocurrent. However, due to the field dependence in OSCs, the maximum photocurrent is reached under reverse bias. Under short-circuit conditions, the workfunctions of the electrodes remain unaltered. The charges will flow towards the respective electrodes until their Fermi energies are equilibrated.

If an external voltage is applied that compensates for the built-in potential across the organic layer, open circuit conditions are reached ($V = V_{OC}$). The built-in potential is the potential drop resulting from the difference in electrode workfunctions. The energy levels align as in Figure 2.4d and ideally no net current flows through the device, as the generated charges cannot be extracted. In practice however, charge injection can take place at the electrodes.

Increasing the applied voltage beyond $V_{OC}$ changes the direction of the HOMO and LUMO tilt. This is displayed in Figure 2.4e and is known as forward bias ($V > V_{OC}$). At this biasing regime, electrons and holes are injected from the electrodes into the organic layer. Once the opposite charges meet, they can recombine radiatively and the device can operate as an organic light emitting diode.

Organic solar cells sometimes show an S-shaped deformation of the device $I$-$V$ characteristic, instead of an exponential behaviour as expected for diode structures. This effect can be ascribed to energetic barriers [26, 27] that can form at (i) metal-organic junctions and at (ii) the planar semiconductor heterojunction.

#### (i) Metal-Organic Interface

(i) At the metal-organic junction, the difference between the metal Fermi level and the semiconductor LUMO level defines the intrinsic electron concentration. Electrons that pass this interface are limited by an extraction rate, also known as surface recombination rate, that describes the restrictions on the charge extraction process.

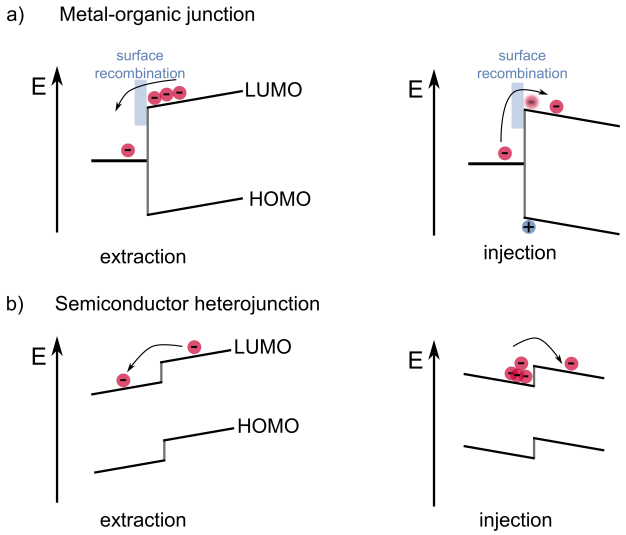


**Figure 2.5:** Generation of space-charge region depending at a) semiconductor heterojunction and b) metal-organic interface. Figure adapted from [26].

If this rate is reduced, it is compensated by additional charges at the junction to maintain a constant flowing current. If under extraction conditions (Figure 2.5a), more charges are transported toward the interface than can be extracted, the charges will pile up, creating a voltage-dependent space-charge region. Under injection conditions, the injection of charges is reduced due to surface recombination, creating a local depletion zone at the interface.

#### (ii) Semiconductor Heterojunction

The interface of the planar semiconductor heterojunction is defined by the energy difference between the LUMO levels and the HOMO levels of the different semiconductors as shown in Figure 2.5b. Due to the direction of band bending at extraction biases, the electrons can hop to an energetically lower and hence more favorable state, crossing the interface. Changing the polarity of the applied voltage going to the injection regime, the bands bend in the other direction. This causes an energetic barrier that the electrons are forced to overcome. Here the electrons pile up and, as well, cause a local space charge that creates an S-shaped $I$-$V$ curve.

## 2.3 Doping of Organic Semiconductors

Doping of organic semiconductors has become a routine process in labs, due to the facile processability from solutions, their low-cost producibility and potential in improving performance of optoelectronic devices. Despite this, little is known about the fundamental doping mechanism in organics, raising two key questions: what is

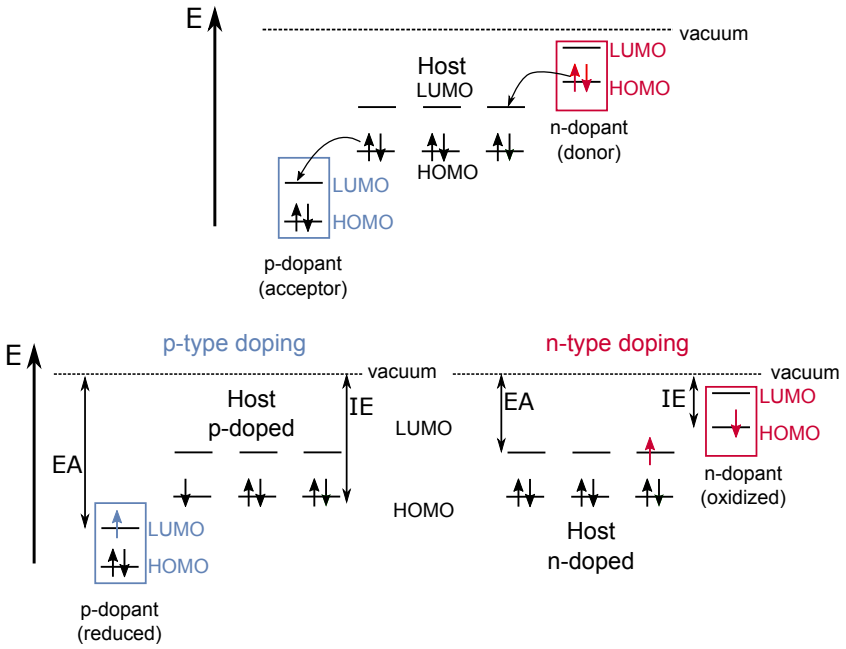


**Figure 2.6:** Schematic illustration of n-type and p-type doping of a host (organic semiconductor) material. Figure adapted from [32].

the nature of the generated charge (polarons, bipolarons, free carriers or strongly bound complexes) and how efficiently does a dopant generate these charges [28].

In contrast to their inorganic counterparts, doping in organic semiconductors is based on a charge-transfer reaction. There are two proposed fundamental processes of doping: (i) the formation of a ground-state charge transfer complex and (ii) charge transfer in a redox reaction. The former doping process is based on the hybridization of the dopant and the organic semiconductor orbitals, forming a new set of occupied bonding and unoccupied anti-bonding molecular orbitals [29–31] similar to Figure 2.2. This was experimentally shown in F4TCNQ doped pentacene [30] amongst other organic semiconductors.

The latter mechanism applies to many cases and is based on a charge-transfer reaction between the organic host and the dopant. This mechanism is illustrated as a schematic in Figure 2.6. It is assumed that the host material is in its neutral ground state. This is indicated in Figure 2.6 in the top middle. The host molecule can be doped by either removing an electron from it, p-type doping (follows the blue scheme), or adding an electron to it, n-type doping (follows the red scheme). For such charge transfer reactions to occur, the acceptor's electron affinity (EA) should be lower in energy than the host molecule's HOMO, while the donor's ionization energy (IE) must be higher in energy with respect to the host's LUMO. In the case of n-type doping, an electron is transferred from the donor material to the host. This leaves the host negatively charged (n-doped) and the dopant in an oxidized state. Conversely, if an electron is taken away from the host, it will leave a hole

behind and hence the molecule is positively charged (p-doped). The p-dopant is left in a reduced state. The introduction of additional charges alters the chemical and electronic properties of the organic semiconductor. Excess charges result in an increased charge carrier density $n$ and hence affect the conductivity $\sigma$ of the material according to eq. 2.6,

$$\sigma_{\mathrm{e/h}} = e \cdot n_{\mathrm{e/h}} \cdot \mu_{\mathrm{e/h}} \tag{2.6}$$

where $e$ is the elementary charge and $\mu$ is the charge carrier mobility. The index represents the type of charge either being an electron (e) or hole (h). It is generally assumed that the charge carrier density is proportional to its conductivity, while the mobility remains constant. Therefore a common method to determine the level of doping is by measuring the materials conductivity with respect to the doping concentration. However, it has been shown that the charge carrier mobility is affected by doping and can either increase or decrease [33–35] and will be topic of discussion in this work.

## 2.4 Perovskite Based Solar Cells

Recently, solar cells based on an organo-metal halides, known as perovskite, have shown great promise as next generation solar cells. Perovskite based solar cells carry the benefits of OSC, e.g. facile and inexpensive production, yet have shown higher PCEs in less than 10 years of research, with growing effort and potential to further boost their performance. In this section the materials for the perovskite building block are introduced and a brief overview on the significant optoelectronic properties is given. The different device architectures and relevant materials are described.

### 2.4.1 Introduction to Perovskite Materials

Historically, perovskite refers to a class of materials that follow an $ABX_3$ stoichiometry as shown in Figure 2.7a. The perovskite crystal structure can adopt different phases depending on the temperature. The extensively studied state-of-the-art perovskite Methylammonium lead iodide (MAPI) ($CH_3NH_3PbI_3$) is in the tetragonal phase at room temperature, with increasing crystal symmetry at higher temperatures adopting the cubic structure (Figure 2.7a). It adopts the orthorhombic structure at temperatures lower than room temperature.

In the field of perovskite based photovoltaics, the perovskite is a mixture of organic-inorganic compounds, which acts as the light harvesting material. In its most commonly used composition for solar cells, the lead ($B$) and halide ($X$) atoms form the inorganic octahedral acting as the anion, while the organic cation resides in the interstices ($A$). Commonly, small cations such as methylammonium ($CH_3NH_3$) are

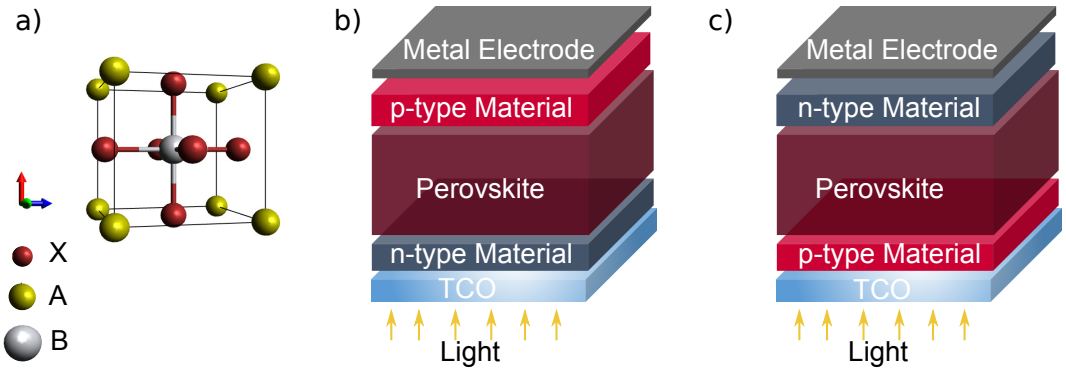


**Figure 2.7:** The perovskite structure in the cubic phase and solar cell configurations. a) The crystal lattice with the $ABX_3$ stochiometry. b) Planar n-i-p perovskite solar cell and c) p-i-n architecture of a perovskite solar cell.

used as the organic compound, however a combination of multiple cations including formamidinium (FA) and caesium (Cs) and anions ($Br^-$, $I^-$, and $Cl^-$) are recently generating higher efficiency solar cells [36].

MAPI is a direct bandgap material with a strong absorption coefficient, due to the high lead (Pb) $p-p$ optical transition probability and sharp absorption edge [37]. Its valence band maximum is a hybridization of the I $5p$ orbitals and Pb $6s$ orbitals and the conduction band minimum is mainly formed by the Pb $6p$ orbitals [38]. The bandgap of $CH_3NH_3PbI_3$ is around 1.55 eV with an absorption onset at 800 nm. The bandgap can be tuned by mixing in different halides [39, 40] and replacing the cation on cite $A$ in Figure 2.7a by a larger cation [41, 42]. The size of the organic cation alters the inorganic framework, which in turn is responsible for the size of the band gap.

Upon photoexcitation in the perovskite material, Wannier-Mott excitons are created with binding energies in the $37-50$ meV range (at room temperature) [43–45]. In contrast, the nature of excitons in organic semiconductors are of Frenkel type, due to their significantly large binding energies, in the range of $0.1-2.0$ eV, as a result of the low dielectric constant. Oppositely, the dielectric constant of perovskite is larger ($\varepsilon_r \approx 18$) [46], leading to weakly bound excitons, that can split into free electrons and holes.

Furthermore, remarkably long charge carrier diffusion lengths, often larger than 1 $\mu$m, were reported for perovskite films [47, 48]. It is debated whether the diffusion lengths depends on the film morphology. It was shown that by increasing the grain size to the thickness of the polycrystalline perovskite film, carrier diffusion lengths could be increased. In single crystals, diffusion can extend to more than 175 $\mu$m [49].

### 2.4.2 Device Architecture

The perovskite layer is capable of ambipolar charge transport, meaning that it can transport both electrons and holes [50]. This depends on the junction it forms with the neighboring material and allows the separation of charges at both interfaces. Commonly, the cell architecture is a n-i-p junction, where the perovskite acts as the absorber layer. It is sandwiched between a Hole Transport Layer (HTL), a p-type semiconductor and an Electron Transport Layer (ETL), which is of n-type. These materials extract the respective photogenerated charge carriers from the perovskite layer and function as selective transport pathways to the electrodes.

Historically, halide perovskite solar cells were derived from dye sensitized solar cells using a mesoporous Titanium oxide ($TiO_2$) structure [10]. The perovskite infiltrates the $TiO_2$, which functions as the electron contact. However, due to the long diffusion lengths of charge carriers and the ambipolar nature of the perovskite, the planar structure prevailed. It can be divided in two classes depending on the selective contact used at the bottom: regular (n-i-p) and inverted (p-i-n), as shown in Figure 2.7a and b respectively. While the n-i-p junction was adapted from dye sensitized solar cells, the inverted structure is derived from the OSC, as the organic transport layers used in OSC were successfully transferred to PSCs [51].

#### n-i-p Junction

The transport-layer/perovskite interfaces play a key role in the performance of the solar cell. The typically used ETLs for the n-i-p cell architecture are metal oxides such as $TiO_2$ and tin(IV) oxide ($SnO_2$), because of their close to ideal charge selectivity and high charge carrier mobility [52–54]. The n-i-p architecture predominantly uses spiro-OMeTAD as the HTL.

Perovskite solar cells in the n-i-p architecture can exhibit PCEs exceeding 23% and high $V_{OC}$, however due to the high processing temperature and the rigid metal oxide as the ETL they are not suitable for flexible devices. Furthermore, conventional PSCs often have a pronounced hysteresis behavior in the $I$-$V$ characteristics. This will be explained in the following section.

#### p-i-n Junction

Inverted architecture devices are processable on flexible devices at low temperatures and are potentially suited for industrial upscaling and low cost production. In the p-i-n architecture, fullerenes and their derivatives are typically used as ETLs, due to their efficient electron transporting properties and solution processability. The fullerene/electrode contact is improved by adding a buffer layer between fullerene and electrode. Furthermore, an Ohmic contact can be improved by employing a combination of metal oxides and fullerenes [55] as an electron transport layer.

Poly(3,4-ethylenedioxythiophene) polystyrene sulfonate (PEDOT:PSS) is often the hole transport material of choice in the p-i-n architecture because it provides a smooth surface on the ITO electrode. The drawback of PEDOT:PSS is its inefficient electron-blocking properties, required to reduce parasitic recombination, and the high acidity that corrodes the ITO and perovskite, limiting the stability and performance of the solar cell [56, 57]. Furthermore, inverted devices with PEDOT:PSS as an HTL show low $V_{OC}$ and $I_{SC}$, which is due to recombination losses. The application of alternative polymers [58, 59] or the modification of PEDOT:PSS [53, 59–62] is a crucial step to improve long-term stability and enhance efficiencies in PSCs.

### 2.4.3 Hysteresis

Perovskite based solar cells often convey a slow transient response that severely influences the current-voltage characteristics. These slow transients result in a hysteresis behavior between *I-V* measurements that are performed with different scan rates and in different voltage-scan directions [63, 64]. Substantial work has been devoted to understand this phenomenon and was attributed to a number of factors.

Various reports have shown that the hysteresis effect is negligible in inverted planar structures (p-i-n cell configuration) with fullerenes as electron transport layers [53, 65, 66]. This was explained by the $I^-$ ion migration: the fullerene and iodine may interdiffuse during fabrication. By interaction of mobile ions in the perovskite with the fullerene, a fullerene-halide radical is formed [67]. This radical reduces the ion-migration produced by the electric field (responsible for hysteretic behavior), and hence suppresses the hysteresis.

In addition, the quality of perovskite layer plays a key role in the degree of hysteresis. Cells with large crystals having few grain boundaries in the absorber layer exhibit little to no *I-V* hysteresis [68, 69]. It is also related to the density of trap states, that serve as recombination channels [70]. Hence, high-performing PSCs are likely to show little or no hysteresis due to low density of traps.

Chapter 3

# Basics of Spin Resonance

*Organic semiconductors have several advantageous properties that make them suitable for investigations with spin resonance techniques. From the practical point of view, they consist of light atoms that have weak spin-orbit couplings, which allows for long charge-carrier spin coherence and relaxation times [71]. In addition, due to the weak dielectric constant, the charge carriers strongly interact with their environment. The charge polarity influences the surrounding such that it is not sufficient to view the charge carrier as an entity of its own, but instead needs to be considered as a quasi particle that polarizes its surroundings: the polaron. Therefore, if found in a paramagnetic state, the polaron spin can provide clues on its the microscopic environment. This furthermore includes, its transport through material, which is, as will be explained, spin dependent. For the fundamental understanding of how the spin of charge carriers is utilized to investigate the physical properties of organic semiconductors, the theory of electrons inside a magnetic field needs to be understood and is the aim of this chapter. In the first part, the spin property of the electron is introduced together with the quantum mechanical description of it inside a magnetic field. In addition, the coupling to other electron and nuclear spins will be explained. This provides the basis for understanding EPR spectroscopy and analysis of EPR spectra, which will be explained after. In the second part of this chapter, the spin-pair model together with spin-dependent processes are elucidated. They provide the foundation for the concept of electrically detected magnetic resonance spectroscopy.*

## 3.1 Electron in a Magnetic Field

In addition to its elementary charge, an electron possesses an intrinsic "angular momentum" termed spin $\mathbf{S}$ [71–76]. It is characterized by a quantum number $S = 1/2$ and an associated magnetic moment $\boldsymbol{\mu}_e$. Their relation is given by

$$\boldsymbol{\mu}_e = -g\mu_B\mathbf{S} \tag{3.1}$$

where $g$ is the Landé factor, also known as the $g$-factor or $g$-value and $\mu_B$ is the Bohr magneton. The electron spin can take on the two states $\alpha$ and $\beta$, that have different orientations but are equal in magnitude. In the presence of a magnetic field, the energy of these states will depend on the direction of $\boldsymbol{\mu}_e$ with respect to the magnetic

field. Therefore, the Hamiltonian of a spin-1/2 particle inside a magnetic field $\mathbf{B}$ is given by:

$$\mathcal{H} = -\boldsymbol{\mu}_e \cdot \mathbf{B} = \frac{g\mu_B}{\hbar}\mathbf{B} \cdot \mathbf{S} \tag{3.2}$$

By convention the axis of the applied magnetic field is chosen in the $z$ direction, simplifying equation 3.2 to:

$$\mathcal{H}_z = \frac{g\mu_B}{\hbar}B_z S_z \tag{3.3}$$

The orientation of $S_z$ is either parallel $|\uparrow\rangle$ or antiparallel $|\downarrow\rangle$ to the applied field, represented by the magnetic quantum number $+m_s$ or the spin state $\alpha$ for the former and $-m_s$ or $\beta$ for the latter. This means that in the presence of a magnetic field, there exists an energy difference between the two possible spin states, which depends on the strength of the applied field. This is given by the equation:

$$\Delta E = g\mu_B B_z \tag{3.4}$$

The splitting of the electron spin states inside a magnetic field is called the Zeeman effect and the Hamiltonian of equation 3.2 describes the electron Zeeman interaction. In disordered systems, such as in organic semiconductors, spins undergo interactions with their environment, neighboring nuclei and other electron spins and need to be considered in the static spin Hamiltonian. The relevant interactions within the scope of this work will be explained in the following sections.

### 3.1.1 The Electron Zeeman Interaction

In systems with particles of spin $S = 1/2$, the electron Zeeman interaction governs the static spin Hamiltonian. The free electron with its angular momentum $\mathbf{S}$ has a $g$-value $g_e = 2.002319$ [77]. This $g$-value is expected for systems of non-degenerate electronic ground states, where the orbital angular momentum $\mathbf{L} = 0$. In systems where this is not the case, an interaction exists that mixes $\mathbf{L}$ from the excited states into the ground state causing $g$-values to deviate from $g_e$ and the orientation dependence of the electron Zeeman term. The Hamiltonian describing this effect is given by:

$$\mathcal{H}_{\text{elec.Z}} + \mathcal{H}_{LS} = \frac{\mu_B}{\hbar}\mathbf{B}(\mathbf{L} + g_e\mathbf{S}) + \lambda\mathbf{L} \cdot \mathbf{S} \tag{3.5}$$

where $\mathcal{H}_{LS}$ is the spin-orbit interaction with the spin-orbit coupling constant $\lambda$. In a second order perturbative treatment this yields the $g$-matrix

$$\boldsymbol{g} = g_e\mathbb{1} + \boldsymbol{\Delta g} \tag{3.6}$$

and $\boldsymbol{\Delta g}$ represents the shift from $g_e$, with its elements given by

$$\Delta g_{i,j} = \frac{\langle\psi_0|L_i|\psi_n\rangle\langle\psi_0|L_j|\psi_n\rangle}{\epsilon_0 - \epsilon_n} \tag{3.7}$$

Here, $\langle\psi_0|$ and $\langle\psi_n|$ represent the ground state of the unpaired electron and its $n$th excited state with their corresponding energies $\epsilon_0$ and $\epsilon_n$.

Equation 3.5 denotes that the stronger the spin-orbit coupling, the larger the deviation from $g_e$ becomes. Systems with weak spin-orbit couplings such as organic semiconductors exhibit small shift from $g_e$ in the order of $\Delta g \sim 10^{-4} - 10^{-3}$ [78, 79]. For compounds consisting of heavier elements such as the perovskite material, larger divinations from $g_e$ are expected, due to the strong spin-orbit coupling [80, 81].

Furthermore, the orientation dependence of the Zeeman interaction inside the magnetic field is included in the $g$-matrix described by the three principle values $g_x$, $g_y$ and $g_z$:

$$\boldsymbol{g} = \begin{pmatrix} g_x & 0 & 0 \\ 0 & g_y & 0 \\ 0 & 0 & g_z \end{pmatrix} \tag{3.8}$$

representing the coordinate system of the paramagnetic state and is typically considered as the molecular frame. The local symmetry at the paramagnetic state can be classified in three categories: cubic symmetry, $g_x = g_y = g_z$, axial symmetry, $g_x = g_y = g_\parallel$ and $g_z = g_\perp$, and for orthorhombic symmetry, $g_x \neq g_y \neq g_z$. In isotropic systems of high symmetry (cubic symmetry), the $g$-value is independent of the magnetic-field direction and the average value

$$g_{\text{iso}} = 1/3(g_x + g_y + g_z) \tag{3.9}$$

is observed.

### 3.1.2 Electron Paramagnetic Resonance

In an EPR experiment an externally applied magnetic field is used to induce the Zeeman interaction removing the degeneracy between substates. The energy difference between these states is given by equation 3.4 which is proportional to the magnetic field strength. Transitions between the two sublevels must obey the selection rule $\Delta m_s = \pm 1$. These transitions are driven by electromagnetic radiation of energy $E = h\nu$, where $\nu$ is the frequency of the electromagnetic field. For a magnetic field applied in $z$ direction, $B_z$, the resonance condition

$$\Delta E = g\mu_B B_z \Delta m_s = h\nu \tag{3.10}$$

is fulfilled once the energy of the radiation is equivalent to the Zeeman splitting and shown in Figure 3.1.

There are two possibilities to perform an EPR experiment: (i) the magnetic field is kept constant while the frequency of the electromagnetic field is varied or (ii)

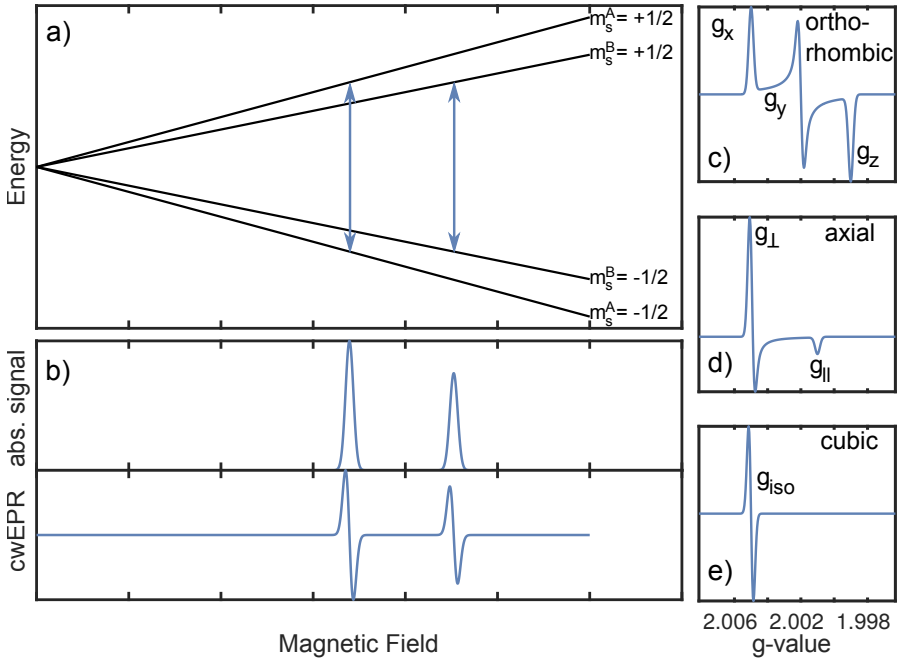


**Figure 3.1:** Zeeman splitting a) of electron A and electron B each having $S = 1/2$, b) absorption spectrum (upper plot) and lock-in detected spectrum (lower plot) as detected in cwEPR. The resulting cwEPR spectra for c) orthorhombic, d) axial and e) cubic symmetry at the paramagnetic state. Simulations performed with EasySpin [82].

the frequency is held constant and the magnetic field is scanned. In a conventional EPR setup, the second approach is employed. Whenever the magnetic field causes a splitting that matches the energy of the applied radiation, this energy is absorbed and detected as an EPR signal as shown in Figure 3.1b (top plot). As neither the frequency nor the resonance field are unique, the proportionality factor, which is the $g$-value is used to identify the paramagnetic state. The resulting cwEPR spectrum as a result of the $g$-anisotropy is illustrated in Figure 3.1c-d.

In continuous wave (cw)EPR, the magnetic field is modulated, typically at 100 kHz with amplitudes that are small compared to the values of the external field. The field modulation is employed to achieve better signal-to-noise ratios (SNR). The resulting signal is therefore approximately the derivative of the absorption spectrum (shown in the lower panel of Figure 3.1b).

### 3.1.3 The Hyperfine Interaction

The hyperfine interaction results from the interplay between the electron magnetic moment $\boldsymbol{\mu}_e$ and the nuclear magnetic moment $\boldsymbol{\mu}_I = g_n \mu_n \mathbf{I}$, where $\mathbf{I}$ is the nuclear spin, and $\mu_n$ and $g_n$ are the nuclear magneton and $g$-factor. The interaction is

magnetic field independent. The Hamiltonian is given by:

$$\mathcal{H}_{HF} = \mathbf{S} \cdot \mathbf{A} \cdot \mathbf{I} \tag{3.11}$$

where $\mathbf{A}$ is the hyperfine tensor. The total spin Hamiltonian which includes the hyperfine interaction and the electron and nuclear Zeeman term is than given as:

$$\mathcal{H} = g_e \mu_B \mathbf{B} \cdot \mathbf{S} + \mathbf{S} \cdot \mathbf{A} \cdot \mathbf{I} - g_n \mu_n \mathbf{B} \cdot \mathbf{I} \tag{3.12}$$

The hyperfine tensor $\mathbf{A}$ consist of an isotropic $a_{\text{iso}}$ and anisotropic $\mathbf{T}$ component and can be written as:

$$\mathbf{A} = a_{\text{iso}} + \mathbf{T} \tag{3.13}$$

The isotropic part of the hyperfine interaction is due to the Fermi contact interaction and is related to the electron spin density $|\psi_0(0)|^2$ at the nucleus. It can be obtained from:

$$a_{\text{iso}} = \frac{2\mu_0}{3\hbar} g_e \mu_B g_n \mu_n |\psi_0(0)|^2 \tag{3.14}$$

The anisotropic part is due to the electron-nuclear dipolar coupling. The classical expression for the interaction between an electron and a nucleus separated by a distance $r$ is given as

$$\mathcal{H}_{\text{dd}}^{HF} = \frac{\mu_0}{4\pi} \left[ \frac{\boldsymbol{\mu}_e \cdot \boldsymbol{\mu}_I}{r^3} - \frac{3\,(\boldsymbol{\mu}_e \cdot \mathbf{r})\,(\boldsymbol{\mu}_I \cdot \mathbf{r})}{r^5} \right]$$

where $\mathbf{r}$ represents the vector joining the unpaired electron and nucleus. The interaction between the magnetic moments varies with $r^{-3}$. Replacing the magnetic moments by their spin operators yields:

$$\mathcal{H}_{\text{dd}}^{HF} = -\frac{\mu_0}{4\hbar\pi} g_e \mu_B g_n \mu_n \left[ \frac{\mathbf{S} \cdot \mathbf{I}}{r^3} - \frac{3\,(\mathbf{S} \cdot \mathbf{r})\,(\mathbf{I} \cdot \mathbf{r})}{r^5} \right] \tag{3.15}$$

where $g_e$ and $g_n$ are assumed to be isotropic for simplicity. When the magnetic field is sufficiently large, $\mathbf{I}$ and $\mathbf{S}$ are quantized along $\mathbf{B}$. As stated before, by convention the $z$-axis is often chosen as the direction of $\mathbf{B}$ and hence the $x$ and $y$ components of $\mathbf{I}$ and $\mathbf{S}$ can be neglected. For the special case of an unpaired electron in a pure $p$-orbital, with its axis in the $xy$-plane centered on the interacting nucleus, the angle $\theta$ describes the angle between the $z$-direction and the axis of the $p$-orbital ($xy$-plane). With $\mathbf{S} \cdot \mathbf{I} = Sz \cdot I_z$ this results in

$$\begin{aligned} \mathbf{S} \cdot \mathbf{r} &= S_z \cos\theta \\ \mathbf{I} \cdot \mathbf{r} &= I_z \cos\theta \end{aligned} \tag{3.16}$$

By substitution in equation 3.15 this results in

$$H_{\text{dd},z}^{HF} = \frac{\mu_0}{4\pi} g_e g_n \mu_B \mu_n \frac{m_s m_I}{r^3} (3\cos^2\theta - 1) \tag{3.17}$$

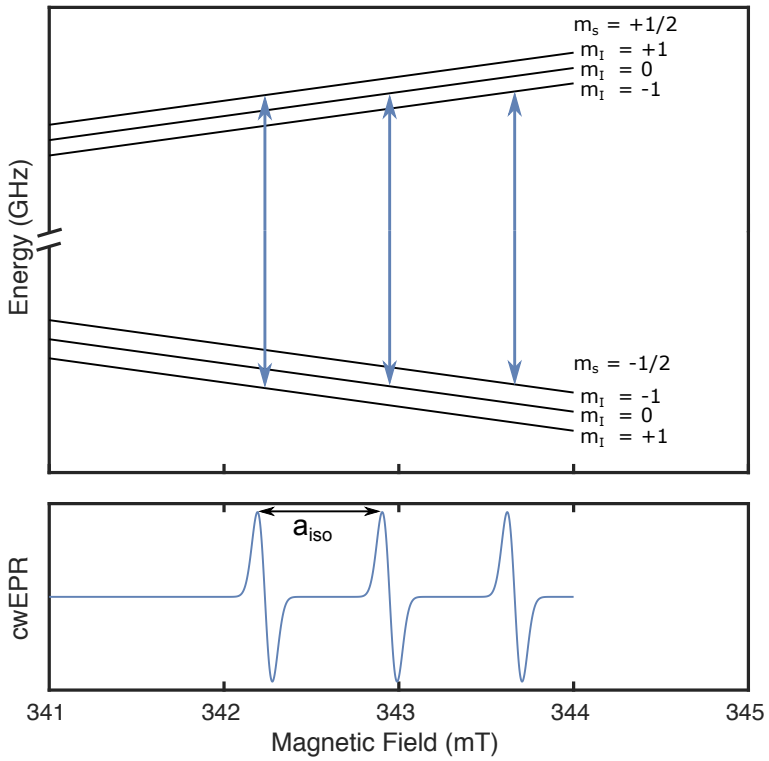


**Figure 3.2:** Zeeman splitting of an electron with $S = 1/2$ inside a magnetic field with a hyperfine splitting for one nucleus with $I = 1$. The lower panel indicates the spectrum upon field modulation (lock-in detection). Simulation with EasySpin toolbox [82] in Matlab, with a $^{14}$N nucleus, $a_{\mathrm{iso}} = 20\,\mathrm{MHz}$, $\Delta B = 0.1\,\mathrm{mT}$, and $g = 2$.

where $m_I$ is the magnetic quantum number in analogy to $m_s$. The orientation dependence is therefore $(3\cos^2\theta - 1)$. The resulting energy is maximal if $\theta = 0°$ or 180°, which is parallel or antiparallel to the direction of the applied magnetic field. This yields $T_z = 3\cos^2\theta - 1 = 2$. The minimal energy is obtained for $\theta = 90°$ and gives the matrix elements $T_x = T_y = 3\cos^2\theta - 1 = -1$. In its diagonalized form the matrix $\mathbf{T}$ is written as

$$\mathbf{T} = \frac{\mu_0}{4\hbar\pi}\frac{g_e\mu_B g_n\mu_n}{r^3}\begin{pmatrix} -1 & 0 & 0 \\ 0 & -1 & 0 \\ 0 & 0 & 2 \end{pmatrix} \tag{3.18}$$

The above consideration essentially means that the orbital shape plays a role in the anisotropy of the hyperfine matrix $\mathbf{T}$. The anisotropy vanishes when the electron is in a spherical orbital of $s$ character. It is useful to note that the isotropic hyperfine coupling is $a_{\mathrm{iso}} = tr(\mathbf{A})/3$.

An unpaired electron of $S = 1/2$ experiencing a hyperfine interaction with a nucleus of $S = 1$ inside a magnetic field, results in the splitting of $(2S+1)(2I+1)$ states as shown in Figure 3.2. Following the selection rule $\Delta m_I = \pm 1$, each nucleus splits each EPR line into equidistant $(2I + 1)$ lines of the same intensity. Thus, the number

Table 3.1: Triplet and singlet substates, where the former has symmetric wave functions and the latter antisymmetric spin wavefunction with respect to the exchange of the particles.

| Symmetric | Antisymmetric |
|---|---|
| $\|T_+\rangle = \|\uparrow\uparrow\rangle$ | |
| $\|T_0\rangle = \frac{1}{\sqrt{2}}(\|\uparrow\downarrow\rangle + \|\uparrow\downarrow\rangle)$ | $\|S\rangle = \frac{1}{\sqrt{2}}(\|\uparrow\downarrow\rangle - \|\uparrow\downarrow\rangle)$ |
| $\|T_-\rangle = \|\downarrow\downarrow\rangle$ | |
| Triplet: $S = 1$ | Singlet: $S = 0$ |

of hyperfine transition grows by multiplication with the number of nonequivalent magnetic nuclei, giving rise to $(2I + 1)^n$ transitions. In the case of $n$ equivalent nuclei, some EPR lines overlap reducing the transitions to $2nI + 1$. The intensities of the hyperfine lines follow a distribution scheme according to Pascal's triangle.

### 3.1.4 Spin-Spin Interaction

In systems containing two or more unpaired electrons, the spins can interact through dipolar and/or exchange interaction. For the simplest system consisting of two interacting electron spins, the complete Hamiltonian can be expressed as the sum of $\mathcal{H}_0$ of the individual spins in addition to the exchange $\mathcal{H}_{ex}$ and the dipolar $\mathcal{H}_{dd}$ interaction Hamiltonian

$$\mathcal{H}_0(S_1, S_2) = \mathcal{H}_0(S_1) + \mathcal{H}_0(S_2) + \mathcal{H}_{\mathrm{dd}} + \mathcal{H}_{\mathrm{ex}} \tag{3.19}$$

Four different states results from the possible combinations of the magnetic quantum numbers $m_{S1}$ and $m_{S2}$, giving the uncoupled basis

$$|\uparrow\uparrow\rangle, |\uparrow\downarrow\rangle, |\downarrow\uparrow\rangle, |\downarrow\downarrow\rangle \tag{3.20}$$

which correspond to the eigenbasis of the Hamiltonian in the absence of exchange or dipolar interactions. In the presence of dipolar or exchange coupling, it is more convenient to work with the coupled basis, which in the limit of strong coupling yields one singlet, $S = 0$, state with antiparallel orientation of the two spins, and three triplet states, with $S = 1$ and $m_S = +1, 0, -1$ (multiplicity of three). The triplet wavefunctions are symmetric with respect to exchange of the particles, while the singlet spin wavefunction is antisymmetric (see Table 3.1).

As the Pauli principle must be obeyed and therefore the overall wavefunction must be antisymmetric, the orbital wavefunction is antisymmetric for the triplet state and symmetric for the singlet state. In the case of strong coupling, it is generally more convenient to consider a group spin $S = 1$ in the spin Hamiltonian for the description of EPR experiments.

#### The Exchange Coupling

The Hamiltonian for isotropic exchange is given by:

$$\mathcal{H}_{\text{ex}} = J\mathbf{S}_1 \cdot \mathbf{S}_2 \tag{3.21}$$

where $J$ is the exchange coupling constant and can be described by the Coulomb exchange integral. It leads to an energetic difference between singlet and triplet states. The sign of $J$ determines whether the singlet or triplet state lies lower in energy. The exchange coupling constant $J$ depends on the overlap of electron wavefunctions and reflects the spatial separation of the spins. Small values for $|J|$ indicate that the unpaired electrons are far apart (less Coulomb exchange), whereas large values denote a small separation and hence a large Coulomb exchange.

#### The Dipolar Interaction

The dipolar interaction Hamiltonian for two electron spins can be derived by analogy to the classical expression for interacting dipole moments

$$\mathcal{H}_{\text{dd}}^{SS} = \frac{\mu_0}{4\pi}\left[\frac{\boldsymbol{\mu}_1 \cdot \boldsymbol{\mu}_2}{r^3} - \frac{3\,(\boldsymbol{\mu}_1 \cdot \mathbf{r})\,(\boldsymbol{\mu}_2 \cdot \mathbf{r})}{r^5}\right] \tag{3.22}$$

with $\mu_0$ as the vacuum permeability and $\mathbf{r}$ the vector connecting the two spins. Replacing the magnetic-moment operators $\boldsymbol{\mu}_{1,2}$ by the corresponding spin operators yields,

$$\mathcal{H}_{\text{dd}}^{SS} = \frac{\mu_0}{4\pi} g_1 g_2 \mu_B^2 \left[\frac{\mathbf{S}_1 \cdot \mathbf{S}_2}{r^3} - \frac{3\,(\mathbf{S}_1 \cdot \mathbf{r})\,(\mathbf{S}_2 \cdot \mathbf{r})}{r^5}\right] \tag{3.23}$$

with $g_1$ and $g_2$ being the $g$-values of electrons 1 and 2. The interaction between the spin-pair is inversely proportional to $r^3$ and thus allows the inter-spin distance to be determined from the coupling strength.

### 3.1.5 Strongly Coupled Pair: Triplet State

The limit of a strongly coupled spin pair is explained with the example of the triplet state. The total Hamiltonian for a triplet state may be written as

$$\mathcal{H} = g\mu_B \mathbf{B}\mathbf{S} + \mathbf{S}\overline{\mathbf{D}}\mathbf{S} \tag{3.24}$$

with the second part of the equation representing $\mathcal{H}_{dd}^{SS}$. The $\overline{\mathbf{D}}$ tensor is referred to as the Zero-field splitting (ZFS) tensor, as the interaction lifts the degeneracy of the three triplet sublevels even in the absence of an external magnetic field, and in addition to the spin-spin contribution described above can also contain spin-orbit contributions in the presence of heavy elements.

Since $\overline{\mathbf{D}}$ is traceless, in the eigenbasis of the ZFS Hamiltonian it can be expressed in terms of two independent parameters $D = -\frac{3}{2}D_z$ and $E = \frac{1}{2}(D_x - D_y)$, known

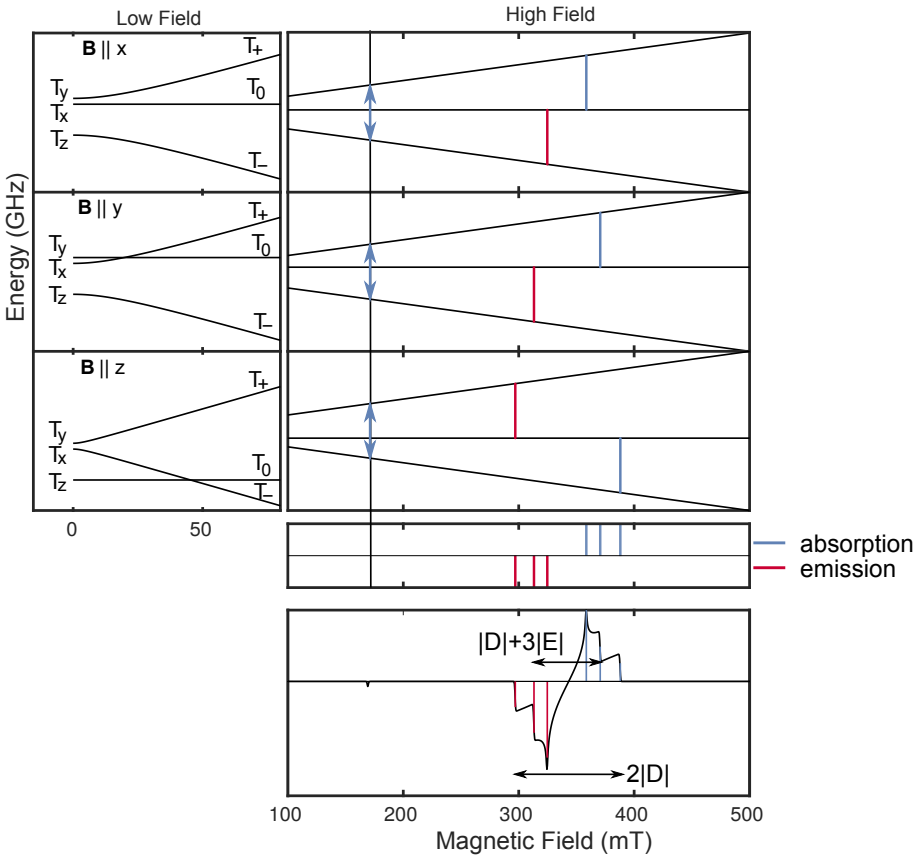


**Figure 3.3:** Energies of triplet sublevels of a triplet state with $D = 1275\,\text{MHz}$ and $E = 100\,\text{MHz}$ as a function of an external magnetic field with the field vector $\mathbf{B}$ aligned with the dipolar axes of $x$, $y$, and $z$, respectively in the zero-field and high-field limit. If the microwave radiation matches the energy gap between either $|T_+\rangle$ or $|T_-\rangle$ and $|T_0\rangle$, a transition can be observed. The transitions can either be absorptive (blue) or emissive (red) depending on the population of the high field sublevels. The powder spectrum in the bottom plot indicates the transitions corresponding to the canonical orientations (marked by horizontal lines) which are characterized by the turning points (with the population of the zero-field states as $[|T_z\rangle\ |T_x\rangle\ |T_y\rangle] = [0.10\ 0.45\ 0.45]$). This figure was generated with the EasySpin toolbox [82] for Matlab.

as the ZFS parameters

$$\boldsymbol{D} = \begin{pmatrix} -\frac{1}{3}D + E & 0 & 0 \\ 0 & -\frac{1}{3}D - E & 0 \\ 0 & 0 & \frac{2}{3}D \end{pmatrix} \tag{3.25}$$

The exchange term is neglected in equation 3.24, as it only contributes with a constant energy for each of the three triplet states. In the absence of an external magnetic field the eigenbasis of the Hamiltonian corresponds to the zero-field states

$|T_x\rangle$, $|T_y\rangle$, and $|T_z\rangle$ with energies

$$\begin{aligned} E_x &= -D_x = \frac{1}{3}D - E \\ E_y &= -D_y = \frac{1}{3}D + E \\ E_z &= -D_z = -\frac{2}{3}D \end{aligned} \tag{3.26}$$

If the electron Zeeman interaction exceeds the ZFS interaction, the high-field states $|T_+\rangle$, $|T_0\rangle$, $|T_-\rangle$ (see table 3.1) are the eigenstates. The zero-field states can be expressed as linear combinations of the high-field states: for $\mathbf{B}$ parallel to the $z$ principal axis of the ZFS tensor

$$\begin{aligned} |T_x\rangle &= \frac{1}{\sqrt{2}}\left(|-1\rangle - |+1\rangle\right) \\ |T_y\rangle &= \frac{i}{\sqrt{2}}\left(|-1\rangle + |+1\rangle\right) \\ |T_z\rangle &= |0\rangle \end{aligned} \tag{3.27}$$

Thus for $B \parallel z$, the $|T_0\rangle$ state is equal to the corresponding zero-field state $|T_z\rangle$ and independent of the magnetic field. Similar expressions can be derived for for an external magnetic field parallel to $x$- and $y$-axes of the zero-field splitting tensor. The energy level splitting for $\mathbf{B} \parallel x, y, z$, also referred to as the canonical orientations, as a function of magnetic field is shown in Figure 3.3. For each orientation of $\mathbf{B}$ with respect to the ZFS tensor, two allowed transitions lead to two peaks in the spectrum. The sum over all possible orientations of the molecule with respect to the field leads to a powder spectrum as shown in the bottom plot of Figure 3.3. Spectral positions where $\mathbf{B}$ is parallel to one of the principal ZFS tensor axes are characterized by turning points in the spectrum and the $D$ and $E$ parameters can be determined from the distance between them as shown in the bottom plot in Figure 3.3.

### 3.1.6 Weakly Coupled Pair: CT-State

For a weakly coupled spin pair the exchange interaction $J$ becomes relevant and therefore the energy difference between the singlet and triplet states, becomes smaller. To describe this type of spin-pair, the coupled basis given in equation 3.20 can be used. In the presence of exchange and dipolar coupling, the Hamiltonian is non-diagonal in the given basis. However, it can be diagonalized by unitary transformation leading to the four eigenstates:

$$\begin{aligned} |1\rangle &= |\uparrow\uparrow\rangle \\ |2\rangle &= |\uparrow\downarrow\rangle\cos\alpha + |\downarrow\uparrow\rangle\sin\alpha \\ |3\rangle &= |\downarrow\uparrow\rangle\cos\alpha + |\uparrow\downarrow\rangle\sin\alpha \\ |4\rangle &= |\downarrow\downarrow\rangle \end{aligned} \tag{3.28}$$

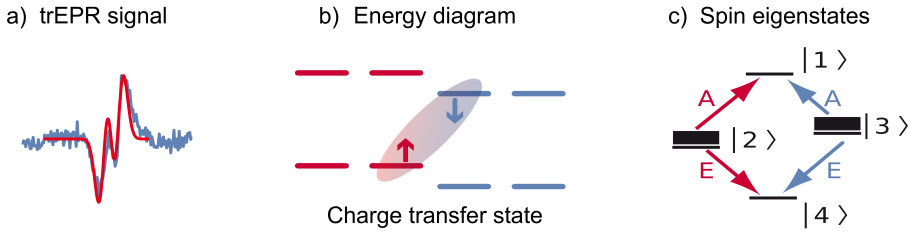


**Figure 3.4:** a) The CT-state signature as measured in transient EPR, b) the energy level diagram illustrating the occupation of the spins, and c) schematics of the eigenstates $|1\rangle$, $|2\rangle$, $|3\rangle$, and $|4\rangle$. Adapted from [83].

where $\alpha$ measures the coupling strenght between the two interacting spins and is defined as:

$$\alpha = \frac{1}{2}\arctan\left(\frac{J-D}{\hbar\Delta\omega}\right) \tag{3.29}$$

with $\Delta\omega = \omega_1 - \omega_2$ representing the difference in eigenfrequencies (Larmor frequencies) of $S_1$ and $S_2$. This gives rise to two pure triplet states ($|1\rangle$ and $|4\rangle$) and two new states with partial singlet and partial singlet character ($|2\rangle$ and $|3\rangle$). As a result of the exchange and dipolar interaction, these four states are energetically non-equidistant and four allowed transitions can be excited in EPR. The four levels are illustrated in Figure 3.4c.

In the case of $\alpha = 0$, the spin species are not coupled. If the spins are strongly coupled for $\alpha = \frac{\pi}{4}$ the states in 3.28 transform into the triplet and singlet substates given in Table 3.1.

$$\begin{aligned}
|1\rangle &\rightarrow |T_+\rangle = |\uparrow\uparrow\rangle \\
|2\rangle &\rightarrow |S\rangle = \frac{1}{\sqrt{2}}(|\uparrow\downarrow\rangle - |\uparrow\downarrow\rangle) \\
|3\rangle &\rightarrow |T_0\rangle = \frac{1}{\sqrt{2}}(|\uparrow\downarrow\rangle + |\uparrow\downarrow\rangle) \\
|4\rangle &\rightarrow |T_-\rangle = |\downarrow\downarrow\rangle
\end{aligned} \tag{3.30}$$

An example of weakly coupled spin pairs is an electron-hole pair at the CT-state (see section 2.2.2). The CT-state is a transitional state between coupled excitons and non-coupled polarons (Figure 3.4b) and is often observed with (low temperature) EPR in organic donor-acceptor blends after a few 100 ns after optical excitation [84]. Due to the four possible transitions, the spectrum will consist of a non-Boltzmann polarization pattern. The signals will partially overlap, due to the large exchange and small spatial separation between the spins. The spectrum is shown in Figure 3.4a.

### 3.1.7 $\Delta g$-Mechanism

If the difference in $g$-values of the photogenerated holes and electrons is large enough, population changes (or spin mixing) in the sublevels based on the $\Delta g$-mechanism can occur. This type of spin-mixing mechanism is significant for systems of large SOC and becomes more efficient at higher magnetic fields [85]. Assuming the electron spins $S_A$ and $S_B$ to be weakly coupled to each other but strongly coupled to the magnetic field, there exist two singlet-triplet interconversion mechanisms [86]: (i) interconversion of $T_0$ and $S$ and (ii) interconversion of $T_+$ ($T_-$) and $S$ by spin-flip mechanism.

#### Interconversion of $T_+$ ($T_-$) and $S$

This type of interconversion involves the flip of an electron spin. The force for flipping originates from magnetic fields perpendicular, e.g. provided by the nuclei, to the magnetization direction (precession direction). This is shown in Figure 3.5a. The spin flip will cause the electrons to go from a $T_+$ or $T_-$ triplet state to a singlet state $S$ and vice versa.

#### Interconversion of $T_0$ and $S$

This interconversion is based on the rephasing of spins as displayed in Figure 3.5b. The starting point of the spin pair at $t = 0$ is a triplet state $T_0$ (total spin $S = 1$ and $m_S = 0$). Internal magnetic fields originating from nearby nuclear spins and electron orbital motion will cause spin $S_A$ to precess with a different frequency than $S_B$. If both are 90° out of phase, they will be in a coupled singlet-triplet state. After a period of time $t = \pi/\Delta\omega$, they will evolve into a singlet state. The difference in precession frequencies is given by

$$\Delta\omega = \frac{\mu_B}{\hbar} B \Delta g + \Delta \sum_i a_i m_i \tag{3.31}$$

where the first term gives the difference in Zeeman interaction for cases in which the $g$-values of the paramagnetic species are different ($g_A \neq g_B$) and the second term arises from the difference in hyperfine fields experienced by the paramagnetic species, with $a$ as the hyperfine interaction and $m$ as the magnetic quantum number. The rate for the interconversion for rephasing of $T_0$ and $S$ thus depends on the difference of the $g$-value of $S_A$ and $S_B$ and the hyperfine fields experienced by the spins. If $\Delta g$ is small, then the rate for $T_0 \leftrightarrow S$ transition given by $1/\Delta\omega$ will also become small and spin decoherence occurs. However, if $\Delta g$ becomes larger, then the transition rate increases and if it becomes longer than the spin-lattice relaxation, the population of the spin sublevels can be modulated by an external magnetic field.

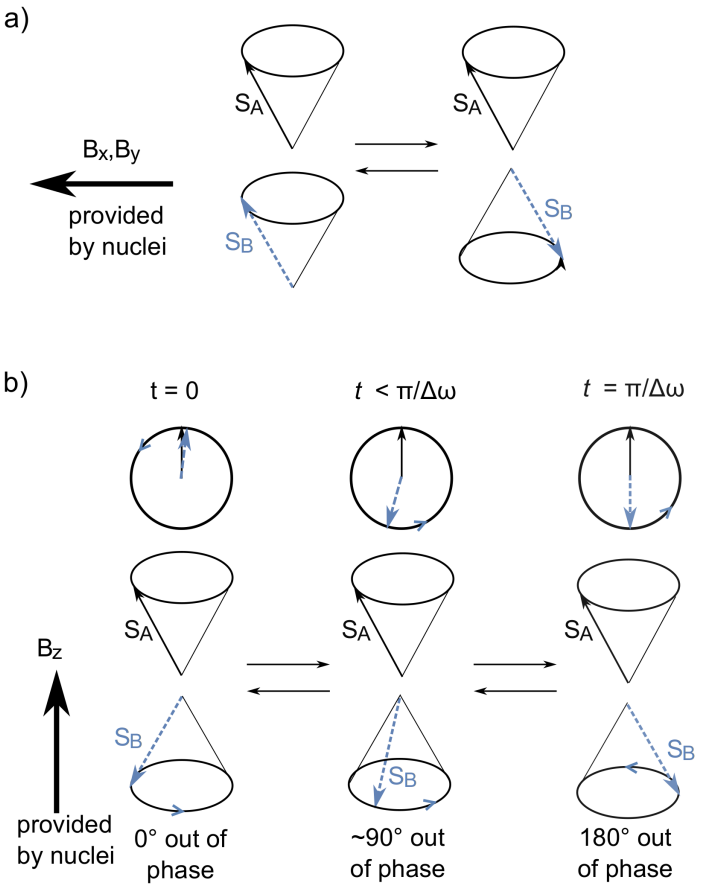


**Figure 3.5:** singlet-triplet interconversion mechanisms: a) interconversion by spin-flip. A magnetic field provided by nuclei causes the $S_B$ to be oriented in a singlet configuration with respect to $S_A$, b) interconversion of $T_0$ and $S$ caused by the rephasing mechanism. A magnetic field $B_z$ causes $S_B$ to precess at a different frequency than $S_A$. At $t = 0$ $S_A$ and $S_B$ are in phase and in a triplet configuration, at the $t < \pi/\Delta\omega$ they evolve into a singlet-triplet coupled state, and after $t = \pi/\Delta\omega$ they are in a pure singlet configuration. Adapted form [86].

## 3.2 Spin Dependent Processes

The idea of magnetic resonance is to obtain information on the microscopic environment of paramagnetic centers. In organic semiconductors such paramagnetic states can be defects, impurities, polarons etc., which if in resonance with a magnetic field can result into microwave absorption in EPR experiments. EDMR experiments rely on a different detection mode, namely the change in sample conductivity, which is evoked by changes of the spin pair singlet-to-triplet proportion, leading to increased recombination and/or hopping in the sample.

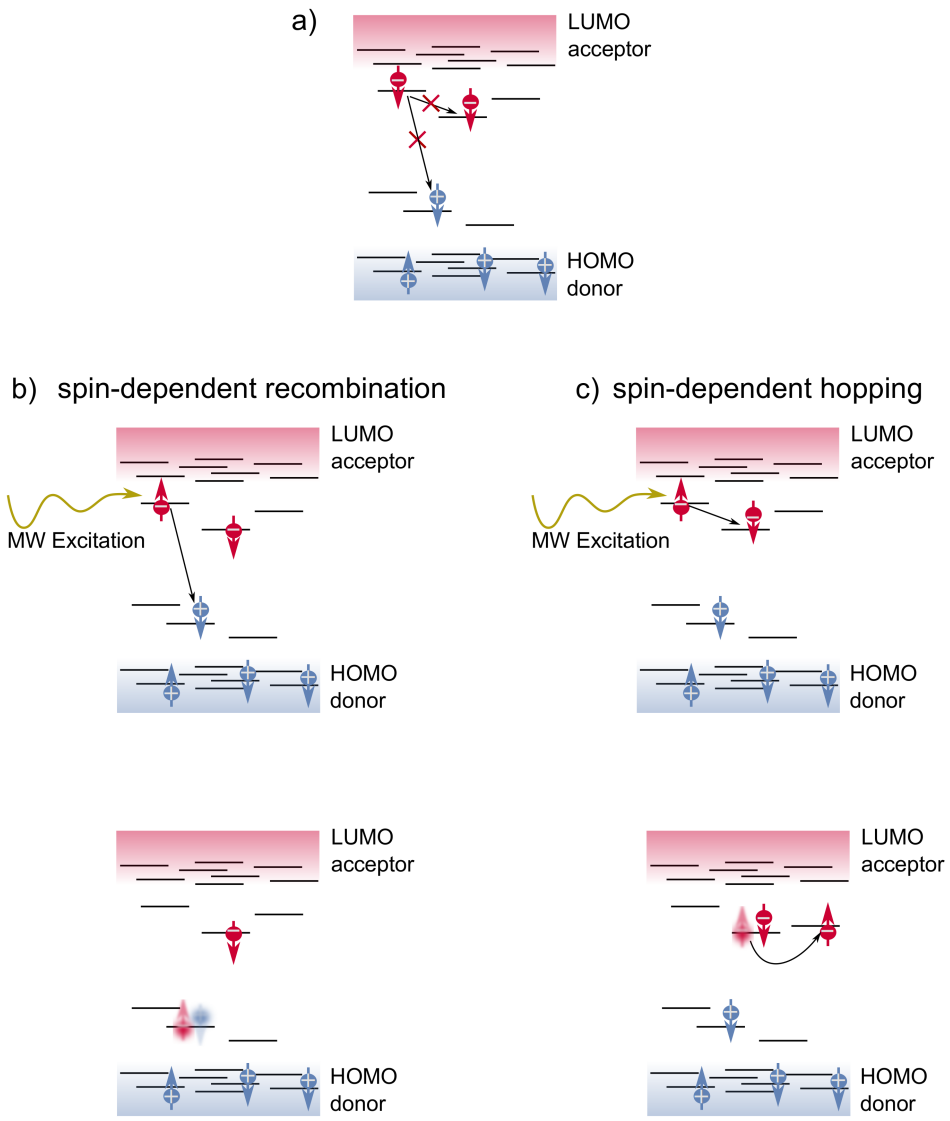


**Figure 3.6:** Spin manipulation by a microwave pulse in EDMR a) initial situation showing forbidden transitions. By MW excitation the spin orientation is changed allowing the transitions to occur and lead to b) spin-dependent recombination, where an electron hops to a state near the donor HOMO and recombines with a hole or c) spin-dependent hopping to a singly occupied nearby state. If sufficient energy is available, the electron can hop multiple times.

Figure 3.6 demonstrates the effect of spin-dependent hopping and recombination in a device consisting of organic semiconductors with localized states between the HOMO and LUMO levels sites. The transport pathways for the charge at such a localized state are blocked due to its spin orientation. This scenario is illustrated in Figure 3.6a. By microwave excitation the orientation of one of the spins can be changed and the initially forbidden transitions become allowed (Figure 3.6b and c upper panel). From this stage the charge carrier has two fates. In the case of hopping

into a state close to the HOMO of the donor, it may attract a hole of opposite spin configuration and recombine through spin-dependent recombination. This is shown in Figure 3.6b in the lower panel. The charge carriers are annihilated (blurred out in the figure) and the net charge carrier concentration in the sample is reduced. Alternatively, the charge hops to a nearby singly occupied state (if the hop is energetically favorable), as the spin configuration allows it: spin-dependent hopping. If further energy is available, either thermally or supplied by further microwave excitation, the charge can hop further until it reaches the electrode. This results in an increase in charge carrier mobility, as long as the transport through semiconductor is guaranteed. The charge carrier concentration does not change during spin-dependent hopping.

### 3.2.1 Charge Transport in Organic Semiconductors

For a perfectly ordered system, hopping transport results only from dynamic disorder. Here, hopping is controlled by only a thermally activated transport rate (and hence is time independent), that determines the mobility and diffusibility of charges. Due to the large disorder in most organic materials, the variations in the site energy and in the distance between the sites are large. The hopping rates are therefore asymmetric and charge transport occurs as a random walk by incoherent jumps between neighboring sites. The random distribution of levels or sites predominately results from the van der Waals coupling with neighboring states and can be described by a Gaussian distribution

$$g(E) = \sqrt{\frac{1}{2\pi\sigma}} \exp\left(-\frac{(E-E_0)^2)}{2\sigma^2}\right) \tag{3.32}$$

where $E$ is the energy of an individual molecule and $\sigma$ is the standard deviation from this energy, which can be interpreted as the disorder parameter and characterizes the width of the distribution (Figure 3.7).

With the density of states (DOS) taking on a Gaussian function, charge transport in disordered systems can be modeled as follows: for a charge to hop from a localized state to a delocalized one, thermal activation is required. Therefore initially charge carriers jump downhill in energy. As the charge reaches the center of the DOS, excitation will promote further transport away from the original state. The energy that allows for this transport is called the transport energy and is found in the middle of the DOS. This means that transport mainly takes place around the transport energy by uphill and downhill jumps. Localized states in the tail of the DOS below the transport energy function rather as traps as these do not participate in the transport process.

In the above discussion, the spin of the charge carrier was neglected. However, in considering that charge carrier hopping is strongly dependent on the Pauli exclu-

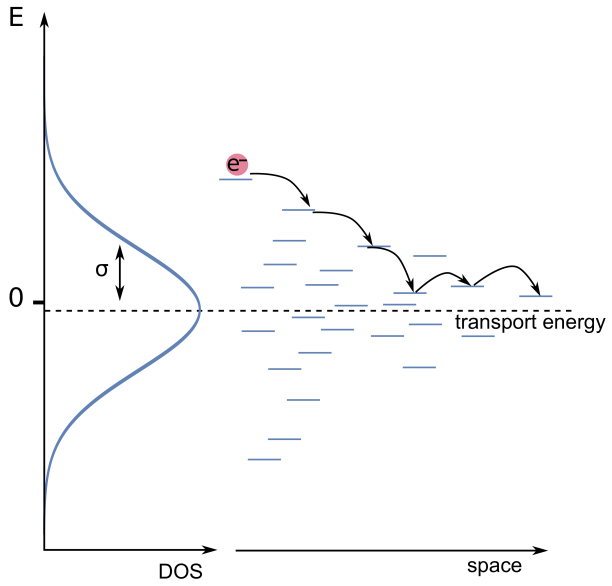


**Figure 3.7:** Illustration of the DOS distribution described by a Gaussian distribution and an electron at an arbitrary energy, that hops within the DOS. The dashed-horizontal line indicates the transport energy. Adapted from [14].

sion principle, the spin plays a key role in transport and will be explained in the framework of the spin-pair model.

### 3.2.2 The Spin Pair Model

To describe resonant changes in the conductivity of a device, Kaplan Solomon, and Mott developed the spin-pair model, which is solely based on the symmetry of the spin wavefunction [87].

As a charge carrier travels through a semiconductor, its spin will experience interactions with other paramagnetic centers, i.e. an other electron, hole, or defect. The fate of the charge carrier will depend on the relative orientation on the two interacting spins and the subsequent processes will follow from it.

In the following discussion two spins are considered. It is assumed that upon an encounter of the two spins, a polaron pair is formed [87, 88]. The Hamiltonian describing the interaction of a spin pair inside a magnetic field was discussed before in section 3.1.4. The pair is usually described in the weakly coupled limit (section 3.1.6) with the eigenstates given by 3.28.

Resonant microwave absorption can drive transitions between the states, causing changes in their population. The pure singlet and triplet states can be assigned the

transition probabilities $r_S$ and $r_T$ respectively. For the coupled states $|2\rangle$ and $|3\rangle$ the transition probability depends on the initial spin state $|i\rangle$

$$r_i = r_s|\langle i|S\rangle|^2 + r_T|\langle i|T_0\rangle|^2 \tag{3.33}$$

### 3.2.3 Spin-Dependent Recombination

The basic concept of recombination is the annihilation of an electron-hole pair. This can proceed in a radiative or non-radiative way. Two types of recombination processes exist that depend on the precursor state. If the annihilated electron-hole pair stems from the same excited state, the type of recombination is referred to as geminate. This can be an excited state on the molecule or a state after photogeneration of electron-hole pairs in photoactive materials. In the case of non-geminate recombination, the precursor state is different for the involved electron and hole. It occurs while charge carriers travel through the semiconductor, encounter and recombine.

In disordered systems, trap-assisted recombination can also prevail. This type of recombination is known as Shockley-Read-Hall (SHR) recombination [14]. This occurs if charge carriers hop into band-gap states (or states in the HOMO-LUMO gap) that function as traps and consists of two steps. In the first step, an electron in the LUMO hops to a neighboring deeper lying state close to HOMO. In the second step, a hole from the HOMO is attracted by the electron and recombine.

Geminate recombination will occur directly after charge carrier generation. As charge carriers are created in a singlet state, this recombination process is not directly spin-dependent, and therefore does not influence the photocurrent [89, 90]. Non-geminate and SRH recombination processes are spin-dependent in organic semiconductors as they involve localized states. Consider that such a state is singly occupied. According to the Pauli principle only charge carriers of anti-parallel spin can occupy the same state. Therefore, only singlets can make the transition, while spin-triplets cannot. Therefore, equation 3.33 can be approximated when neglecting triplet state recombination which results in

$$r_{2,3} \approx \frac{1}{2}(r_S + r_T) \tag{3.34}$$

With resonant excitation of one of the spins of the $|\uparrow\uparrow\rangle$ or $|\downarrow\downarrow\rangle$ states, the spin symmetry is changed by creation of a coupled state $|2\rangle$ or $|3\rangle$: the singlet content in the sample increases and the transition given by equation 3.33 becomes more probable, thus recombination becomes possible. If the recombination involves an electron and a hole, the pair will be annihilated, reducing the charge carrier concentration. For a spin ensemble this will have direct consequences on the sample conductivity: as the charge carrier concentration is reduced, the conductivity will decrease as well.

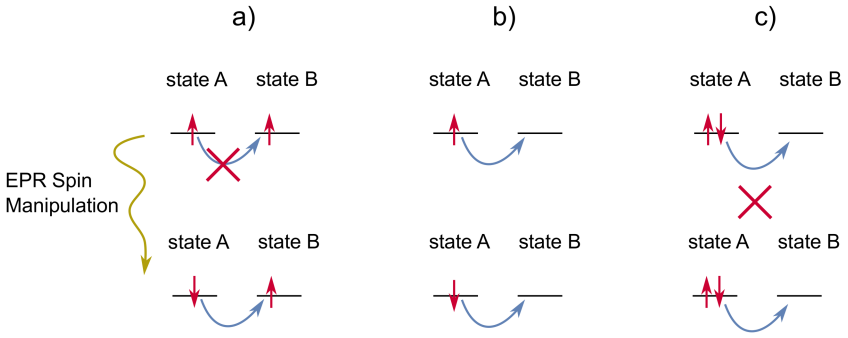


**Figure 3.8:** Hopping possibilities of a charge between states A and B illustrating the spin relevance. a) Hopping between two singly occupied states: spin dependent. Spin manipulation makes the transition possible. Hopping from a singly b) and doubly c) occupied state to an empty state: spin independent. Option c) cannot be accessed with EPR.

### 3.2.4 Spin-Dependent Hopping

The hopping of electrons is in actuality a tunnelling process that becomes spin-dependent once it involves two singly occupied states. This is because due to the Pauli exclusion, the hopping process depends on the spin orientation of the involved electrons. Being at spin resonance with one of the electrons, enables the manipulation of its spin and may increase the probability of tunnelling into the singly occupied state. In effect the electron mobility is increased while the charge carrier concentration remains unchanged.

In the following we limit the description to the hopping transport of electrons from one localized state to another, since the equivalent description will apply for the transport of holes. The model for spin-dependent hopping adapted from [89] is shown in Figure 3.8.

This model firstly requires that two singly occupied states are in close spatial and energetic proximity. Secondly, the spin is conserved during the transition, as the spin selection rules dominate the transition probability. Considering two states A and B, the transition becomes spin-dependent if both states are singly occupied (Figure 3.8a). If only A is singly occupied, while B is empty, the transition is spin independent. The same goes for a transition from a doubly occupied state A to an empty state B as seen in Figure 3.8b and c respectively. This initial singlet state cannot be manipulated by EPR and hence the hopping transition is spin-independent.

Therefore in the case of Figure 3.8a, the tunnelling probability depends on the symmetry of the electron spin wavefunctions. The transition rates can be written as in equation 3.33 with $r_{1,4} = r_T$. The spin-spin interaction can be neglected for a weakly coupled pair, which results in the eigenstates $|2\rangle \approx |\uparrow\downarrow\rangle$ and $|3\rangle \approx |\uparrow\downarrow\rangle$ being

identical and the approximation of 3.34 for the transition rate $r_{2,3}$ is in analogy to spin-dependent recombination.

Chapter 4

# Samples and Methods

*This chapter describes the experimental methods used within the framework of this thesis. The first part outlines the preparation of various types of samples, which for the most part was carried out at the labs of the Freie Universität Berlin. Perovskite samples were prepared at different labs in collaboration with Lukas Kegelmann and Steve Albrecht (HZB) and Christian Wolff (AG Neher, University of Potsdam). In the second part, an overview of the EPR techniques used to study the samples and a description of the experimental setup is given. Finally, a list of the EPR spectrometers and other instrumentation is provided at the end of the chapter.*

## 4.1 Sample Preparation

The samples studied in this work for the most part are composed of organic materials that are prone to degradation once exposed to oxygen. Therefore, most of the sample preparation took place in a nitrogen ($N_2$) filled glovebox. After preparation, care is taken to properly seal the samples to avoid aging in ambient atmosphere.

### 4.1.1 Spiro-OMeTAD Doping Series

All chemicals were used as received and all samples were prepared inside a nitrogen-filled glove box. Spiro-OMeTAD (Merck KGaA) was dissolved in chlorobenzene (Sigma Aldrich) under exclusion of UV light. For the doping series with FK209, a spiro-OMeTAD concentration of 36.2 mg/ml was used. For the Li-TFSI doping series, a concentration of 72.3 mg/ml of spiro-OMeTAD was used. FK209 (Dyenamo AB) and Li-TFSI (Sigma Aldrich) were dissolved in acetonitrile (Sigma Aldrich) at concentrations of 300 mg/ml and 520 mg/ml, respectively. The doping ratio was varied by diluting the dopants and keeping the concentration of spiro-OMeTAD fixed. 60 $\mu$l or 30 $\mu$l of the doped solutions were transferred into EPR quartz tubes of 3.9 mm or 2.9 mm outer diameter for X- and Q-band measurements, respectively. The solvent was evaporated under vacuum, leaving a film on the inner-wall of the quartz tube. The tubes were then filled with helium and sealed using a blowtorch. The samples for the aging measurements were not sealed. In the case of solution

samples, a freeze-pump-thaw method was used for degassing. This was as well followed by filling with helium and sealing by blowtorch.

### 4.1.2 Samples for Conductivity Measurements

For the conductivity measurements, pristine and Li-doped spiro-OMeTAD layers were deposited on cleaned glass substrates. To provide sufficient wetting, a 50 nm layer of aluminum oxide ($Al_2O_3$) was first coated on the glass from an $Al_2O_3$ nanoparticles dispersion (20 wt.% in isopropanol, Sigma Aldrich, 1:10 vol.% dilution of isopropanol) and spin coated at 1000 rpm for 30 s with subsequent annealing for 1 h at 180°C. Two substrates each were spin coated at 2000 rpm for 30 s inside a nitrogen filled glovebox using 36.2 mg/ml solutions of pristine or Li-TFSI-doped (doping ratio 1:10) spiro-OMeTAD in chlorobenzene on top of the $Al_2O_3$ film. A layer thickness of 250 nm was determined from scanning electron microscopy cross-section images recorded with Hitachi S-4100 scanning electron microscope at 5 kV acceleration voltage and 30k magnification.

Lateral conductivities were determined on a glass/$Al_2O_3$/spiro-OMeTAD layer stack by a laboratory-built mercury probe setup following Abowitz et al. [91] in combination with a Keithley model 237 voltage source measurement unit. The obtained conductivities can be found in Table B.1.

### 4.1.3 Organic Bulk Heterojunction Solar Cells

Quartz glass substrates of the dimension (57.5 × 2.5 × 0.5) mm patterned with 100 nm layer of Indium Tin Oxide (ITO) were cleaned in subsequent steps of different solvents: acetone, 2% Hellmannex solution, distilled water, and iso-propanol and with 15 min. inside an ultra-sonic bath between each step. The substrates were dried by an air stream.

Poly(3,4-ethylenedioxythiophene) polystyrene sulfonate (PEDOT:PSS) filtered suspension is deposited on the substrates by spin coating it at a speed of 1800 rpm for 40 s. The substrates are then annealed at 100° C on a hotplate for 15 min.

Poly(4,4-dioctyldithieno(3,2-b:2',3'-d)silole)-2,6-diyl-alt-(2,1,3-benzo-thiadiazole)-4,7-diyl (PSBTBT-8) (1-Material Organic Nano Electronic) and PCBM (Solene) were mixed at a weight ratio of 1 : 1.5, respectively, and dissolved in 1,2 dichlorobenzene. Two concentrations were prepared: 16.1 mg/ml and 12 mg/ml. These were firstly deposited on pre-cut microscope glass substrates to test the thickness of the film with the prepared concentration.

From profilometer measurements on the microscope glass substrates[1] a maximum film thickness of 50 nm for the 16 mg/ml concentration spincoated at a speed of 800 rpm for the first 20 s and 1400 rpm for the following 40 s was determined. The mentioned concentration and spincoating settings were used on the ITO-patterned substrates. The substrates were then left in the antichamber to dry for $\sim 1$ hour.

After drying, the samples were transferred to the evaporation chamber, where under a vacuum pressure of $10^{-7}$ mbar firstly a 20 nm layer of calcium followed by a 200 nm layer of aluminum were evaporated. The calcium layer acts as a hole-blocking layer in the device, but also matches the workfunction between the organic blend and the Al electrode.

Two thin copper stripes were soldered on to two separate cables. The stripes were carefully placed on the ITO-lanes that are separated by lithography to prevent shortcuts. After this procedure the cells were put inside an EPR tube of 4 mm outer diameter. A two component epoxy resin (Emrson and Cuming STYCAST 1266), mixed at the ratio $A$:$B$ of 28:100 was used for sealing.

### 4.1.4 Sn-Pb Based Perovskite Solar Cells

The perovskite solar cells were prepared at the labs of the Dieter Neher group in University of Potsdam with the help of Christian Wolff.

The ITO-patterned quartz substrates were cleaned as described above. After a short plasma treatment a filtered (using a 2 $\mu$m PTFE filter) PEDOT:PSS suspension was spincoated at 2400 rpm for 30 seconds and annealed at 100°C in air for 15 min. After cooling down, the substrates were transferred to a nitrogen filled glovebox.

The mixed Sn-Pb perovskites were prepared from two stock solutions: $FA_{0.75}Cs_{0.25}PbI_3$ and $FA_{0.75}Cs_{0.25}SnI_3$ and mixed in 60/40 (Sn/Pb mol/mol) ratio. The individual stock solutions were prepared as follows:

**$FA_{0.75}Cs_{0.25}PbI_3$**: 0.75 mol FAI (greatcellsolar), 0.25 mmol CsI (Simga-Aldrich), and 1.03 mmol $PbI_2$ (Alfa-Aesar) were mixed in 0.75 ml and 0.25 ml dimethylformamide (DMF) and dimethyl sulfoxide (DMSO) (both anhydrous, Sigma-Aldrich).

**$FA_{0.75}Cs_{0.25}SnI_3$**: 0.75 mol FAI, 0.25 mmol CsI, 1.1 mmol $SnI_2$ (Sigma-Aldrich), and 0.1 mmol $SnF_2$ (Sigma-Aldrich) were mixed in 0.75 ml and 0.25 ml DMF and DMSO.

[1] Two substrates were spin coated with each polymer-fullerene concentration. The substrates were scratched forming an empty channel. The channel depth is then measured with the profilometer, generating a step-like profile. The height difference between the scratched channel and the spincoated layer gives the film thickness. This procedure is repeated multiple times each sample.

Both solutions were prepared inside the gloveboxes, stirred for $\sim 3$ hours at room temperature prior to mixing and used quickly after preparation of the target mixtures.

The perovskite layers were deposited inside the glove box by dispersing adequate amounts (e.g. $100\,\mu$l for a $2.5 \times 2.5\,\mathrm{cm}^2$ substrates and $20\,\mu$l for the EDMR substrates) of the solution and spincoating at 6000 rpm for 35 seconds. After the spincoating the substrates were quickly immersed in a bath of anhydrous anisole (Sigma-Aldrich) for $\sim 30\,s$, blown dry with an $N_2$ gun and annealed at 75°C for 30 minutes.

The substrates were transferred to an evaporation chamber, where 30 nm $C_{60}$ (creaphys), 8 nm 2,9-dimethyl-4,7-diphenyl-1,10-phenanthroline (BCP) (Sigma-Aldrich) and 100 nm Cu (Sigma-Aldrich) were evaporated at $< 10^{-6}$ mbar. The individual deposition rates were 0.1, 0.2 and 0.5 Å/s, respectively.

The contacting and sealing procedures were done as described previously for the organic BHJ solar cell.

### 4.1.5 Measuring *I-V* Characteristics

The solar cells were tested immediately after preparation (and before contacting and encapsulation) inside the glove box with 2-point contacts connected to a source measure unit (2 channel Keithley 2612B). Illumination is realized by a 1 W LED lamp.

The *I-V* characteristics of the the solar cell inside the resonator are measured by a Keithley source measuring unit (2611A). This is an important and crucial procedure to do before and after an experiment to examine whether the device is still operating and whether the experiment has influenced the working potential of the cell. The *I-V* characteristics are in addition recorded whenever the measurement conditions affecting the resonator, and hence the solar cell, environment are changed (i.e. temperature, light source etc.).

The obtained *J-V* parameters given in Table 7.1 of section 7.2 for the Sn-Pb perovskite solar cells were measured on a standard $2.5 \times 2.5\,\mathrm{cm}^2$ geometry. The measurements were performed directly after preparation in the laboratories of the group of Prof. Dr. Neher. The *J-V* scans were performed under $N_2$ atmosphere with a Keithley 2400 source measure unit, while the substrates were Peltier cooled to 25°C. The illumination source was a filtered Oriel class AAA Xenon lamp and the intensity was monitored simultaneously with a Si reference cell. The calibration was done with a KG5 filtered reference silicon solar cell (calibrated by Fraunhofer ISE) [92].

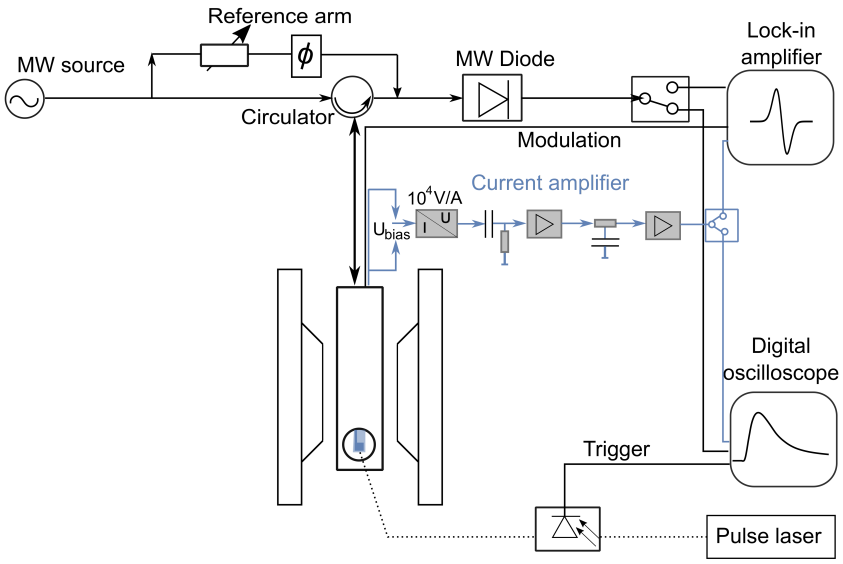


**Figure 4.1:** The cwEPR and trEPR setup. The cwEDMR and trEDMR detection follows the blue connection towards a current amplifier. The amplification scheme is shown in by the grey circuit symbols.

## 4.2 Experimental Methods

This section outlines the experimental methods used in this thesis. Mainly EPR and EDMR spectroscopic techniques were employed. The combined EPR and EDMR setup for continuous wave and transient detection is shown in Figure 4.1 illustrating the EPR (black) and EDMR (blue) detection paths. In addition, Density Functional Theory (DFT) calculations are described as used for the spiro-OMeTAD study presented in chapter 5.

### 4.2.1 cwEPR Setup

Continuous wave (cw)EPR refers to the application of a microwave, constant in amplitude and frequency, to the sample, while sweeping the magnetic field $B_0$. The sample is placed in the center of the cavity, where incoming microwaves, produced by the microwave source, irradiate the sample. The dimensions of the cavity depend on the target frequency to be used during a measurement. The microwaves stimulate the absorption in the sample and once at resonance at a specific magnetic field strength, standing waves are produced in the cavity. Standing electromagnetic waves have their electric and magnetic component exactly out of phase. This means that ideally the sample is placed in the electric field minimum and magnetic field maximum.

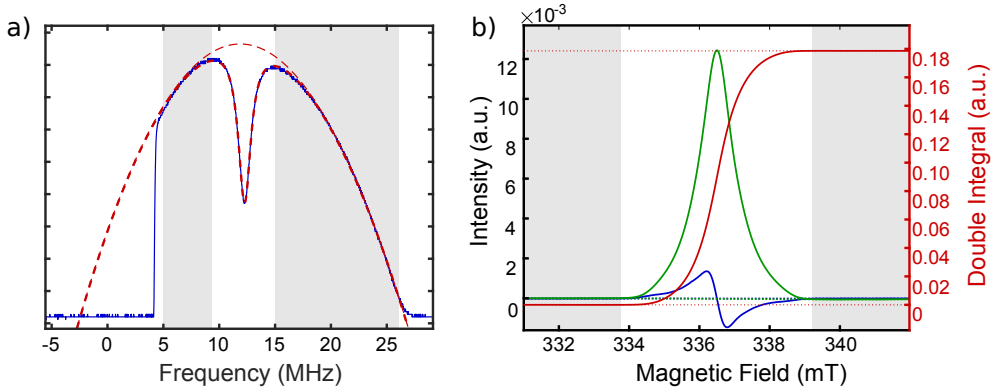


**Figure 4.2:** a) An example tune picture of a critically coupled resonator. The blue line shows the resonance dip resulting from the sample inside the resonator. The red-dashed line shows the fit, from which the $Q$-factor was determined. b) The signal amplitude is determined from the double integral (red). The blue spectrum is the measured cwEPR spectrum and the green is absorption spectrum obtained by integration.

The cavity is critically coupled to minimize the power reflection to the detector. This is done by matching the impedance of the cavity and the waveguide. At the resonance condition, the microwaves are absorbed by the sample, altering the properties of the resonator and microwave power is reflected from the resonator. These are then guided through a circulator to the detection diode. The function of the circulator is to separate the waves going to and out of the cavity and guarantees that only microwaves reflected back arrive at the diode detector. For optimum sensitivity, the diode is biased to its linear working regime and is achieved by the reference arm that supplies the detector with a bias. Additionally, a phase shifter is employed to make sure the reflected and reference arm microwaves are in phase when the detector combines the two signals.

To increase SNR, phase sensitive (lock-in) detection is employed. This entails the modulation of the magnetic field with a sinus wave, typically at a frequency of 100 kHz and an amplitude $B_m$. At the resonance signal, the field modulation sweeps through parts of the signals and the amplitude of the signal reflected back by the resonator is modulated at the same frequency. The steeper the signal, the larger the amplitude of the output signal. The signal output is then obtained as the derivative of the absorption spectrum. The lock-in amplifier produces a current that is proportional to the amplitude of the modulated signal. The reference current is compared to the modulated signal and extracts only the signals that have the same frequency and phase as the field modulation. This allows the amplification of relevant signals and the suppression of noise.

### 4.2.2 Quantitative EPR

Since EPR directly probes the spin, it can be used to determine the spin count in a sample. The information is entailed in the cwEPR spectrum [76]. In order to analyze the EPR spectrum quantitatively, certain factors must be considered when measuring the spectra.

#### Microwave Attenuation

It is important to measure the EPR spectrum at a microwave power where the line intensity does not saturate. In the absence of saturation, the spectrum intensity increases linearly with the square root of the applied microwave power.

#### The Q-Factor

The Quality factor (Q-factor) of the resonator indicates how efficiently the resonator stores the resonance energy, which is the microwave energy. It is defined as:

$$Q = \frac{2\pi \times \text{energy stored}}{\text{energy dissipated per cycle}} \tag{4.1}$$

where the energy dissipated per cycle is equal to the amount of energy lost during one microwave period. Loss in energy is caused due to the generation of electrical currents by microwave irradiation which in turn generate heat. This can happen if the sample is extremely conductive, reducing the quality of the cavity. The spectrometer sensitivity increases with the Q-factor. The signal intensity depends on the Q-factor. Therefore information on the Q-factor is needed for quantitative EPR.

#### Determining Spin Concentrations

In this work, quantitative EPR is used to determine spin concentrations in doped spiro-OMeTAD samples. The spin-counting analysis was done employing the spin-counting toolbox in Matlab [93]. Figure 4.2a indicates a plot of reflected power vs. microwave frequency of a critically coupled resonator. The experimentally measured resonator dip (blue line) was simulated by a Lorentzian function (red dashed line) and the quality factor of the resonator is determined as the resonance frequency of the cavity divided by the width of the cavity dip at half of its height for reflected power (obtained from the fit) [76]. The recorded derivative spectra were background corrected followed by double integration, giving the signal area DI as demonstrated in Figure 4.2b. A calibration was performed using a reference sample with known spin count (4-Hydroxy-TEMPO dissolved in toluene) to determine the constant $c_{\text{calib}}$, which was then used to calculate the number of spins $N_s$ as:

$$N_s = \frac{DI}{c_{\text{calib.}}\sqrt{P_{MW}}B_m Q n_B S(S+1)[G_R C_t N_{\text{scans}}]} \tag{4.2}$$

where $P_{MW}$ is the applied microwave power, $B_m$ the used modulation amplitude, $n_B$ the temperature-dependent Boltzmann factor, $G_R$ the receiver gain and $C_t$ the

conversion time [76]. The spin concentration $C$ is determined as follows:

$$C = \frac{N_s}{V_{\text{film}}} \tag{4.3}$$

where $V_{\text{film}}$ is the spiro-OMeTAD film volume of the sample and is defined as

$$V_{\text{film}} = \frac{m_{\text{spiro-OMeTAD}}}{\rho_{\text{spiro-OMeTAD}}} \tag{4.4}$$

with the density of spiro-OMeTAD $\rho_{\text{spiro-OMeTAD}} = 1.82\text{g/cm}^3$ [94] and mass $m_{\text{spiro-OMeTAD}}$.

### 4.2.3 cwEDMR Setup

To perform a cwEDMR experiment, the EPR setup can, to a great extent, be adopted with a few modifications in the detection scheme. This is shown in Figure 4.1 following the blue detection path. In this setup the solar cell is connected with cables going outside of the resonator to a current amplifier. The current amplifier has two functions: (i) it contains a steady voltage source, that supplies the sample with a bias voltage and (ii) it amplifies and transforms the current flowing through the sample into a voltage signal. The current amplifiers used for EDMR measurements in this thesis are from Elektronik Manufaktur Mahlsdorf.

The applied voltage $U_{bias}$ is split into two voltages $\pm U_{bias}/2$ and applied in a symmetrical configuration to the ground potential. The total current flowing through the sample is then obtained by subtracting the two currents resulting from $+U_{bias}/2$ and $-U_{bias}/2$. This allows the suppression of noise and interfering signals coming from outside of the detection path. The response signal from the sample is first passed trough a trans-impedance amplifier that converts the current with the factor $10^4\,\text{V/A}$ to a voltage. The DC component flows through a low-pass filter and is read out on the connected multimeter. The AC component goes through a high-pass filter, that filters out frequencies below a certain set cut-off frequency. This signal is amplified, then passed through a low-pass filter and amplified for a second time. The low-pass filter can be varied to monitor the time resolution of the detection.

As in conventional cwEPR, phase-sensitive detection is also used in cwEDMR to enhance SNR. The modulation frequency used is usually in the lower range of $4-20\,\text{kHz}$ and is often chosen such that the output signal is maximized. There are, however, reports showing modulation frequency dependencies on the sample current [95]. The modulation frequency should therefore not be ignored and its dependence on the cwEDMR signal should be examined.

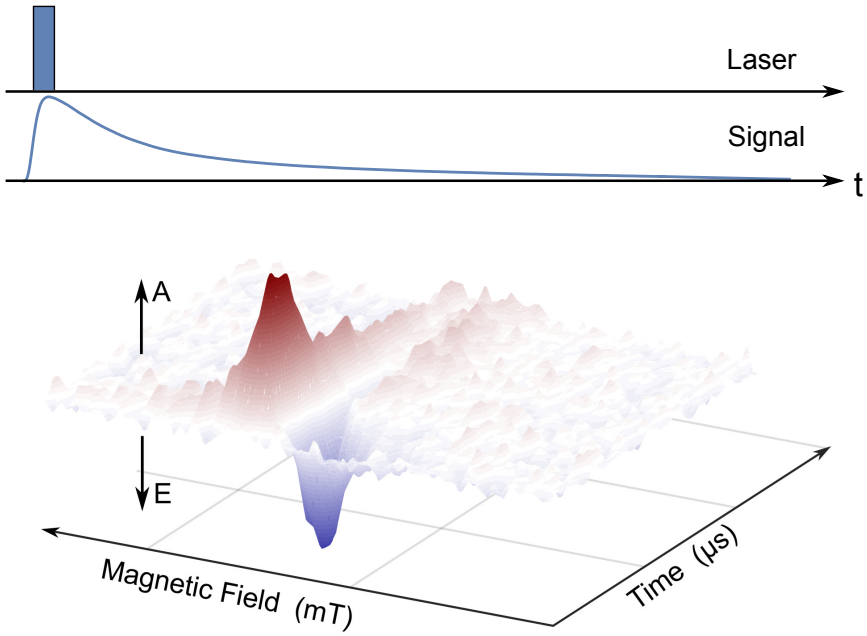


**Figure 4.3:** Spectrum obtained in trEPR measurement. The detection occurs with delay after a laser flash on a $\mu$s scale. The magnetic field, time and signal intensity relation is shown. The arrows indicate absorptive (A) and emissive (E) features.

### 4.2.4 Combined Transient EPR and EDMR Setup

Time-resolved or transient (tr)EPR and trEDMR measurements are ideal to study dynamics of light-induced paramagnetic states after optical excitation and their involvement in spin-dependent processes. The setup employs continuous wave irradiation, similar to cwEPR. A laser flash induces paramagnetic centers in the material. The transient microwave absorption is detected after the light flash with a fast oscilloscope. The time trace recorded contains the generation and decay of the signal with time. By scanning the magnetic field, a relation is obtained, where for each magnetic field position, the signal intensity over a time interval is recorded. This is shown in Figure 4.3. The detected signals correspond to absorptive (A) and emissive (E) features as indicated by the arrows.

Similar to trEPR, time resolved EDMR can be employed to detect the photocurrent response to spin manipulation. The same setup as for trEPR is used enabling combined detection. This allows the correlation between signals observed in trEPR and trEDMR. The sign of the resonant current change is correlated to current quenching or current enhancing effects. For trEDMR detection, the sample requires electrical contacts, which are connected to a current amplifier. The same current amplifier can be used as in cwEDMR experiment. Only the AC current is amplified and ap-

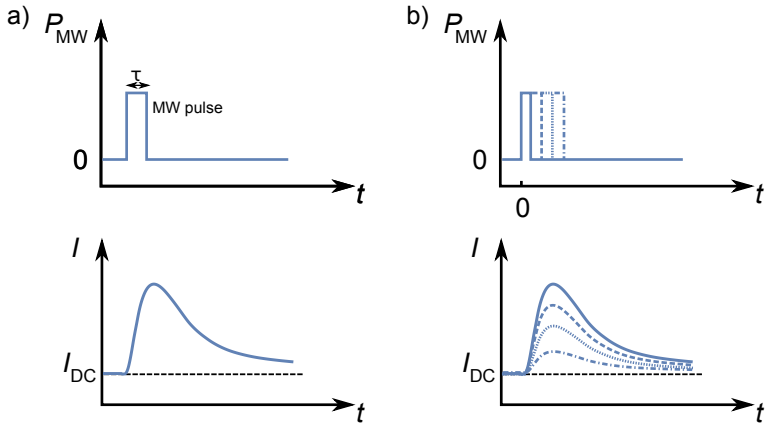


**Figure 4.4:** Pulsed EDMR experiments: a) a short microwave pulse is applied illustrated by the upper plot and the current response as a function of time after the pulse is given in the lower plot b) The microwave pulse length is incremented. The current response of the sample is shown after each incrementation in the lower plot.

pears as the photo-transient on the fast oscilloscope. The photocurrent response is recorded with respect to the magnetic field.

### 4.2.5 Pulsed EDMR Experiments

In pulsed (p)EDMR experiments, a short microwave pulse is used to drive spin transitions that influence the current of a device. The change in sample conductivity resulting from changes in spin-dependent recombination and hopping rates is detected as a function of time after the applied pulse. Initially, the spins are aligned parallel to the direction of a magnetic field $B_0$. A microwave pulse $B_1$ of length $\tau$ drives the spin ensemble into a non-steady state. Directly after the pulse, a change in the current $\Delta I(t)$ induced by the spin-dependent processes is detected. Due to spin-relaxation, the current will return to its steady state value with time. Similar to the above describe transient experiment, the current response as a function of time after the the microwave pulse is recorded (Figure 4.4a) over a selected magnetic field range.

#### Rabi Oscillation Experiment

In a Rabi oscillation experiment, the length of the microwave pulse ($\tau$) is incremented and the transient current response $\Delta I(t)$ is recorded (Figure 4.4b). Integrating over a fixed time interval yields the charges $\Delta Q(\tau)$ (within the integration window equivalent to the length of the pulse $\tau$) involved in a resonant transition. Plotting $\Delta Q$ with respect to $\tau$ reveals the behavior of coherent spin motion in the form of Rabi oscillations, as the spin flip or nutation angle is proportional to the pulse length. The inverse of one Rabi cycle gives the Rabi frequency of the driven spin species.

In the case of having more than one spin species, the spins will have different Rabi frequencies. At weak $B_1$ excitation, only one of spins is driven at the frequency $\Omega_1 = \gamma B_1$, where $\gamma$ is the gyromagnetic ratio. In the case of a weakly coupled spin pair and the application of a strong $B_1$ field, a coherent spin motion of both carriers is driven. This leads to the doubling of the Rabi oscillation $\Omega = 2\gamma B_1$.

### 4.2.6 DFT Calculation

Chapter 5 presents results obtained from DFT calculations performed on spiro-OMeTAD molecule in different environments using the quantum chemistry program ORCA (program version 4.0.1.2) [96, 97].

To model the spiro-OMeTAD conformation in solution, the molecule was symmetrized (by combining two identical arms as described in reference [98]) resulting in $C_2$ symmetry. The geometry of spiro-OMeTAD in the solid state was extracted from single-crystal X-ray diffraction characterization data by Shi et al. [98]

DFT single-point calculations for the determination of the magnetic properties were performed directly on the spiro-OMeTAD single crystal and symmetrized geometries. The range-separated hybrid functional $\omega$B97X-D3 [99] with the default range separation parameter $\omega = 0.25\,\mathrm{bohr}^{-1}$, the atom-pairwise dispersion correction with the Becke-Johnson damping scheme, D3BJ [100, 101], and the basis set EPR-II [102] were utilized for the calculations. The parameters obtained from the DFT calculations are shown in table C.1 for spiro-OMeTAD in the solution model and in table C.2 for spiro-OMeTAD in the single crystal structure.

## 4.3 EPR Spectrometers and Other Intrumentation

**Lyra**
Laboratory-built X-band spectrometer equipped with an X-SHQ resonator (Bruker 4122-SHQ-E) suitable for quantitative cwEPR measurements. The magnetic field was monitored by a field controller (Bruker BH15) and the microwave generation and detection was achieved with a Bruker microwave bridge (Bruker ER 048 R). Magnetic field modulation in combination with lock-in detection was employed using a lock-in amplifier (Stanford Research SR810) and a modulation amplifier (Wangine WPA-120).

**Isaak**
Laboratory-built spectrometer capable of cwEPR and trEPR measurements at X- and Q-band. Q-band measurements were performed using a home-built cylinder resonator and for X-band measurements a dielectric ring resonator (Bruker ER

4118X-MD5) was used. The magnetic field was monitored by a field controller (Bruker ER 032M) and the microwave generation and detection was achieved with a Bruker microwave bridge (Bruker ER 048R). The transient microwave response for trEPR measurements was recorded by a digital oscilloscope (LeCroy WaveRunner 104MXi). In the case of cwEPR and cwEDMR experiments field modulation was employed using a lock-in amplifier (Stanford Research SR830). The cwEDMR and trEDMR experiments were performed on this spectrometer using the same devices with additionally a current amplifier (Elektronik Manufaktur Mahlsdorf).

**Bruker Elexsys E680**
X- and W-band Bruker spectrometer. The pulse EDMR measurements presented in Chapter 7 were performed on this spectrometer at X-band. The resonator used is a dielectric ring ER 4118X-MD5. The resonator has a window allowing illumination of the sample. The microwave pulses were generated by a 1 kW TWT microwave amplifier (Applied Systems Engineering, Inc Model 117).

### 4.3.1 Light Sources

**Cooled White-Light:** Light from a DC regulated 150 W halogen light with IR filter from Polytech (DCR IV). The illumination intensity can be varied between 100 to $\sim 50\%$.

**Continuous Wave Diode Laser:** Laser diode (DJ532-40) from ThorLabs with leasing wavelength of 532 nm and a beam diameter[2] $d \approx 6$ mm was operated at an optical power output $P_0 = 40$ mW. The photon flux density per second is:

$$\Phi = \frac{P_0/E_{\lambda=532\text{nm}}}{\pi d^2} = 1.7 \cdot 10^{27} \frac{\text{photons}}{\text{s} \cdot \text{cm}^2} \tag{4.5}$$

where $E_{\lambda=532\text{nm}}$ is the energy of a green photon. The laser diode was controlled by a laser diode driver (LDC205C) and a 12 W temperature controller (TED200C).

**Pulsed Laser:** 532 nm diode-pumped 100 Hz ND-YAG laser from Atum Titan AC 15MM SHG was used for transient measurements.

[2]Beam diameter $d$ measured at a distance of $\sim$ 1m.

Chapter 5

# Doping of Spiro-OMeTAD

*The hole-transport layer in perovskite solar cells has been proven to play a significant role in achieving high efficiencies and stabilities. The most commonly used hole transport layer in perovskite solar cells is spiro-OMeTAD. However, to enable highest efficiencies, it requires careful chemical doping to increase its conductivity. This chapter demonstrates the use of EPR spectroscopy to investigate spiro-OMeTAD doped with two of the most commonly used p-dopants: Li-TFSI and FK209. In the first part of this chapter, doping efficiencies for the mentioned additives are determined and their role in doping spiro-OMeTAD is discussed. In the second part, a multifrequency EPR analysis of doped spiro-OMeTAD solutions and films is presented.*

## 5.1 Introduction to Spiro-OMeTAD

Perovskite-based solar cells (PSCs) have ignited a competition for record power conversion efficiencies (PCEs) since their first successful implementation in 2009 [10]. Their PCE has risen to over 23% [12] within less than a decade, which, in addition to their inexpensive and facile fabrication from solution [103, 104], and their unique optoelectronic properties [105, 106], makes them promising candidates for third generation solar cells. The architecture of a typical PSC consists of the perovskite material sandwiched between electron and hole transport layers (ETLs and HTLs). These layers function as charge selective pathways for photogenerated charge carriers towards the electrodes and play a fundamental role in increasing efficiency and stability [62, 107, 108]. A promising route to further enhance photovoltaic performance is by optimizing the hole collection at the perovskite/HTL interface.

The organic molecule 2,2',7,7-tetrakis(N,N-di-p-methoxyphenylamine)-9,9'-spirobifluorene, known as spiro-OMeTAD and shown in Figure 5.1, has been the hole transport material of choice when striving for high PCEs [36, 109, 110]. As in its pristine form spiro-OMeTAD suffers from low conductivity, p-doping has become a decisive and standard process in improving conduction [111–113].

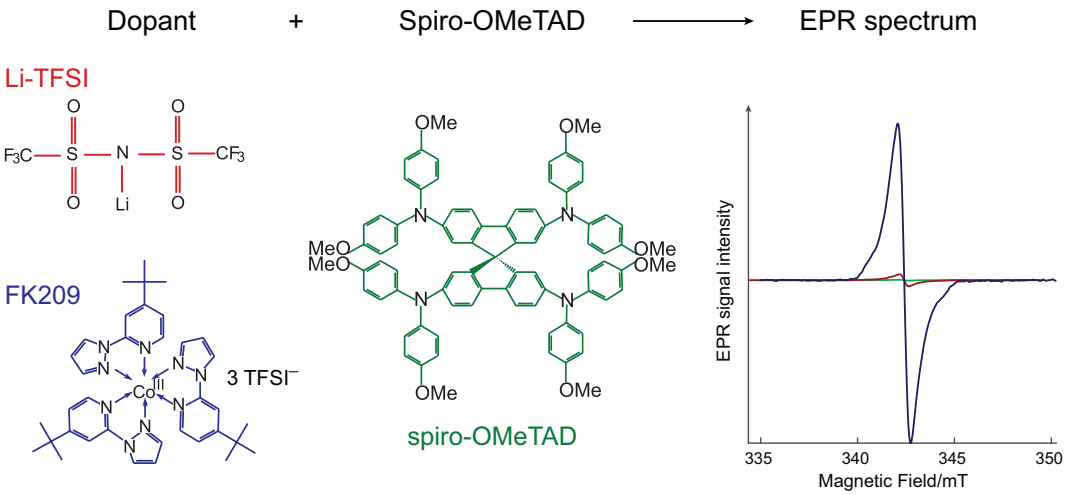


**Figure 5.1:** Left: chemical structures of the dopants Li-TFSI (red), FK209 (blue) and the hole transporting molecule spiro-OMeTAD (green). Right: the effect of doping as detected in continuous wave EPR (cwEPR). The green spectrum is the undoped spiro-OMeTAD spectrum, the red and blue spectra are the signals after doping with Li-TFSI or FK209, respectively, at a doping ratio of 1:100. The largest increase in signal intensity is seen for FK209.

Several groups reported on increased conductivities induced by lithium bis-(trifluoromethylsulfonyl)-imide (Li-TFSI) in combination with light and oxygen [28, 112, 114]. This type of doping under photo-oxidation, however, is inconvenient as firstly it is hardly controllable and secondly many organic compounds are prone to degradation upon exposure to oxygen. Therefore, a different dopant based on a Co(III)-complex, tris(2-(1H-pyrazol-1-yl)- 4-tert-butylpyridine)cobalt(III)-$TFSI_3$, generally denoted as FK209, was introduced due to its capability to efficiently p-dope spiro-OMeTAD without additional conditioning [32, 39, 115]. Currently, spiro-OMeTAD is usually doped by including both Li-TFSI and FK209 [32, 36, 39, 116]. It is, however, unclear to what extent each added p-dopant enhances the charge carrier concentration in spiro-OMeTAD.

Numerous optical spectroscopy studies on (doped) spiro-OMeTAD have provided the current understanding on the physical properties of the molecule and on the effect of doping the material by addition of the same p-dopants investigated here [28, 32, 115, 117]. While these optical measurements are a rather indirect way to analyze doping processes, Electron Paramagnetic Resonance (EPR) spectroscopy is used here to directly probe electron spins and quantify the amount of charges introduced by doping [118]. Additionally, this technique is particularly advantageous in cases where the sample has scattering properties or is opaque, preventing accurate optical measurements [76]. With regards to conductivity studies, EPR spectroscopy allows to quantitatively investigate the extent of doping independent from the effects on the charge mobility and hence conductivity.

In the first part of this chapter, we describe the use of continuous wave EPR spectroscopy (cwEPR) to quantitatively determine absolute charge carrier densities introduced by doping. The high sensitivity of this method allows the investigation of doping ratios covering the range between $10^{-6}$ and 1 dopant per spiro-OMeTAD molecule, broader compared to optical studies. Doping efficiencies of Li-TFSI and FK209 doped spiro-OMeTAD of less than 2% and roughly 81% respectively, are determined. We identify FK209 as the main doping agent. In addition, we find that in Li-TFSI doped spiro-OMeTAD, oxygen and light do not cause a significant further increase in spin concentration. The role of Li-TFSI is evaluated and we conclude that its overall effect in PSC is related to its capability of enhancing hole mobility and improving electron transfer to the TCO layer due to $Li^+$ migration, rather than its doping of spiro-OMeTAD.

In the second part, the focus lies on the interpretation of the measured EPR spectra of doped spiro-OMeTAD. This involves the analysis of X-band (9.6 GHz) and Q-band (34 GHz) spectra obtained from liquid-phase and film samples. The detected signal was assigned to the hole on the spiro-OMeTAD molecule. Comparison with DFT calculations provided information on its microscopic environment and allowed the interpretation of the observed spectral shape, which is mainly determined by the hyperfine interaction with the nitrogen nuclei.

## 5.2 Determining Doping Efficiencies

With the help of quantitative EPR, the extent of doping of spiro-OMeTAD by Li-TFSI and/or FK209 is elucidated by measuring the spin concentration as a function of dopant concentration. This approach requires knowledge of the number of detected EPR signals, i.e. whether both host and dopant or just one of them contributes to the EPR spectrum. Based on a detailed analysis discussed in the next section, the observed EPR signal was assigned to the hole introduced in spiro-OMeTAD as a result of p-doping. We note at this point that in the case of direct overlap between the EPR signal of the hole on the host and the signal due to the unpaired electron on the dopant, a maximum error of a factor of two in the spin concentration would result. Since the detected spins originate from the charge carriers in the system, the determined spin concentrations provide a direct measure of the charge carrier concentration. Spin and charge carrier concentrations are generally equivalent, except in cases where spin paired species, such as bipolarons, which do not contribute to the EPR signal, are present. Therefore, the spin concentrations reported below are best considered as lower limits of the charge carrier concentrations.

Figure 5.2 displays the dependence of the spin concentration on the individual Li-TFSI and FK209 content in spiro-OMeTAD films. A significant intrinsic spin con-

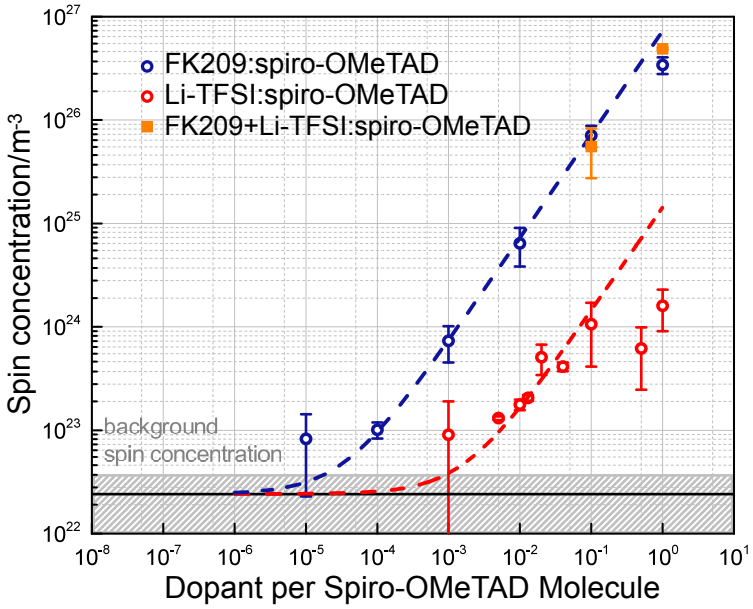


**Figure 5.2:** The total spin concentration determined by quantitative EPR measurements for spiro-OMeTAD films prepared with different concentrations of FK209 (blue circles), Li-TFSI (red circles) and the combination of the two (orange squares, x-axis refers to FK209 dopant only). The sample preparation and measurements were performed under inert atmosphere. The error bars were obtained from the standard deviation for four measurement series. The background spin concentration was measured on pristine spiro-OMeTAD and is indicated by the black solid line. The grey area includes the standard deviation. The blue and red dashed lines show the fit from Equation 5.1.

centration in pristine spiro-OMeTAD was determined. This is referred to as the background spin concentration and is marked in grey in Figure 5.2. The pure Li-TFSI and FK209 materials, prepared from acetonitrile solutions, are EPR silent. The observation of spins in undoped, pristine organic molecules is common and usually ascribed to intrinsic charges, impurities, or defects [118–120].

For the dopant FK209, the quantitative EPR data yield a linear relation on the log/log plot between the spin concentration and doping ratio within the range from 1:10 down to 1:10 000. It implies that doping is efficient over a very broad doping range. A slight deviation from this linearity is observed for the highest doping ratio. For doping concentrations below 1:10 000, the spin concentration begins to approach the intrinsic one. The doping series was prepared four times and each point in the graph represents the mean over multiple measurements with the error bars indicating the standard deviation. The doping efficiency is determined from a fit to:

$$C(N_{\text{dop.}}) = C_{\text{bg}} + \eta \frac{N_{\text{dop.}}}{V} \tag{5.1}$$

Here, $C(N_{\text{dop.}})$ is the spin concentration plotted in Figure 5.2, $C_{\text{bg}}$ is the background spin concentration of the pristine spiro-OMeTAD, $\eta$ is the doping efficiency, $N_{\text{dop.}}$

is the number of dopant molecules, and $V$ is the sample volume. From this we determine a doping efficiency of $\eta_{\text{FK209}} = (81 \pm 12)\%$ for FK209.

In comparison, doping with Li-TFSI could only be detected down to a doping ratio of 1:1 000, as at lower doping ratios the signal is indistinguishable from the background signal. In addition, a deviation from the linear behavior of spin concentration as a function of doping ratio is observed for ratios higher than 1:10. A similar saturation behavior was previously observed in conductivity measurements [112]. The doping by Li-TFSI is thus quantifiable in a narrower range compared to FK209. Nonetheless, we determine an average doping efficiency $\eta_{\text{Li-TFSI}} = (1.6 \pm 0.2)\%$ for Li-TFSI-doped spiro-OMeTAD. Earlier EPR studies on the efficiency of Li-TFSI doping reported $\eta_{\text{Li-TFSI}} = 0.45 - 0.90\%$ [114]. However, in that case the efficiency was obtained from samples of ∼1:2 doping ratio, which is within the range where we observed a saturation of the spin concentration.

Finally, by adding both Li-TFSI and FK209, it is expected that the total doping efficiency will follow the sum of both $\eta_{\text{Li-TFSI}}$ and $\eta_{\text{FK209}}$. However, since $\eta_{\text{FK209}}$ is more than 50 times larger, the total efficiency will likely amount to $\eta_{\text{total}} \approx \eta_{\text{FK209}}$. Two samples were prepared to verify this hypothesis. The first sample follows the standard doping recipe with doping ratios of 1:2 for Li-TFSI: spiro-OMeTAD and 1:10 for FK209:spiro-OMeTAD. The second sample was prepared with a doping ratio of 1:1:1 for Li-TFSI:FK209:spiro-OMeTAD. The results are shown in orange in Figure 5.2 with reference to the ratio of FK209 to spiro-OMeTAD. As predicted, the spin concentrations are not further enhanced after addition of Li-TFSI, showing that Li-TFSI is redundant for doping in the presence of FK209. Thereby, we identify FK209 as the predominant p-dopant.

The determined doping efficiency for Li-TFSI, $\eta_{\text{Li-TFSI}} = (1.6 \pm 0.2)\%$, is surprisingly low. Literature studies report on improved doping upon exposure to oxygen and light. It was shown that under ambient conditions the number of spins in Li-TFSI-doped spiro-OMeTAD (doping ratio ≈1:2) increased by two orders of magnitude compared to the pristine material [114]. The results presented here indicate an enhancement of charge carrier concentration by ∼ 1.6 orders of magnitude in the absence of additional conditioning. To examine whether a further increase can be obtained in the presence of oxygen and light, the number of spins in a film sample of 1:2 doping ratio was monitored over a period of 27 hours under ambient conditions. Throughout the measurement the sample was exposed to air. During the first 12 hours, the sample was illuminated by a cold white light source, followed by 12 hours of dark measurements and finally illumination for the remaining three hours. The results in Figure 5.3a show that over this period of time, a variation of 8% in the number of spins is measured. This indicates that exposure to oxygen and light compared to no exposure does not lead to a significant increase in the spin concentration. The same measurement was performed without illumination for a sample with a lower doping concentration, 1:10 Li-TFSI:spiro-OMeTAD. Figure 5.3b

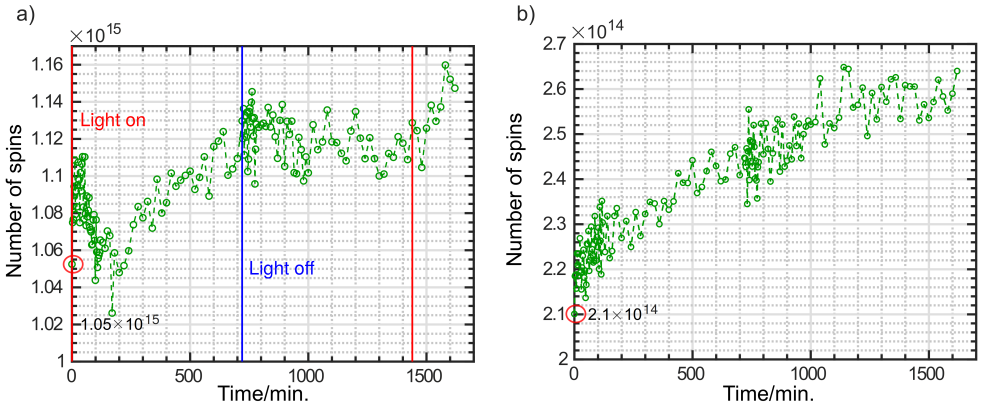


**Figure 5.3:** Number of spins measured over ∼27 hours for Li-TFSI doped spiro-OMeTAD film samples exposed to air. a) Measurement under illumination or in the dark for Li-TFSI-doped spiro-OMeTAD with a doping ratio of 1:2. b) Measurement in the dark for Li-TFSI:spiro-OMeTAD with a doping ration of 1:10. The red circle indicates the first measurement point with the spin number of spins given in the graph.

demonstrates that although an increasing trend is measured, it only amounts to 18% higher charge carrier concentrations.

Conductivity measurements with a mercury probe setup on spin-coated films were performed directly after fabrication and showed an enhancement of more than three orders of magnitude between undoped ($7 \cdot 10^{-8}$ S/cm) and Li-TFSI-doped spiro-OMeTAD ($2 \cdot 10^{-4}$ S/cm), which agrees with previous reports [112, 121, 122]. After 24 hours and storage under ambient conditions, the conductivity of the undoped sample had increased to ($2 \cdot 10^{-7}$ S/cm), whereas the Li-TFSI-doped sample's conductivity remained approximately unchanged at three orders of magnitude larger values ($7 \cdot 10^{-5}$ S/cm). Based on the increase in conductivity by two orders of magnitude originating from the introduction of additional holes to spiro-OMeTAD by doping with Li-TFSI (as shown in figure 2 and discussed above) and given that the conductivity is the product of charge carrier density and mobility, it follows that the charge carrier mobility is enhanced by at least one order of magnitude. This was also previously shown and discussed by Snaith et al. [121] The proposed mechanism can be described by the broadening of the density of states (DOS) distribution and filling of tail states by doping of disordered organic materials: the addition of Li-TFSI broadens the DOS distribution and introduces acceptor anions which generate strong Coulomb fields, forming deep Coulomb trapping potentials at the tail of the DOS distribution. This is accompanied by the filling of deep traps. As the charge density is also increased (particularly with higher doping concentrations), under equilibrium conditions, the carriers fill the deep states and shift the quasi-Fermi energy closer to the mobility edge. This leads to a higher average hopping rate and hence a higher carrier mobility [33, 123]. We note that if trap filling was the main effect causing the increase in conductivity, we would expect to see a larger increase in charge-carrier

concentration in the EPR experiments. Thus, our results indicate that classical trap filling in spiro-OMeTAD is at least not the only efficiency-increasing mechanism.

To summarize the results, it was found that additional conditioning with oxygen and light does not further enhance the spin concentration in Li-TFSI doped spiro-OMeTAD. If one seeks to efficiently p-dope spiro-OMeTAD, FK209 is the far better additive with its ability to dope at an efficiency of about 81%. The role of Li-TFSI (in the absence of oxygen) in the recipe remains to be clarified. In addition to enhancing the hole mobility, it is known that Li-TFSI affects the charge transport at the $TiO_2$ surface of the solar cell, if employed as the electron transport material [112, 124] $Li^+$ ion migration towards the transparent conductive oxide surface, caused by the built-in potential under illumination of the solar cell, facilitates photocurrent generation. Furthermore, Li-TFSI causes a shift in the surface potential of the $TiO_2$, which in turn allows a more efficient electron transfer [125, 126]. These results imply that the beneficial effects on device performance observed by including Li-TFSI in the hole transport layer of perovskite solar cells are not solely related to the introduction of additional charge carriers to spiro-OMeTAD.

## 5.3 Spiro-OMeTAD EPR Signature

In the remaining part of this chapter the origin of the spiro-OMeTAD EPR signature arising upon doping with Li-TFSI and FK209 is studied. In addition to X-band measurements (at 9.6 GHz) discussed in the previous section, Q-band measurements (at 34 GHz) were also performed for increased resolution and to aid in the interpretation of the observed spectral features. Additional insight is also provided by measurements in solution, where any existing anisotropies are averaged out by molecular motion, thus simplifying the spectrum. The spectra recorded for spiro-OMeTAD solutions and films doped with FK209 and Li-TFSI are compared in Figure 5.4. The same EPR signature is observed independent of the dopant used, indicating that the same paramagnetic species is generated in both cases.

The X-band solution EPR spectra shown in Figure 5.4a reveal a single EPR line with partially resolved hyperfine structure assigned to the interaction between the unpaired electron spin and the four nitrogen nuclei on the spiro-OMeTAD. The isotropic hyperfine coupling can be determined from the line splitting and is related to the spin density distribution in the molecule, which will be discussed later in this article. The corresponding Q-band spectra (shown in Figure 5.4b) do not show any significant difference in spectral shape, in particular, the spectral width is comparable. In case of contributions of different paramagnetic species (e.g. electron and hole) with different characteristic $g$-values, a broadening or splitting of the EPR line would be expected at Q-band compared to X-band due to the field dependence of the electron Zeeman interaction. The solution EPR data therefore supports the assign-

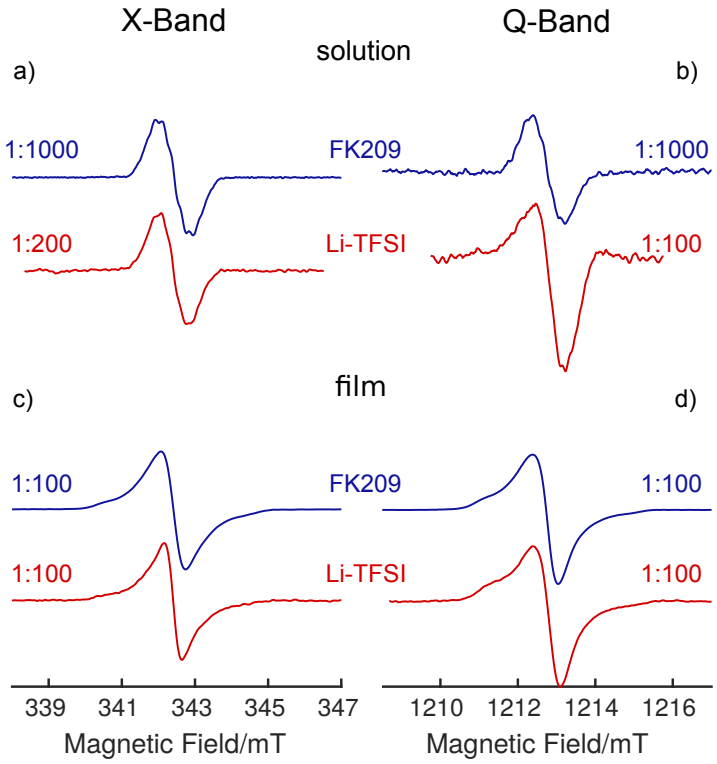


**Figure 5.4:** cwEPR spectra measured at X- (9.6 GHz) and Q-band (34 GHz) on doped spiro-OMeTAD solutions (a, b) and films (c, d) at room temperature. The dopants and doping concentrations are indicated in the respective color of the spectrum.

ment of the observed EPR signal to the hole on the spiro-OMeTAD molecule. The observed line width of the solution EPR spectra is due to unresolved proton hyperfine couplings and potentially dipolar interactions between charged spiro-OMeTAD molecules.

The X- and Q-band spectra recorded on doped films are shown in Figure 5.4c and d and consist of a narrow resonance signal and a shoulder on the low-field side. Since the Q-band solution spectra do not reveal broadening or a second signature, the low-field feature is interpreted as part of the same EPR signal due to the hole on spiro-OMeTAD. The similarity between the spectra recorded at the two different frequency bands indicates that the spectral shape is mostly dominated by the hyperfine interaction to the nitrogen nuclei. The small asymmetry observed in both cases, but more pronounced for the Q-band spectra, suggests the presence of a small $g$-anisotropy, which would be in agreement with the high symmetry of the spiro-OMeTAD molecule. The changes between the solution and solid-state spectra can be explained by the contribution of the anisotropic hyperfine interaction in films, while in solution only the isotropic component of the hyperfine interaction is observed. An overall increased line broadening for the film spectra is likely due to a combination of a distribution in $g$-values and hyperfine interactions, caused by

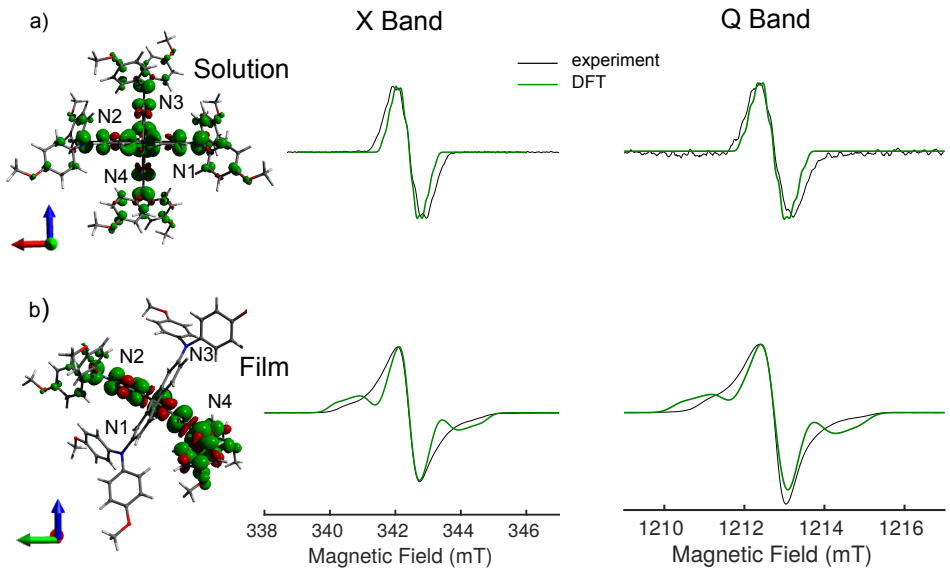


**Figure 5.5:** Spin density distributions calculated at the ωB97X-D3/EPR-II level for a symmetrized spiro-OMeTAD molecule and a molecule extracted from the crystal structure [98] and comparison of the experimental EPR spectra of spiro-OMeTAD doped with FK209 for a) solution (doping ratio 1000:1) and b) films (doping ratio 100:1) with simulations based on the parameters resulting from the DFT calculations (see main text for details). The simulation parameters are given Apendix C.

different environments of spiro-OMeTAD molecules within the disordered solution-processed film, and increased dipolar broadening due to decreased spatial separation of charge carriers, in particular for high doping concentrations. The spectra shown in Figure 5.4 were recorded for relatively low doping concentrations, for which spectral broadening due to spin-spin interactions should play a minor role [71].

With the clear assignment of the EPR signal observed for doped spiro-OMeTAD to the hole on the molecule, the signature of the electron generated in the doping process remains unidentified. The doping of Li-TFSI leads to the $Li^+$ cation and the TFSI anion [112], which are both diamagnetic and therefore EPR-silent. Doping with FK209 results in the reduction of $Co^{3+}$ to $Co^{2+}$ [115], where the former is diamagnetic and the latter is paramagnetic. However, the $Co^{2+}$ cation is present in a high spin configuration ($S = 3/2$) [127] and high spin $Co^{2+}$ systems are typically characterized by broad spectra due to large $g$-anisotropies and significant spin-orbit couplings [128]. Additionally, low temperatures are usually required to detect the signals due to fast relaxation. It is therefore not surprising that no contribution was detected at room temperature, in particular in the region around $g = 2$ shown in Figure 5.4.

The $g$-tensor and hyperfine parameters were calculated by DFT and compared to the experimental results to aid the understanding of the microenvironment of the charge carriers at the molecular level. In accordance with previous computational

studies [98], calculations were performed for two different geometries: for an ideal symmetrized molecule as a model of the average conformation assumed by spiro-OMeTAD in solution and for a molecule extracted from the single-crystal X-ray diffraction structure [129] as a model for the structure in the solid state. The resulting spin density distributions for the hole on spiro-OMeTAD are shown in Figure 5.5.

The simulations of the cwEPR spectra were performed using the EasySpin toolbox for Matlab [82]. Solution spectra were simulated using the isotropic simulation routine and film spectra were simulated with the solid-state simulation routine. The EPR parameters used for the simulations were directly imported from the DFT output file, only the Gaussian line width $\Delta B$ was adjusted to match the experimental results ($\Delta B = 0.21\,\mathrm{mT}$ for solution spectra and $\Delta B = 0.45\,\mathrm{mT}$ for films). The DFT-parameters used for the isotropic and solid-state simulation can be found in Appendix C

While the spin density is fully delocalized across the entire molecule in the solution phase model structure, in the crystal structure it is localized on a single arm. This is in agreement with the results of previous calculations [98, 129]. The significant hole density at the nitrogen atoms leads to large calculated hyperfine couplings that dominate the line shape of the EPR spectrum. Nitrogen has a nuclear spin $I = 1$ and hence the interaction with the unpaired electron leads to a splitting into $2nI + 1$ lines for solution EPR spectra. For a spin delocalized over both arms of the molecule and thus four equivalent nitrogen nuclei, this would lead to nine lines split by the isotropic hyperfine coupling, while delocalization over a single arm and therefore two equivalent nitrogen nuclei would lead to five lines with twice the splitting, since the isotropic hyperfine coupling is proportional to the spin density at the position of the nucleus. Due to inhomogeneous broadening, the hyperfine splitting is only partially resolved in the solution EPR spectra, nevertheless the presence of nine peaks can still be identified. Comparison of the experimental data with simulations based on the completely delocalized spin density is overall in good agreement with the experimental results (Figure 5.5 a), confirming delocalization of the charge over the whole molecule in solution.

For the EPR spectra recorded on doped films, a better agreement with the experimental results is obtained for a spin localized on half of the molecule, as predicted for the single crystal structure. In the solid state, the EPR spectrum is determined by the full anisotropic hyperfine tensor, containing both the isotropic hyperfine coupling and the dipolar electron-nuclear interaction, leading to the spectral shapes of Figure 5.5b. If considering a delocalization on all four nitrogen atoms with equally large hyperfine couplings, the orientation dependence of the hyperfine interaction inside the magnetic field would result in a spectrum of different shape. The overall width of the spectrum is determined by the largest hyperfine coupling and the reasonable agreement between simulation and experiment supports the predicted localization of the charge carrier on one half of the spiro-OMeTAD molecule. Considering an

ensemble of molecules with slightly different geometries and therefore different nitrogen hyperfine couplings would be a more accurate model of the disorder expected in a solution-processed film and would explain the larger broadening and less clearly resolved hyperfine structure in the experimental data, in particular at the extremes of the spectrum. It can also not be excluded that a superposition of solution and film simulations would produce better agreement with the measured film spectra. This would imply that molecules with completely delocalized spin density and molecules with charge carriers mainly residing on a single arm are both present in the film.

## 5.4 Conclusion

In conclusion, the doping efficiencies $\eta$ of the commonly used additives Li-TFSI and FK209 for spiro-OMeTAD doping were determined as $\eta_{\text{FK209}} = (81 \pm 12)\%$ and $\eta_{\text{Li-TFSI}} = (1.6 \pm 0.2)\%$. The results clearly indicate that FK209 is the main doping agent. Furthermore, doping by means of both additives will not enhance the efficiency and instead keeps it constant at $\sim 81\%$. Although Li-TFSI may seem as an active dopant based on conductivity measurements, the doping efficiency determined by EPR is close to two orders of magnitude lower than for FK209. This indicates that the main impact of Li-TFSI on the efficiency of PSC is not due to a doping-induced increase in charge-carrier concentration. We also demonstrated that the spin concentration of Li-TFSI doped spiro-OMeTAD does not significantly increase further in the presence of oxygen and light. Hence, the observed increase in conductivity is not only connected to an increase in charge carriers, but also to an improved charge mobility. Even though FK209 is an efficient dopant for spiro-OMeTAD, $Li^+$ ions might still be required for an efficiently operating PSC, e.g. by interacting with the $TiO_2$ layer.

A detailed spectral analysis of the doped spiro-OMeTAD EPR employing multi-frequency EPR measurements on solution and film samples and DFT calculations was conducted. The origin of the EPR spectrum detected for doped spiro-OMeTAD was clearly identified as the hole on the spiro-OMeTAD molecule and the nature of the EPR-active charge carrier was shown to be independent of the dopant. The differences in the spectral shape between solutions and films were found to be due to a different charge carrier distribution on the molecule in the different environments. From a comparison of the experimental spectra with simulations based on DFT results it was concluded that while in the liquid phase the charge carrier distribution extends over the entire molecule, it becomes localized on a single arm of spiro-OMeTAD in the solid state. The EPR spectra recorded for doped solution-processed films of spiro-OMeTAD reflect the disorder expected based on the preparation method and suggest that EPR could be employed as a tool to investigate the effect of increased crystallinity on the charge carrier distribution and its relation to the hole transport efficiency.

Chapter 6

# Spin-Dependent Processes in Organic Solar Cells

*This chapter presents results obtained from bias-dependent trEPR and trEDMR measurements on bulk-heterojunction solar cells. The detected spin-species and their state after optical excitation was identified with the help of trEPR. This information is correlated to the simultaneously measured EDMR signals, allowing to determine the photocurrent influencing spin-dependent processes.*

## 6.1 Introduction

Organic semiconductors have proven their potential in commercial applications with organic light emitting diodes (OLEDs), encouraging their implementation in photovoltaic devices. The power conversion efficiencies have drastically increased over the last few years and have recently reached values beyond 17% [9, 130–132]. Significant strategies in material design succeeded in boosting efficiencies, e.g. by synthesizing new acceptors [133], optimizing film morphology [134], and enhancing air-stability [135]. In addition, studying fundamental charge transport processes in materials and devices can allow the evaluation of the efficiency limitations, which in turn adds to the knowledge on improving performance.

Transport in organic semiconductors is governed by hopping of charge carriers between localized states. Since organic semiconductors posses weak spin-orbit couplings and dielectric screenings, the spin-relaxation times of the charge carriers are long and lead to a spin dependence in transport and recombination processes which may limit device performance. These processes may thus be studied using spin resonance techniques such as Electron Paramagnetic Resonance (EPR) and Electrically Detected Magnetic Resonance (EDMR) spectroscopy.

Advanced EDMR methods have provided remarkable insight into spin-dependent processes in organic semiconductor devices, with emphasis on charge-carrier recombination [136–140]. However, the involvement of the spin-pairs in the processes and their identification is still debated [141–143]. This is because the different signals

observed in EDMR typically overlap spectrally, making the separation of individual resonance lines challenging. Such processes can either be the recombination of a bipolar pair of a negatively charged polaron ($P^-$) and a positively charged polaron ($P^+$) or the formation of a unipolar pair, where a bipolaron is created from two like-charged polarons. These problems can be overcome by performing low-temperature EDMR experiments and choosing materials in which the spectral signatures associated with $P^+$ and $P^-$ can clearly be separated [139].

It was previously shown that the bias voltage can have a strong impact on the EDMR signals of commercial p-n junctions [144] and organic solar cells (OSC) [145, 146]. This can help to identify possible transport pathways or loss mechanisms under the probed operating conditions. In addition, the influence of the bias voltage on the dynamics of light-induced spin-dependent processes has not been studied yet. However, information on the dynamics of light-induced current-influencing processes can be obtained form transient EDMR (trEDMR) experiments. This was recently shown for polythiophene:fullerene solar cells [147].

Here we present bias-dependent trEDMR measurements on organic bulk-heterojunction solar cells with poly(4, 4-dioctyldithieno(3, 2-b:2′, 3′-d)silole)-2, 6-diyl-alt-(2, 1, 3-benzothiadiazole)-4, 7-diyl (PSBTBT-8) blended with [6,6]-phenyl C61-butyric acid methyl ester (PCBM). We simultaneously perform conventional transient EPR (trEPR) measurements in order to explore the evolution from exciton generation to free charge carriers [83, 84, 148].

Our results show that the resonance signals are spectrally resolved in both EPR and EDMR, allowing the identification of the charge carriers ($P^+$ in PSBTBT-8, $P^-$ in PCBM) involved in spin-dependent processes at low temperature ($T = 80$ K). The spectral signatures of the paramagnetic states contributing to the trEDMR spectrum do not change upon variation of the bias voltage. Yet, the dynamics of the trEDMR signals changes substantially for long delays (several microseconds) after exciton generation. Since the evolution of the $P^+$ and $P^-$ signals is different on this time scale, we conclude that both signals originate from different spin-dependent processes. In contrast, for short delays after optical excitation (below one microsecond), we find similar dynamics for $P^+$ and $P^-$ as well as similar signal intensities, indicating that the trEDMR signal in this time window results from a resonant reduction of the recombination of charge-transfer states, i.e., weakly-coupled polaron pairs localized at the polymer/fullerene interface.

## 6.2 PSBTBT-8:PCBM Bulk Heterojunction

A brief overview of the previously discussed *I-V* characteriscs in BHJ (section 2.2.3) and spin-dependent processes (section 3.2) is given here with reference to the OSC under investigation.

### 6.2.1 *I-V* Characteristics

An organic solar cell can be operated in several regimes defined by the bias voltage (reverse bias, open-circuit conditions, forward bias). The different regimes are shown in Figure 6.1 on the right and marked in the *I-V* curve shown on the left. The curves were measured on a PSBTBT-8:PCBM miniature sized solar cell at room temperature (296 K) inside the resonator at dark conditions (blue) and during illumination (red). In the following the three illustrated biasing conditions and their influence on the spin-dependent transport will be studied. Note that the *I-V* curves show a substantial series resistance. This results from long ITO contact lines necessary for EDMR experiments. This series resistance has no influence on the EDMR signals.

By driving the solar cell in forward bias shown in Figure 6.1a, the HOMO and LUMO levels will align in such a way that electrons and holes are injected from the electrodes allowing them to be transported down (for electrons) and up (for holes) as indicated by the arrows. This leads to an increased recombination rate. The dominant transport mechanism is sequential hopping via localized states. Applying an external bias that compensates the built-in potential will result in a flattening of the energy levels as shown in Figure 6.1b. This is known as the open-circuit condition and in this case is found at $\sim 0.4 - 0.45$ V. At this applied voltage the net current is zero. In the reverse-bias regime, ITO will have a higher potential with respect to Al, as illustrated in Figure 6.1c, causing a tilt of the levels in the opposite direction and hence allowing generated charge carries to be extracted and collected at the respective electrodes.

The EPR and EDMR experiments were performed at 80 K. At this temperature the *I-V* characteristics differs from the behavior at 296 K as shown in Figure 6.2a. The dashed lines indicate the operating conditions of the cell for trEPR and trEDMR measurements. By comparison with the room temperature curve, at 80 K photocurrent generation still takes place, however is reduced. In addition, the curve exhibits an S-like form. S-shaped *I-V* curves can be caused by a strong imbalance of charge-carrier densities at the contacts arising from interfacial effects and can influence the extraction near the device electrodes [149]. In our case, energy barriers at the organic/electrode interface can emerge at low temperatures. Nevertheless, as previous EPR and EDMR studies were performed at low temperatures and, in particular, trEPR measurements on very similar materials cannot easily be carried out at room

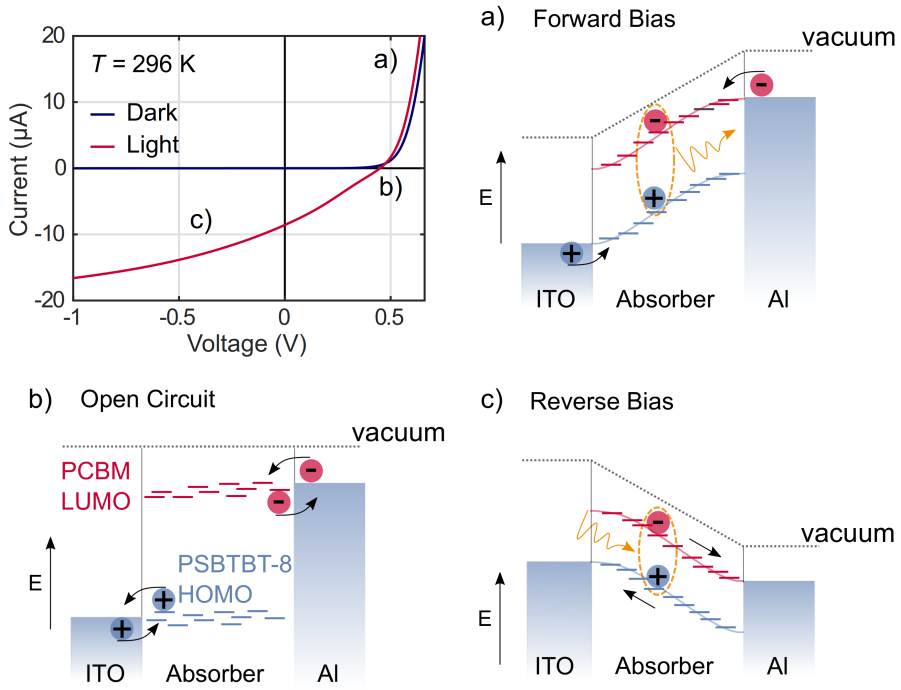


**Figure 6.1:** Left: $I$-$V$ characteristics of a PSBTBT-8:PCBM bulk heterojunction solar cell measured at 296 K inside the resonator under dark conditions (blue) and under illumination (red). The different transport regimes are marked a) for forward bias, b) for open-circuit conditions, and c) for reverse bias. Right: schematic band diagrams for the mentioned operating conditions: a) ($V > V_{oc}$) charge injection from the electrodes into the bulk material, b) the applied voltage compensates the built-in potential and the vacuum levels realign, and c) extraction of photogenerated charge carriers from the bulk material into the electrodes. Note that the LUMO of the donor as well as the HOMO of the acceptor are not shown. Band diagrams adapted from [14].

temperature [84, 147, 150], we chose 80 K for the bias-dependent trEDMR measurements as well.

### 6.2.2 Possible Spin-Dependent Processes

In a donor-acceptor heterojunction solar cell, the absorption of an incident photon leads to the creation of a singlet exciton. This photo-generated exciton diffuses until it reaches a donor/acceptor interface, where a charge transfer (CT) state, i.e., a weakly-bound polaron pair localized at the polymer/fullerene interface is created [18]. The CT state mediates free charge-carrier generation. Ideally this is followed by the electron transport through the acceptor material and the hole through the donor material towards the respective electrodes to contribute to the current. However, the $P^+$ and $P^-$ forming the CT state can also recombine. The recombination probability depends on its spin state and can thus be manipulated using

spin-resonant excitations, giving rise to an EDMR signal. Note that after successful charge separation, non-geminate recombination (at the interface or within a donor or acceptor domain) can occur as a spin-dependent process as well [141, 151]. In addition, hopping transport of polarons via localized states can also lead to EDMR signals if transient doubly occupied conjugated segments of the semiconductor are formed. These doubly occupied states, e.g. bipolarons, are only allowed in a singlet configuration. In consequence, the bipolaron formation rate depends on the spin state of the contributing like-charge polarons [137, 152].

## 6.3 Bias-Dependent trEPR and trEDMR

Figure 6.2b shows the results of a trEPR experiment. The upper panel illustrates the time evolution of the EPR signal after the laser flash. Red colors indicate microwave absorption and blue colors microwave emission as indicated by the arrows. The dashed horizontal lines highlight selected times for which the trEPR signals are shown as a function of the magnetic field in the lower panel. We did not observe an influence of the bias voltage on the trEPR spectrum. In Figures 6.2c-e bias-dependent trEDMR spectra are displayed. In trEDMR measurements, the change in the sample conductivity is detected as a function of the delay after the laser flash (DAF) being current quenching (Q) and current enhancing (En) signals. Note that the absolute sign of the DC current ($I_{DC}$) depends on the applied bias voltage. This is why En signals are positive in Figure 6.2c whereas they are negative in Figures 6.2d and e.

In both trEPR and trEDMR we observe a spectrum comprising at least two components. For long DAF we can clearly identify two separate signals in the trEPR spectrum. Both signals can be reproduced by simulations with the Easyspin toolbox [82] for Matlab assuming literature $g$-matrices. In particular we used $g_x = 2.0027$, $g_y = 2.0020$, $g_z = 2.0009$ for $P^+$ in poly[(4, 4′-bis(2-ethylhexyl)dithieno[3, 2-*b*:2′, 3′-]silole) -2, 6-diyl-*alt*-(4, 7-bis(2-thienyl)-2, 1, 3-benzothiadiazole)-5, 5′-diyl (Si-PCPDTBT) as taken from Ref. [84] for $P^+$ in PSBTBT-8, based on the fact that the chemical structures of both polymers are very similar. $P^-$ in PCBM was simulated using $g_x = 2.0003$, $g_y = 2.0001$, $g_z = 1.9982$ [153]. The antiphase doublet pattern observed in trEPR for short DAF can be attributed to CT states, which can be simulated using the same $g$-matrices as before, in combination with an exchange coupling $J = 1.0\,\mathrm{MHz}$ and a dipolar coupling $D = 8.0\,\mathrm{MHz}$. The simulation, assuming a singlet precursor state, is further described in Ref. [146].

Also the trEDMR spectra can be simulated for all DAF assuming two spectral components with the same line parameters as for trEPR. Only the linewidth was adjusted for each bias condition. From Figures 6.2c-e it is apparent that the trEDMR spectrum changes with time. In addition, the spectral components show zero crossings

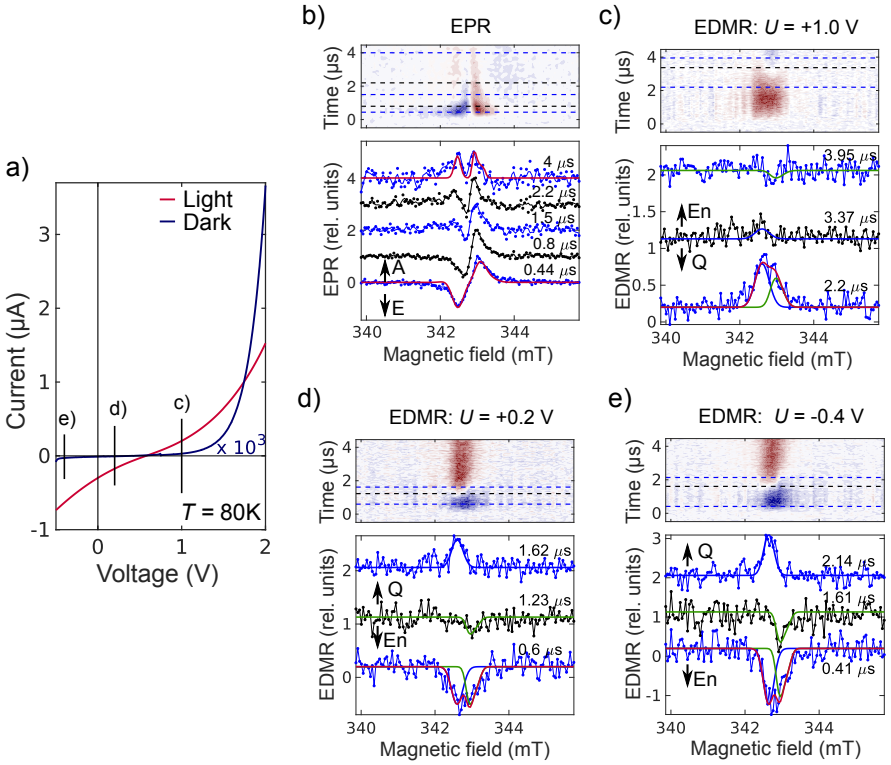


**Figure 6.2:** (a) $I$-$V$ characteristics of a PSBTBT-8:PCBM solar cell measured at 80 K inside an EPR resonator under dark conditions (blue) and under illumination (red). The dark curve is multiplied by a factor $10^3$. The blacked solid lines mark the bias conditions at which trEPR and trEDMR measurements were preformed. (b)-(e) trEPR and trEDMR measurements obtained at 80 K and for different bias voltages. The upper panel is a contour plot displaying the signal in dependence of the magnetic field and its time evolution. The lower panel shows selected time slices. b) trEPR: thin solid lines represent smoothed background-subtracted spectra and the red lines are simulated spectra (see text for details). (c)-(e) trEDMR: the scatter plot (connected by thin lines) gives the background subtracted experimental results. The time slices are shown for times at which one of the two signal contributions is zero. Simulations are given in solid lines (see text for details).

for different DAF. This is illustrated by selecting the time slices such that one of the two signal contributions is zero. In order to study the dynamics of the individual resonant signals for $P^+$ and $P^-$, we show the time evolution of the trEDMR signal for different magnetic-field positions in Figure 6.3. The black solid line represents the off-resonant transient. This is the background current response after the laser flash that is subtracted from all trEDMR signals. The blue and green dashed lines represent the on-resonance transients. The resonance positions are indicated in the inset-plot showing a spectrum taken at $t = 0.41\,\mu$s and a constant applied bias of $-0.4$ V. In the injection regime, the background current is positive at a constant applied bias. This indicates that a positive current response corresponds to an enhancing signal and vice versa. The inverse is true for the extraction regime. The arrows in Figure 6.3 indicate signal enhancing and quenching. We note that the

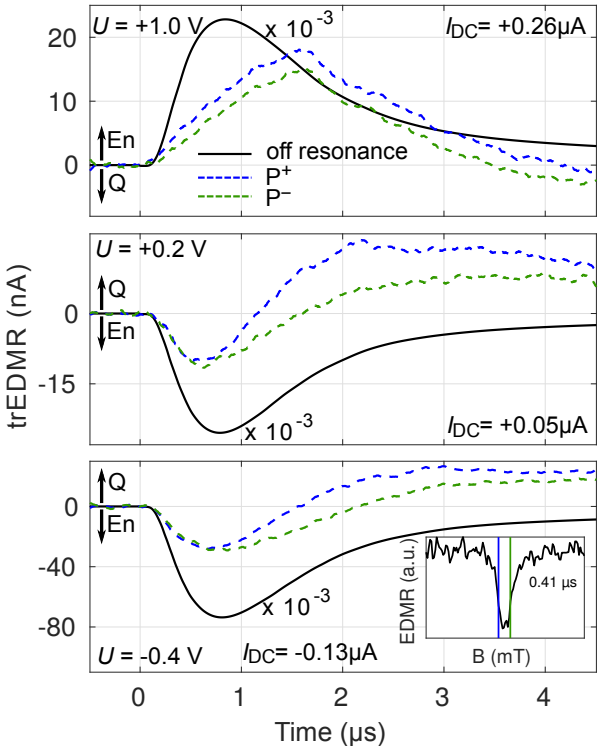


**Figure 6.3:** Current transients for the biasing conditions +1.0 V, +0.2 V, and −0.4 V. Off-resonant transient in black solid line and the background corrected resonant transients in dashed blue and green lines. The background transient is multiplied by a factor $10^{-3}$ for better comparison. The inset plot demonstrates a spectrum recorded at 0.41 $\mu$s DAF and constant bias of −0.4 V. The blue and green solid lines indicate the magnetic field positions for which the transients are displayed.

off-resonant transient does not experience a sign inversion of the current, contrary to the recorded resonant transients. This indicates that the sign change measured in the resonant transients is a genuine effect emerging from the detected signals. They exhibit a transition from a current enhancing to a current quenching process. We further note that the maximum amplitude of the off-resonant transient is much larger than $I_{DC}$ for the given bias voltages. Figure 6.3 also clarifies that the dynamics of the off-resonant and on-resonant transients deviate. This means that the time evolution of the trEDMR signals is not only determined by the $RC$ constant of the device, but also by the dynamics of the spin-dependent processes.

For all probed biasing conditions in trEDMR, one firstly detects current enhancing signals (typically having approximately equal relative intensities), followed by current quenching signals. By comparison of the upper panels in Figure 6.2 it is apparent that current enhancing signal at +1.0 V are longer lived compared to those detected in reverse bias (+0.2 V and −0.4 V). In addition, in Figure 6.3 it is noticeable that for every bias voltage the two EDMR transients change sign at different

DAF and hence have different contributions to the spectrum. This suggests that the nature of the dominant spin-dependent process changes as a function of time.

### 6.3.1 Singular Value Decomposition

Unfortunately, the signal dynamics shown in Figure 6.3 have contributions from both spectral components associated with $P^+$ and $P^-$ due to substantial spectral overlap (see also Figure 6.2). In order to study the temporal evolution of both spectral components individually, we applied a singular-value decomposition (SVD). For a spectrum containing two signals $A(t, B_0)$ and $B(t, B_0)$ that depend both on time $t$ and magnetic field $B_0$, the total spectrum $S_{\mathrm{tot}}$ at each time can be decomposed as follows

$$S_{\mathrm{tot}}(B_0, t) = a(t) \cdot A(B_0) + b(t) \cdot B(B_0) \tag{6.1}$$

where $a(t)$ and $b(t)$ are the SVD-parameters containing the time information and $A(B_0)$ and $B(B_0)$ are spectra of $P^+$ and $P^-$ which were simulated as described above.

From the SVD analysis we obtain the individual intensities of the $P^+$ and $P^-$ EDMR transients. The corresponding time traces are shown in Figure 6.4 for the three bias voltages. To study the influence of the bias voltage on the dynamical behavior we fitted the SVD time traces using the equation

$$f(t) = \left[ a_1 \left( 1 - e^{-\frac{t}{\tau_A}} \right) - a_2 \left( 1 - e^{-\frac{t}{\tau_B}} \right) \right] \cdot e^{-\frac{t}{\tau_C}} \tag{6.2}$$

with the amplitudes $a_1$, $a_2$ and the three time constants $\tau_A$ (describing the rise of the fastest component), $\tau_B$ (describing the rise of the second component) and $\tau_C$ (describing a signal decay). The fit results are shown as red and black solid lines in Figure 6.4. The time constants are given in Table 6.1.

The time traces reflect the rise and decay of the signals after light excitation. From the fits, the three time constants are determined and given in Table 6.1. From the zero intercept the time at which only one component contributes to the spectrum is determined. The obtained SVD-signal at this particular time is shown in the lower panels of Figures 6.2c-e with respect to the experimental spectrum (scatter plot). Here the blue line represents the spectrum of $P^+$ polaron, the green line of the $P^-$ polaron and the red line gives the total spectrum.

## 6.4 Determined Spin-Dependent Processes

The possible spin-dependent processes taking place at the probed biasing regimes and DAF are discussed. The trEPR results are used to identify the polaron state

Table 6.1: Decay-time constants $\tau$ of the trEDMR signal determined from the fit of equation 6.1 for $P^+$ and $P^-$

| | $\tau_C$ [$\mu$s] | $\tau_A$ [$\mu$s] | | $\tau_B$ [$\mu$s] | |
|---|---|---|---|---|---|
| Appl. Bias [V] | | $P^+$ | $P^-$ | $P^+$ | $P^-$ |
| +1.0 | 1.4 | 3.1 | 2.9 | 4.3 | 5.7 |
| +0.2 | 1.2 | 0.7 | 0.6 | 2.1 | 2.9 |
| −0.4 | 1.2 | 1.0 | 1.0 | 2.4 | 3.2 |

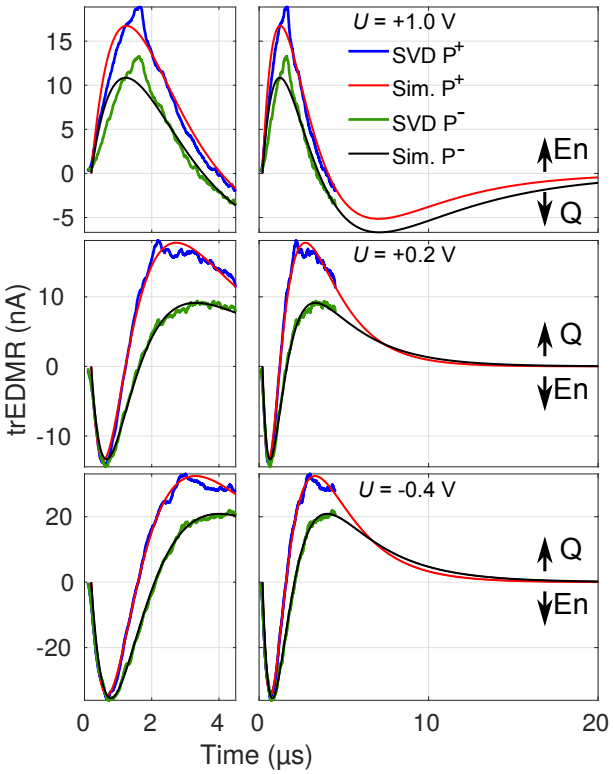


**Figure 6.4:** Time traces for the rise and decay of signals at the applied bias voltages $U = +1.0\,\mathrm{V}$, $U = +0.2\,\mathrm{V}$, and $U = -0.4\,\mathrm{V}$ obtained from the singular value decomposition approach for $P^+$ in blue and $P^-$ in green. The black and red lines indicate exponential fits using equation 6.2.

after excitation. The paramagnetic state is correlated to the spin-dependent process detected in EDMR.

### 6.4.1 Suppression of CT-State Recombination

From the SVD analysis shown in Figure 6.4 we observe for short DAF and at all applied bias voltages, current enhancing signals from both $P^+$ and $P^-$. Within an applied bias voltage, $P^+$ and $P^-$ have a similar fast signal rise time $\tau_A$ in addition to almost similar signal intensities.

The detected EPR spectra between $0.2-0.8\,\mu$s indicate the non-Boltzmann polarized pattern that was attributed to polarons at the CT-state. Thus, the spin-dependent processes detected at early DAF originates from the polarons at the CT-state. Since an enhanced AC current was detected the process at hand aids the dissociation of polarons at the CT-state. The equivalent signal intensities of $P^+$ and $P^-$ imply the involvement of equally large contributions of both polarons.

From the results in EPR and EDMR for early DAF the following dynamic is deduced: after the photogeneration of an exciton, diffusion towards the donor/acceptor interface takes place and the exciton is transferred to the CT-state, where the $P^-$ polaron is in the PCBM and $P^+$ in the PSBTBT-8 matrix near the interface and weakly coupled. The polarons are initially in a singlet configuration and the probability of recombination is higher. Spin manipulation can lead to a larger triplet ensemble from which recombination is forbidden and dissociation is more likely. Finally the number of $P^+$ and $P^-$ polarons that reach the electrodes is similar resulting in similar signal rise times and almost similar signal intensities. We attribute this spin-dependent processes to the suppression of recombination at the CT-state.

### 6.4.2 Bias-Dependent Hopping Transport

The rise time of the second component $\tau_B$ is longer compared to $\tau_A$ and takes over at longer DAF. The constant $\tau_B$ is different for the $P^+$ and $P^-$ polarons and also varies between the different biasing regimes probed.

In principle the following spin-dependent processes can occur: (i) spin-dependent recombination of $P^+$ residing on the polymer and $P^-$ residing on the fullerene, (ii) recombination of both $P^+$ and $P^-$ in the fullerene, (iii) recombination of $P^+$ and $P^-$ in the polymer, and (iv) hopping transport of $P^+$ in the polymer and $P^-$ in the fullerene via localized states.

Recombination of the $P^+$ in the polymer and $P^-$ in the fullerene at the CT-state would yield a signal decay for $P^+$ and $P^-$ on a similar time scale. Since $\tau_B$ is clearly different for the two polarons, this recombination process can to a great extent be excluded. The described recombination processes (ii) and (iii) generally can occur during transport and cannot be ruled out. Typically, the variation in signal decay times of polarons implies a difference in their transport dynamics.

With the trEPR spectra for long DAF indicating two separate signals, it is clear that $P^+$ and $P^-$ are in different environments. Thus the polarons undergo spin-dependent processes that are independent of each other and therefore have different signal rise times $\tau_B$. The process is likely related to spin-dependent hopping. The polarons have different mobilities due to their environment: the $P^+$ hopping transport takes place in the polymer and is faster than the $P^-$ transport, which takes place

in the fullerene. Furthermore, we observe that the biasing condition can influence the time constant $\tau_B$ of the hopping transport. Extraction bias voltages indicate a shorter $\tau_B$ and hence a faster spin-dependent process compared to the probed injection bias voltage. This is also reflected in the contour plot in Figure 6.2c-d where in the injection regime the transition from current enhancing to current quenching signals takes longer than in the extraction regime.

### 6.4.3 Single Polaron Contribution

The zero crossing of one polaron results in its EDMR signature to not contribute to the spectrum, while the other is detectable and hence its spin can still be manipulated with microwaves. The detection of one polaron at a time is further evidence for its participation in a spin-dependent photocurrent influencing process that is different from the process of the resonantly-absent polaron. Depending on the applied bias voltage the polaron can be engaged in a photocurrent enhancing or quenching mechanism: in injection $P^+$ contributes to current enhancement during the zero intercept of $P^-$, while $P^-$ participates in current quenching at the $P^+$ zero crossing. The inverse is true for the extraction bias voltages.

## 6.5 Conclusion

Simultaneous detection of trEPR and trEDMR showed spectrally resolved resonance signals which allowed the identification of the $P^+$ and $P^-$ polarons in the PSBTBT-8 and PCBM respectively and their spin-dependent processes. EDMR results revealed for short delays after optical excitation similar dynamics as well as similar signal intensities for $P^+$ and $P^-$. The spin-dependent process the polarons are involved in was attributed to the reduction of spin-dependent recombination at the CT-state. For longer delays after exciton generation the $P^+$ and $P^-$ signals were found to evolve with different time scales, evidence for their involvement in different spin-dependent processes.

The present work demonstrates the convenience of simultaneous trEPR and trEDMR detection for the identification of light-induced paramagnetic species and their involvement in photocurrent influencing processes. This strategy can be important for future studies on related material systems, such as non-fullerene acceptors-polymer and perovskite solar cells, to shed light on the transport processes and loss mechanisms affecting photovoltaic energy conversion.

Chapter 7

# Spin Physics in Perovskites

*This chapter presents first results obtained from EPR and EDMR experiments on perovskite materials and solar cells. In the first part, Sn-Pb perovskite solar cells are studied using EDMR. The question whether spin-dependent processes in perovskite solar cells play a role is addressed and discussed. In the second part, the evidence of triplet-excitons in 2D perovskites is investigated. Lastly, an overall outlook on the prospects of EPR spectroscopy to study perovskite materials and devices is outlined.*

## 7.1 Introduction

From the doping studies on organic semiconductors, the work on organic solar cells presented in this thesis, as well as numerous EPR studies conducted on organic semiconductors, it is clear that the spin degree of freedom plays a tremendous role in the detection and determination of charge carrier dynamics. Organic semiconductors are an optimum medium for spins to perpetuate, as they consist of light atoms with weak spin-orbit couplings that prolong spin relaxation times. Such dynamics are already present at room temperature. For systems with strong SOCs, such as perovskites, the $g$-value will depart markedly from the value of the free electron and is expected to have a large $g$-anisotropy [128]. The reported absolute $g$-values[1] for photogenerated electrons and holes in a (standard) $CH_3NH_3PbCl_xI_{3x}$ perovskite film are 2.63 and 0.33 respectively [154], resulting in a large difference between the electron and hole $g$-values, giving rise to a large $\Delta g \sim 2.3$. Earlier reports measured a $\delta g \sim 0.65$ in $CH_3NH_3$ $PbI_{3-x}Cl_x$ [81]. Based on the $\Delta g$-mechanism described in section 3.1.7, a large $\Delta g$ causes large singlet-triplet interconversion rates. If this rate becomes larger than the spin-lattice relaxation time, alterations in the spin populations of the sublevels via the application of an external magnetic field can be induced. The changes in the populations of the spin sublevels will affect the recombination and dissociation probabilities of spin-pairs, measured as changes in the photocurrent and photoluminescence [81, 155, 156].

[1] The $g$-values were determined from transient Faraday rotation experiments. The linear relation between the oscillation frequency and magnetic field yields the $g$-value as the slope.

Based on the reported spin-dynamics studied by magneto-optical experiments, efforts to explore state-of-the-art perovskite materials and solar cells with EPR and EDMR spectroscopy were made. The absence of resonance signals in most experiments is not fully understood, but believed to be caused by the strong SOC. Nonetheless, experimental strategies can be applied to gain insight into spin-dependent processes and will be demonstrated in the chapter.

## 7.2 Tin-Based Perovskite Solar Cells

Zhang et al. [156] reported on an increasing spin dependence of the measured photocurrent, as a result of reduced Pb content in the perovskite layer of solar cells. The result was attributed to the weakening of the SOC as a consequence of the reduction of the heavy element Pb and its substitution by the lighter element Sn. In this section we intend to explore spin-dependent processes using EDMR techniques in Sn-Pb perovskite solar cells. The objective is to identify the paramagnetic centers that influence the photocurrent. The possible spin-dependent processes the centers are involved in at different solar cell working conditions are discussed.

### 7.2.1 *I-V* Characteristics

Table 7.1: Sn-Pb PSC parameters obtained from the *J-V* shown in Figure 7.1a and measured in forward direction (blue). Illumination with a light intensity of $100\,\mathrm{mW/cm^2}$.

| $V_{OC}$ [V] | $J_{SC}$ [$\mathrm{mA\,cm^{-2}}$] | $V_{MPP}$ [V] | $J_{MPP}$ [$\mathrm{mA\,cm^{-2}}$] | $FF$ | $PCE$ [%] |
|---|---|---|---|---|---|
| 0.67 | -28.5 | 0.50 | -25.7 | 0.67 | 12.8 |

The solar cells were fabricated as described in section 4.1.4. A schematic illustration of the layers is shown in Figure 7.1a. The *I-V* characteristics in Figure 7.1a were measured on a standard $2.5 \times 2.5\,\mathrm{cm^2}$ geometry directly after preparation inside a glovebox in the laboratories of the group of Prof. Dr. Neher in Potsdam (as described in section 4.1.5). The voltage was once scanned in forward and in reverse direction, as indicated by the arrows, to examine the cell's response to transient changes affected by the scan direction, which are minimal for this cell. The *J-V* parameters were obtained from the forward bias scan and given in Table 7.1. The PCE of 12.8% is calculated according to equation 2.4, where the input power was $P_0 = 100\,\mathrm{mW/cm^2}$. A PCE of almost 13% is adequate as reported efficiencies range between 6.7% [156] to 17.6% [157] depending on the Sn-to-Pb ratios and cell architecture used. The $V_{OC}$ is however relatively low. It was observed that the $V_{OC}$ loss increases with the Sn content [158]. This is mainly contributed by defects created by oxidation of $Sn^{2+}$ to $Sn^{4+}$. The $V_{OC}$ can be as high as 0.77 V [157].

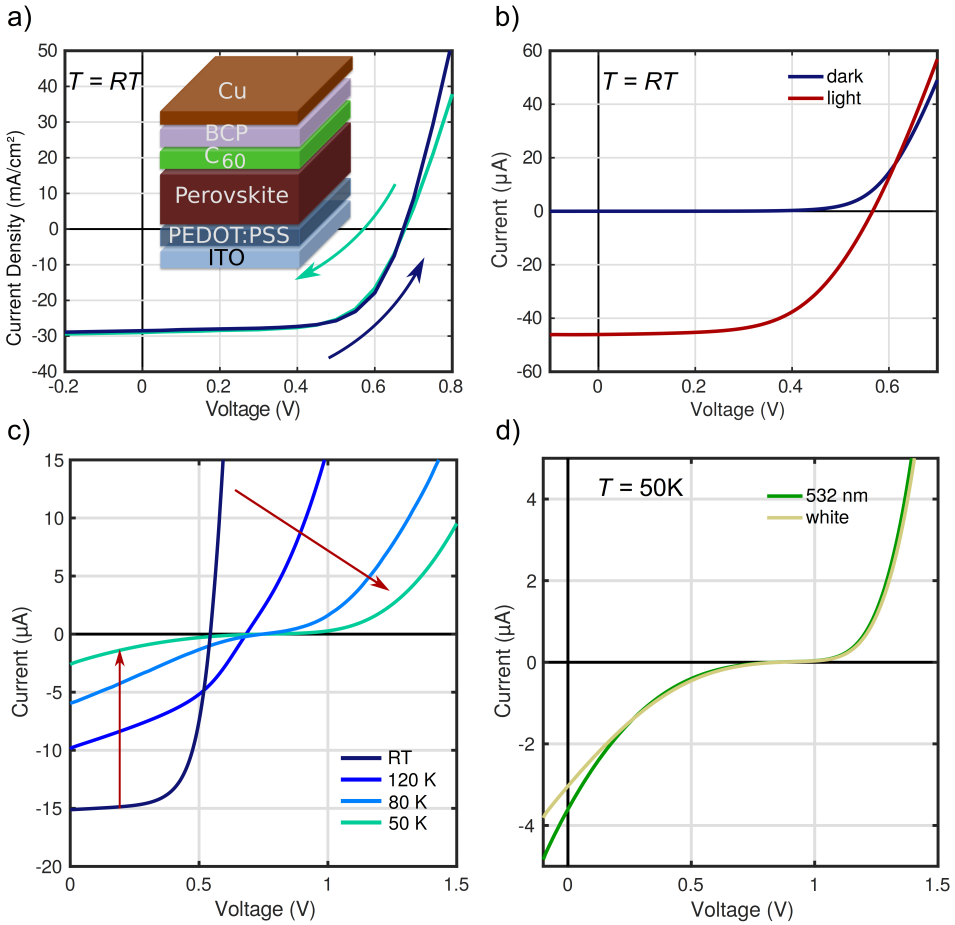


**Figure 7.1:** *I-V* characteristics of Sn-Pb PSC: a) current density versus applied voltage in forward and reverse direction measured on a $2.5 \cdot 2.5\,\mathrm{cm}^2$ substrate inside a glove box. The obtained *J-V* parameters are given in Table 7.1, b) *I-V* curve measured on a EDMR substrate inside the glove box. c)-d) *I-V* curves measured for an encapsulated cell inside the resonator: c) temperature dependent, with the red arrows emphasizing the effect on the curves with decreasing temperatures (decreasing $I_{SC}$ and increasing $R_S$) and d) at 50 K and illumination-wavelength dependent.

Figure 7.1b shows the *I-V* characteristics of a solar cell prepared on the EDMR-substrate geometry measured at room temperature at the probe-station setup inside the glovebox in the labs of the Freie Universität Berlin.

Temperature dependent *I-V* curves were measured inside the resonator for room temperature (RT $\approx$ 296 K), 120 K, 80 K, and 50 K and shown in Figures 7.1c. There are noticeable changes that take place when going to lower temperatures. Firstly, the short circuit current $I_{SC}$ is reduced. Secondly, an increase in the series resistance $R_S$ is observed. Furthermore, the *I-V* curves deform and develop an S-shape with decreasing temperatures, forming a plateau around $V_{OC}$. The latter effect is a consequence of energetic barriers [26, 159] that can form at the organic/electrode junctions and/or at the perovskite/organic heterojunction.

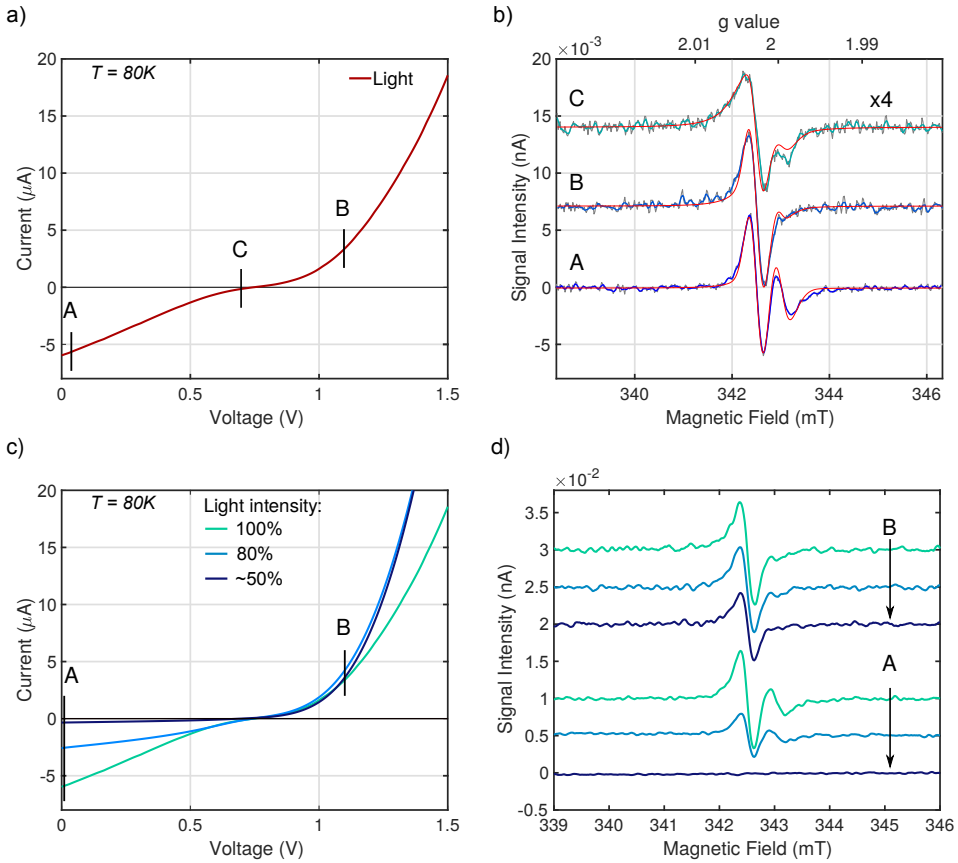


**Figure 7.2:** Bias-dependent cwEDMR measurement at low temperatures: a) and c) *I*-*V* curves of the Sn-Pb PSC at 80 K measured under illumination a) at 100% and c) at varying light intensities. The black markers label A,B, and C indicate the biasing condition at which cwEDMR spectra were recorded shown in b) and d). The spectra in b) are recorded at a modulation frequency of 4 kHz, 0.12 mT modulation amplitude and 20 dB microwave attenuation. The top axis indicates the *g*-value axis. Spectrum C is multiplied by a factor 4 to ease comparison with other spectra. The spectra in d) are recorded at a modulation frequency of 10 kHz, modulation amplitude of 0.12 mT, and microwave powers of 17 dB.

### 7.2.2 Bias Dependent cwEDMR

An attempt to detect EDMR spectra at room temperature and different biasing conditions was made. This however, remained unsuccessful. The first EDMR spectra were detected at 80 K. Therefore all EDMR experiments were conducted at lower temperatures.

The *I*-*V* curve under maximum white light illumination and at 80 K is shown in Figure 7.2a. The black vertical lines labeled A, B, and C mark the positions on the curve where cwEDMR spectra were measured (under the same illumination condition) and shown in Figure 7.2b. Measurements under reduced light intensities were conducted to verify whether the detected cwEDMR signals are light-induced

Table 7.2: Simulation parameters for the spectra in Figure 7.2b. $\Delta B$ is the linewidth of Gaussian shape (if not otherwise indicated) and $w$ is the weighting factor. The $P^-$ signal was additionally simulated with a $g$-strain (0.0001 0.0001 0.0020).
[a]This line width is of Lorentzian shape.

| | | $V_{OC}$ | $U > V_{OC}$ | $U \approx 0$ |
|---|---|---|---|---|
| PEDOT | $g = 2.0029$ | $\Delta B^a$ : 0.8 mT<br>$w$ : 2.31 | $\Delta B^a$ : 0.8 mT<br>$w$ : 2.0 | $\Delta B^a$ : 0.8 mT<br>$w$ : 1.0 |
| $P^-$ in $C_{60}$ | $g_x = 2.0003$<br>$g_y = 1.9996$<br>$g_z = 1.9982$ | $\Delta B$ : 0.3 mT<br>$w$ : 0.09 | $\Delta B$ : 0.2 mT<br>$w$ : 0.11 | $\Delta B$ : 0.3 mT<br>$w$ : 0.71 |
| CR | $g = 2.0026$ | $\Delta B$ : 0.30 mT<br>$w$ : 0.10 | $\Delta B$ : 0.35 mT<br>$w$ : 1.0 | $\Delta B$ : 0.35 mT<br>$w$ : 1.0 |

and coming from the sample. Figure 7.2c shows the $I$-$V$ curves measured at 100%, 80%, and $\sim$ 50% light intensities with cwEDMR spectra measured at the positions marked by A and B in the $I$-$V$ curves and displayed in Figure 7.2d. The color of the spectra indicate the respective $I$-$V$ curve and illumination intensity given in Figure 7.2c.

Decreasing the light intensity results in the decrease of the DC current measured at short circuit conditions from $-0.57\,\mu$A under maximum illumination to $-0.30\,\mu$A at 80% and $-0.03\,\mu$A at $\sim$ 50% illumination intensity. In Figure 7.2d spectra A measured at $U \approx 0$ indicate a decrease in signal intensity with a 20% decrease in light-source intensity and no spectrum with further decrease to 50%, which implies that the signals detected are light-induced. Spectra B measured at $U = +1.1$ V show that the signal intensity and the DC current seem to be insensitive to variations in the light intensity.

Simulations of the spectra under maximum light intensity and different biasing conditions are shown in red in Figure 7.2b with their parameters given in Table 7.2. The spectra were simulated with three spin-1/2 systems using the solid-state cwEPR simulation routine of the Matlab toolbox EasySpin [82]. The linewidths ($\Delta B$) are fitted to match the experimental data and the weighting factors ($w$) are fitted to match the signal intensity regarding the complete spectrum. The high-field signal was simulated with the $g$-matrix given in Table 7.2 and a $g$-strain, which describes the random distribution of $g$-values around the mean. The PEDOT signal was determined from X-band cwEPR measurements (see Appendix D) and only appears as a low field shoulder in the spectra. The sharp feature at the center of the spectrum is simulated with $g = 2.0026$ and is referred to as the central-resonance (CR) signature. Its origin is not precisely known and will be discussed later.

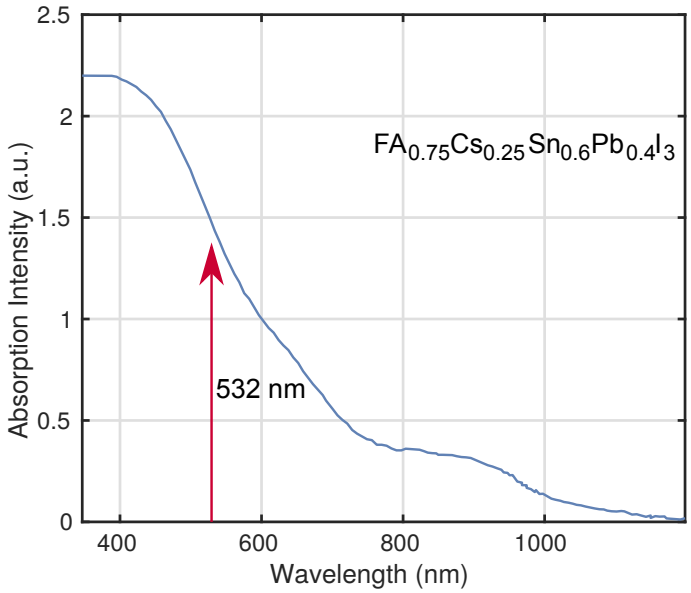


**Figure 7.3:** Absorption spectrum of $FA_{0.75}Cs_{0.25}Sn_{0.6}Pb_{0.4}I_3$ perovskite with the red arrow marking the absorption at 532 nm. Measurement performed in the labs of Prof. Dr. Dieter Neher in Potsdam.

Depending on the applied bias, the cwEDMR signals and their intensity differs. Particularly at $V_{OC}$ (spectrum B), even though the signal intensity is four times lower compared to the other biasing conditions, three spectral features can be distinguished: PEDOT, $P^-$ in $C_{60}$, and the CR-line. The spectrum at $V_{OC}$ is broader compared to spectra measured at other bias voltages. The broadening is attributed to the PEDOT contribution that becomes significant with a linewidth of $\Delta B = 0.8\,\mathrm{mT}$ and a weighting factor of $w \approx 2.3$. In the EDMR spectrum at $U \approx 0$ (A), a significant contribution of $C_{60}$ is detected, compared to $V_{OC}$ and forward bias $U > V_{OC}$ (spectra C and B respectively). At forward bias, mainly the CR feature is detected.

The individual signals were identified by determining their $g$-values from which the type of paramagnetic species and its environment can be deduced. The study showed that the charge carriers originate from the solar cell. To examine whether the signals are actually created in the perovskite layer rather than the applied transport layers, different excitation wavelengths can be used to selectively and exclusively excite a specific layer.

### 7.2.3 Optical Excitation at 532 nm

State-of-the-art perovskite material MAPI (without Sn) has an absorption edge around 800 nm. By including Sn, the optical absorbance moves towards the infrared region and is further red-shifted with increasing Sn-content [160]. PEDOT:PSS contains absorption peaks at 193 and 225 nm attributed to $\pi$ and $\pi^*$ transitions [161],

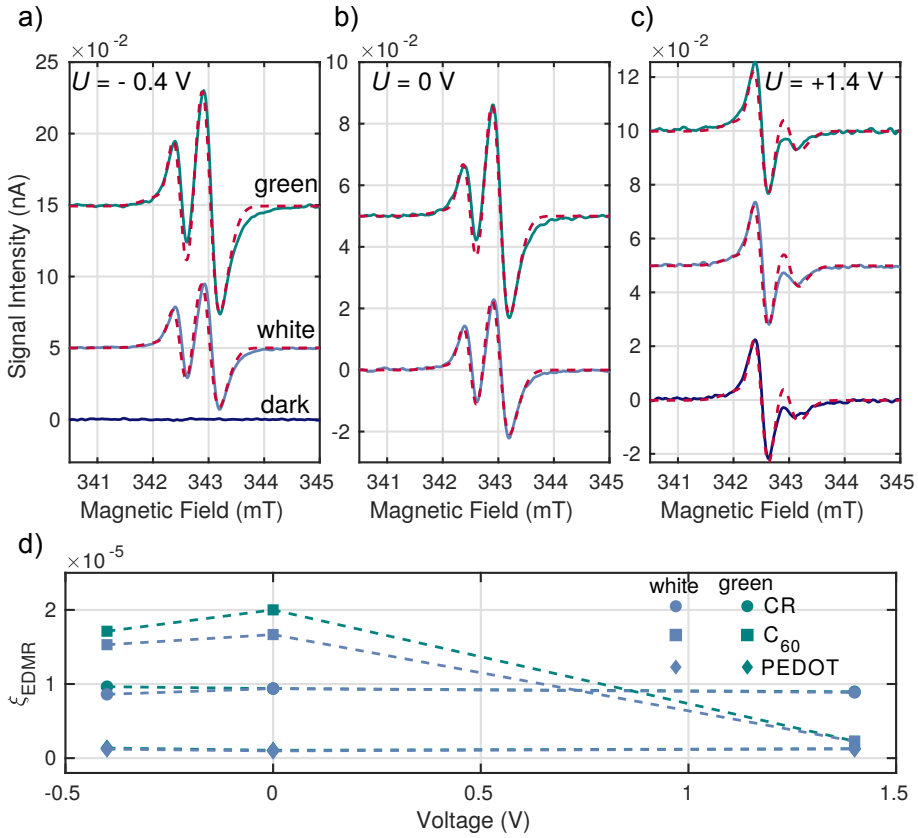


**Figure 7.4:** a-c) Bias-dependent cwEDMR spectra measured at 50 K with 10 kHz modulation frequency, 0.12 mT modulation amplitude under green and white light illumination and dark conditions. Red-dashed lines indicate the simulation. d) $\xi_{EDMR}$ vs. applied voltage.

and no absorption maxima between 400 and 800 nm. $C_{60}$ contains intense peaks in the UV region and a weak visible absorption band in the range of $400 - 600$ nm [162]. Therefore, illumination of the Sn-Pb solar cell at wavelengths between 400 and 600 nm would ideally result only in the optical excitation of the perovskite layer. For this purpose, an excitation wavelength of 532 nm was used to study the EDMR response of the Sn-Pb solar cell and compared to cold white light illumination.

The EDMR signals measured under dark and illumination with a continuous wave diode laser at 532 nm (green) and the halogen cold white light source under different biasing conditions are examined. Low temperatures of 50 K were selected due to the improved SNR of the signals. The *I-V* curves are shown in Figure 7.1d. The cwEDMR spectra are shown in Figure 7.4.

The spectra are simulated with the parameters given in Table 7.2. Only the amplitude (given by the weighting factor $w$) was adjusted to the signal intensity. The peak-to-peak signal intensity of each spectral feature $\Delta I_{\mathrm{EDMR}}$ gives the absolute spin-dependent EDMR current. An approximation of the number of green photons reaching the sample is obtained from the photon flux determined in equation 4.5

Table 7.3: The influence of the detected species on the photocurrent on resonance given by $\xi_{EDMR}$.

| | $\lambda$ | $\xi_{EDMR}\ U<0$ $\times10^{-5}$ | $\xi_{EDMR}\ V\approx0$ $\times10^{-5}$ | $\xi_{EDMR}\ U>V_{OC}$ $\times10^{-5}$ |
|---|---|---|---|---|
| CR | 532 | 0.96 | 0.94 | 0.90 |
| | white | 0.86 | 0.94 | 0.87 |
| $C_{60}$ | 532 | 1.7 | 2.0 | 0.23 |
| | white | 1.5 | 1.7 | 0.23 |
| PEDOT | 532 | 0.14 | 0.11 | 0.13 |
| | white | 0.12 | 0.10 | 0.13 |

multiplied by the photoactive area defined by the electrode ($\sim 2.25 \cdot 10^{-2}\,\mathrm{cm}^2$). This results in $\sim 3.8 \cdot 10^{25}$ photons per second reaching the solar cell. From the DC current at $I_{\mathrm{SC}} = -3.5\,\mu\mathrm{A}$, approximately $2.2 \cdot 10^{13}$ electron-hole pairs are generated and give rise to the measured DC photocurrent. The evaluation of $\Delta I_{\mathrm{EDMR}}$ at short circuit gives a rough estimate of $6 \cdot 10^5$ polarons and/or spin species involved in a spin-dependent process, which is almost 1 in $10^6$. The contribution of each individual spin species to the change in DC current $I_{\mathrm{DC}}$ yields the EDMR effect $\xi_{\mathrm{EDMR}}$

$$\xi_{\mathrm{EDMR}} = \left| \frac{\Delta I_{\mathrm{EDMR}}}{I_{\mathrm{DC}}} \right| \tag{7.1}$$

given in Table 7.3 for each detected signal in the spectra at different applied bias voltages and under green and white illumination. The graph in Figure 7.4b displays the results of Table 7.3.

### 7.2.4 Discussion

The S-shape of the *I-V* curve is a result of energetic barriers at the perovskite/organic and/or organic/electrode interface. In principle, both barriers can emerge at room temperature and give rise to the S-shape. In the solar cell under investigation, the current can flow barrier free at room temperature, thus excluding transport limitations at interfaces. Since the perovskite/organic interfaces are energetically matched, this type of barrier will not play a role, even at lower temperatures. The decrease of $I_{\mathrm{SC}}$ with decreasing temperature is an indication for transport limitations to the electrodes and eventually the extraction at the electrodes. Hence, the S-shape most probably originates from energetic barriers emerging at the organic/electrode interfaces. The first EDMR spectra were detected at 80 K and may be partially connected to the deformation observed in the *I-V* curve when lowering the temperature. Since transport in disordered systems requires thermal

activation, the decrease in temperature reduces the hopping probability. In effect spin-dependent transport becomes relevant, as hopping can be enhanced by spin resonance.

The EDMR study conducted on a Sn-Pb PSC demonstrated that photo-induced paramagnetic species created in the perovskite layer can be detected with EDMR. The detected spin species taking part in alterations of the spin-dependent photocurrent were distinguished based on their $g$-values ($g$-matrix).

The high-field signal was attributed to the $P^-$ polaron in $C_{60}$. The determined principle values of the $g$-matrix given in Table 7.2 are closer to the values reported for the PCBM anion in Ref. [153] than the $C_{60}$ values experimentally determined from a blend of poly(3-hexylthiophen-2,5-diyl) (P3HT):$C_{60}$ frozen solution in Ref. [163]. It was shown that $g_y$ and $g_z$ markedly depend on the sample treatment [163], which explains the deviations from the reported values and inconsistencies in literature regarding the magnetic resonance parameters. The low-field peak of the $C_{60}$ anion ($g_x$) on the other hand always stays narrow and does not shift. Its value is more consistent with reported values in literature. The $g$-anisotropy is to some extent due to the Jahn-Teller effect [164, 165], which is a result of a distortion in the symmetry of the $C_{60}$ molecule once it accepts an electron. However, latest results have shown that the anisotropy is largely due to the microscopic environment of the $C_{60}$, which can deform and distort the molecule [163]. In addition a $g$-strain is assumed which describes the random distribution of $g$-values around the mean. It accounts for the broadening effect that arises from a distribution of slightly different structures induced by microscopically different sites [164].

A low-field shoulder that was relatively insensitive to the experimental conditions was attributed to a paramagnetic state in PEDOT. Its $g$-value was determined from X-band cwEPR measurement on a PEDOT:PSS film (see Appendix D). A third pronounced resonance line indicated as the CR-line was determined with $g = 2.0026$ close to values reported for a narrow feature detected in PEDOT cwEPR spectra [166] and for thiophene radical cations [161, 167, 168]. It is therefore likely that this feature is the $P^+$ polaron in the PEDOT layer. The signal was overall sensitive to the illumination intensity at short circuit and extraction bias voltages, where the resonance line is accompanied by the $P^-$ signal. This provides further evidence for its attribution to the $P^+$ polaron.

The difference in the spin-dependent contribution $\xi_{\mathrm{EDMR}}$ between $P^+$ and $P^-$ implies that they are involved in different spin-dependent processes. This is extremely probable as the perovskite separates the $C_{60}$ and PEDOT layers. Unless the polarons are coupled over the entire thickness of the perovskite layer, spin-dependent recombination by the $P^+$ and $P^-$ can to a large extent be excluded. The current influencing spin-dependent process that $P^+$ contributes to may be related to the transport in the PEDOT layer and the same applies for the $P^-$ in $C_{60}$.

At extraction and open circuit under illumination, both $P^+$ and $P^-$ contribute to the spectrum. The $P^-$ contribution is slightly larger. Since at extraction under dark conditions, no EDMR signals were detected (Figure 7.4a), it is likely that under illumination these are the photogenerated charge carriers from the perovskite layer that are transferred to the organic layer where they undergo spin-dependent processes.

In the injection regime, the $P^+$ is the only signal with a significant contribution to the spectrum, which further suggests its sole involvement in a process different than that from $P^-$. The signal appears independent of solar cell illumination, indicating that the polarons taking part in the spin-dependent process are not necessarily light induced and may stem from the injection of charge carriers at the electrodes. The $P^-$ in $C_{60}$ has a significantly smaller and almost disappearing spin-dependent contribution compared to the contribution detected at extraction voltages. The other PEDOT contribution at $g = 2.0029(4)$ is relatively small. The feature determined from cwEPR seems to only play a marginal role in the transport dynamics compared to the other detected signatures.

Moreover, the bias-dependent study shows that $\xi_{\mathrm{EDMR}}$ of $P^-$ is affected by variations in the applied bias, whereas the $P^+$ contribution remains unchanged. It implies that the spin-dependent process of $P^-$ in $C_{60}$ can be tuned, such that it is increased, reduced, or activated with the application of an external bias voltage. The type of process may differ depending on the applied bias.

The advantage of cwEDMR is the high sensitivity of signal detection aided by the lock-in amplifier which at the same time imposes a drawback: due to phase sensitive detection the sign of the resonance signal cannot give conclusive information on the type of spin-dependent process at hand. We determined that $P^-$ and $P^+$ are likely engaged in spin-dependent processes that take place in $C_{60}$ and PEDOT, respectively, and thus are independent of each other. However, whether they are spin-dependent hopping or recombination processes leading to current enhancing or current quenching is difficult to determine from cwEDMR measurements alone. For this purpose, pulsed EDMR techniques allow a direct identification of the photocurrent influencing dynamics and will be discussed in the following section.

### 7.2.5 Pulse EDMR

Pulse EDMR experiments allow the electrical detection of the change in sample conductivity resulting from changes in spin-dependent recombination and hopping rates as a function of time after spin manipulation. The results discussed in the following lay the groundwork for future experiments.

The current response was detected after a pulse of $t_p = 70\,\text{ns}$ length (exciting at a bandwidth of $\Delta\nu = 1/t_p = 14\,\text{MHz}$ ) with microwave power attenuation of 20 dB. The pEDMR spectrum measured at 20 K under white light illumination and applied bias $U = +2.0\,\text{V}$ is shown in Figure 7.5a. The lower plot shows the EDMR spectrum for 2.6 $\mu$s and 4.4 $\mu$s after the microwave pulse. Two signals can be distinguished with approximately the same signal amplitude. From the transient current response, it was determined that these signals contribute to a current quenching spin-dependent process.

The high-field signal simulated with $g$-matrix = (2.0003 2.001 1.9982) and $\Delta B = 0.3\,\text{mT}$ is attributed to $P^-$ in $C_{60}$ (green line). The low-field signal is simulated with a $g$-value of 2.0018 and $\Delta B = 0.3\,\text{mT}$ (yellow line). This feature was also observed in previous pulsed EDMR experiments conducted on $C_{60}$-containing devices at room temperature by Harneit et al. [141]. The reported $g$-value of $g = 2.0018(5)$ and narrow linewidth of $\Delta B \leq 0.3\,\text{mT}$ is in accordance with the signal found in the presented measurement. We concluded that this signal also originates from a paramagnetic species in the $C_{60}$ layer of the solar cell. The type of paramagnetic species, e.g. cation, defect state, etc., and its sensitivity to the experimental conditions such as temperature and externally applied voltage still need to be determined.

To allow the comparison between the signals identified in cwEDMR and pEDMR, Figure 7.5b shows the cwEDMR spectrum in the top plot and the pEDMR at 4.4 $\mu$s after the microwave pulse in the bottom plot, both measured at forward bias. The horizontal lines mark the $g$-values (and $g$-matrix for $P^-$) determined from both experiments. The $g_y$ value of the $P^-$ determined from pEDMR differs from the one determined in cwEDMR. It was previously mentioned that this may be a result of sample treatment and the experimental conditions at which measurements are conducted [163]. It is important to note that literature $g$-values obtained from EPR experiments can deviate from EDMR measurements, since the detected observable differs between the two measurements (microwave detection for EPR and current detection for EDMR). It is possible that in EDMR an isotropic line at a certain principle value of the $g$-matrix is detected [147]. This suggests that the EDMR spectral intensity is mainly due to polarons ($P^-$) in the molecule ($C_{60}$) with a preferential orientation with respect to the direction of the external magnetic field.

To identify the type of spin-dependent process the detected species are involved in at $U = +2.0\,\text{V}$, a Rabi-oscillation experiment at different magnetic field positions was performed. If a spin pair is simultaneously driven by magnetic resonance, the doubling of the fundamental Rabi oscillation $\Omega = 2\gamma B_1$ is detected, where $\gamma$ is the gyromagnetic factor and $B_1$ is the magnetic field induced by the microwave radiation. For spectral features separated on the magnetic field axis, the distinction between spin-dependent hopping and recombination can be made on the basis of the field position of the spin-locking signal [139]. Under application of high $B_1$ and assuming two well separated signals attributed to $P^+$ and $P^-$ polarons, in the case

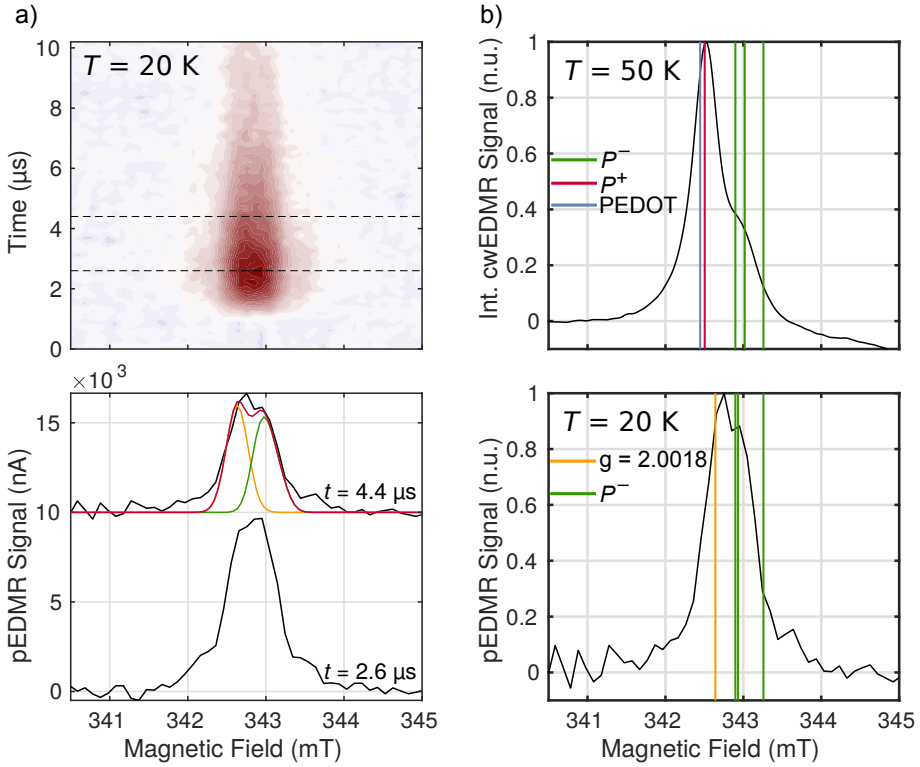


**Figure 7.5:** a) Pulse EDMR results from Sn-Pb PSC measured at $T = 20\,\mathrm{K}$, under while light illumination and $U = +2.0\,\mathrm{V}$ applied bias voltage. The lower plot indicates the spectra at selected times after the mw pulse. Simulation of the spectrum at $t = 4.4\mu\mathrm{s}$ in red consisting of a the simulation of $P^-$ (green) and the signal at $g = 2.0018$ in yellow. b) Comparison between integrated cwEDMR ($T = 50\,\mathrm{K}$) and pEDMR spectra $T = 20\,\mathrm{K}$. Horizontal lines mark the experimentally determined $g$-values.

of hopping two spin-locking signals will appear at the same spectral position as that of the detected $P^+$ and $P^-$. Since coherent oscillation between $P^+$ and $P^-$ cannot be driven at high $B_1$, the pair is not coupled and the spin-locking signals detected stem from independently oscillating $P^+$ and $P^-$ polarons. In the case of spin-dependent recombination of the $P^+$ and $P^-$, the polarons will be (weakly) coupled and coherent driving of spin nutations results in a spin locking signal between the resonance positions of the two detected features.

The analysis of the Rabi experiment was done in Matlab. The time traces were apodized by a Hamming window to suppress high side-bands appearing after the fast-Fourier transformation. The results are shown in Figure 7.6, where the spin-locking signal is detected already at weak $B_1 = 0.52\,\mathrm{mT}$. The lower plot shows the fast-Fourier spectrum with respect to the oscillation frequency at the field position marked by the dashed line in the upper plot. Two components at $\Omega_1 = 14.4\,\mathrm{MHz}$ and $\Omega = 2\Omega_1 = 28.8\,\mathrm{MHz}$ are determined. The spin-locking signal appears between the resonances of the two spin species, thus indicating that the $P^-$ and the species at $g = 2.0018$ are weakly-coupled and involved in spin-dependent recombination.

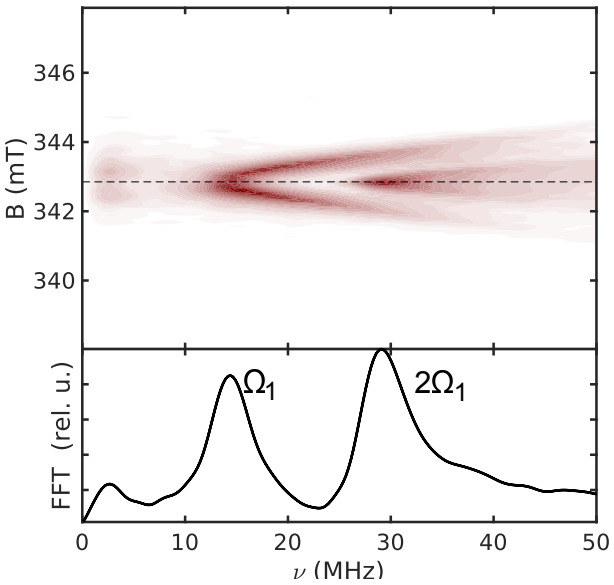


**Figure 7.6:** FFT Rabi oscillations versus magnetic field. The black dashed line marks the field position for which in the lower plot the FT spectrum is shown.

### 7.2.6 Outlook on EDMR experiments

The discussed cwEDMR and pEDMR experiments and results demonstrate that spin resonance studies on PSCs are possible and can help identify paramagnetic species in their molecular environment and the spin-dependent processes they are involved in. The study raised open questions that can be addressed with further experimental efforts.

It was proposed that the detection of EDMR spectra may be connected to the emergence of the S-shape in the *I-V* curve at low temperatures. The S-shape is presumably a result of energetic barriers at the organic/electrode interface. It is probable that spin-dependent processes start to play a role once energetic barriers emerge at these interfaces. This relation can be investigated by systematically decreasing the temperature, measuring the *I-V* curve and recording EDMR spectra allowing a direct correlation between the detection of EDMR signals and the deformation in the *I-V* characteristics. In addition, this may help identify at which organic/metal junction the barriers lie and develop strategies to reduce them.

Sufficient evidence provided by the cwEDMR study suggests that the detected $P^+$ and $P^-$ polarons in the organic layers are likely to be uncoupled and therefore undergo spin-dependent processes that are independent of each other. It would be interesting to see whether $P^+$ and $P^-$ polaron coupling across the perovskite layer can be achieved. This can be investigated by fabricating solar cells with reduced perovskite layer thicknesses and measuring Rabi oscillations, where the coherent

driving of spin nutations for weakly coupled spin pairs ($P^+$ and $P^-$ polarons) can be detected.

Furthermore, the success of EDMR detection may be due to the reduction of the Pb content in the perovskite layer. This needs to be verified and understood. The EDMR detection limit as a consequence of Pb can be investigated by systematically increasing the Pb contribution with respect to Sn in PSCs. This can also help understand the connection between the absence of spin resonance signals in standard (without Sn) PSCs, such as cells with MAPI as a the light absorber.

In conclusion, the work in this section showed that EDMR can be used as a tool to investigate transport processes in PSCs. Further experimental efforts using EDMR techniques can contribute to the understanding of transport mechanisms from the perovskite layer to the transport layers in PSCs.

## 7.3 Triplet Excitons in 2D Perovskites

Recently, Younts et al. reported on triplet exciton generation in two-dimensional (2D) perovskite $(CH_3NH_3)_2Pb(SCN)_2I_2$ (MAPSI) [169]. A photoluminescence (PL) emission peak at 1.64 eV was observed that could not be directly excited or stimulated with optical excitation (thus a dipole forbidden transition) and provided evidence for the existence of long-lived triplet excitons in MAPSI. The observation of long-lived triplet excitons in 2D perovskite may potentially allow their detection with trEPR spectroscopy. This section presents first attempts to measure triplet excitons in the 2D-perovskite MAPSI (shown in Figure 7.7c). General schemes of 3D and 2D perovskite are given in Figure 7.7a and b.

The interest in triplets lies in their ability to take part in processes, such as singlet fission, triplet-triplet annihilation or back-electron transfer. While the former two mentioned processes can raise the efficiency in photovoltaic devices, the later can function as a loss mechanism. Although these concepts are known for organic systems, in hybrid perovskites the generation of triplet states remains largely unexplored. Time resolved EPR techniques provide direct proof of triplet-excitons in addition to spectroscopic parameters that aid the understanding of their fundamental physics.

### 7.3.1 trEPR at X- and Q-Band

Quartz substrates spincoated with a thin film of 2D MAPSI were obtained from the group of Dr. David Mitzi (Duke University North Carolina U.S.A). Transient EPR measurements at X- and Q-Band frequencies were performed on the films at 10 K

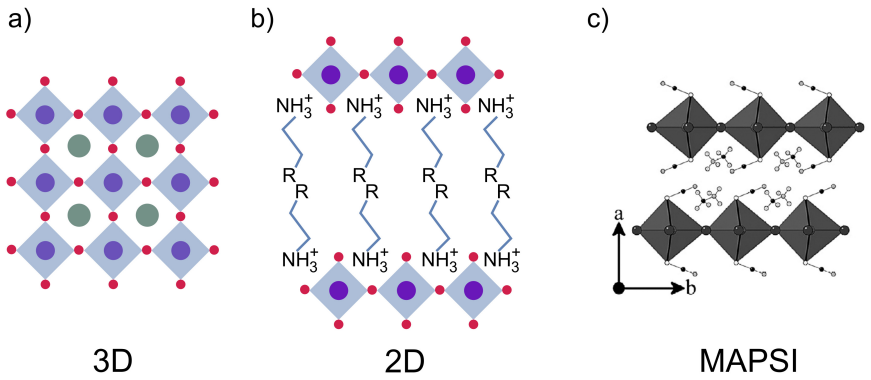


**Figure 7.7:** Schemes of a) 3D perovskite, b) 2D hybrid organic-inorganic perovskite. Purple circles represent the metal cations (Pb, Sn), red circles stand for halides (I, Br, Cl), and grey circles or inorganic (Cs) or organic (MA, FA) cations. Figures a) and b) adapted form [170]. c) MAPSI crystal structure obtained from Ref. [169].

with the diode-pumped Nd:YAG laser at the excitation wavelength of $\lambda = 532\,\text{nm}$. X-band transient spectra were recorded at a microwave attenuation of 35 dB and laser fluence of $\sim 4.7\,\text{mJ/cm}^2$. The Q-band measurements were performed at a microwave attenuation of 41 dB and laser fluence of $\sim 6.1\,\text{mJ/cm}^2$.

Due to the high SOC caused by the heavy elements Pb and I, the $g$-values are expected to largely deviate from the free electron $g$-value. Therefore and because of the lack of knowledge on the paramagnetic species in MAPSI, a broad magnetic field range was measured at X-band frequencies. Furthermore, Q-band measurements were additionally carried out to obtain further spectral resolution. The results are shown in Figure 7.8.

The X-band contour plot in Figure 7.8a indicates two relatively broad signatures, an absorptive feature in the low magnetic field range (red contour) and an emissive feature (blue contour) at higher magnetic fields. The lower plot shows the EPR spectra at selected times after the laser flash. At $0\,\mu\text{s}$ the spectrum does not exhibit any features. At early times $0.4\,\mu\text{s}$ DAF, the low-field signature appears. This is than accompanied by the high-field signal measured for DAF longer than $0.6\,\mu\text{s}$. The two signals become distinctive at $2.6\,\mu\text{s}$. The low-field signal decays after $6\,\mu\text{s}$ wheres the high field signal is long lived and shows a decrease in intensity however does not completely decay within the measured time scale.

The blue dashed line marks the emissive signal component on the magnetic field axis. The feature has its signal minimum around $g_1 = 2.065$. The red-dashed line marks $g_2 = 2g_1$, at half-field of $g_1$. This is the region where a half-field transition is expected in the case that the signal of $g_1$ is a triplet exciton. The expected half-field transition coincides with the absorptive signal in the low-field region.

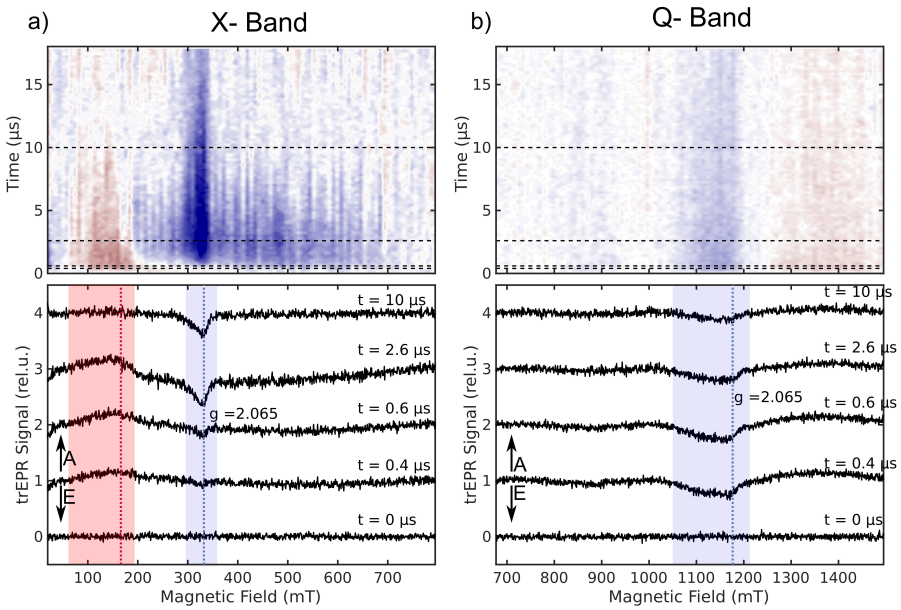


**Figure 7.8:** X- a) and Q-band b) trEPR measurements on MAPSI thin films. The 2D-plot gives the signal intensity with respect to DAF and magnetic field position. Red indicates microwave absorption and blue microwave emission. The lower plot shows selected time slices with the red-dashed line marking a signal that may be attributed to a half-field transition. The red-shaded area indicates the field range of the absorptive signal. The blue-shaded area covers the high-field signal of $g = 2.065$, marked by the blue-dashed line.

It is difficult to analyze the spectral shape of the high-field signal at $g_1$. The signal is asymmetric in shape and is about 76 mT wide. Q-band measurements can provide more spectral resolution on the magnetic field axis. Figure 7.8b shows the contour plot with the selected time slices and mark an emissive signal detected with the blue-dashed line at $g_1 = 2.065$: the same high-field signal detected at X-band. The signal maintains its linewidth going from X-band to Q-Band. This might hint towards a hyperfine-broadened signal. Figure 7.9 shows a combined plot of the measurements performed in X- (black) and Q-band (blue) on the same magnetic field axis. The low-field signal is not contained in the magnetic field range of the Q-band measurement.

### 7.3.2 Discussion

X- and Q-band trEPR spectra were measured on the 2D perosvkite MAPSI at 10 K to explore the long-lived triplet excitons reported on in Ref. [169]. Preliminary X-band results indicated two features: one at $g_1 = 2.065$ and one at approximately half-field of $g_1$. The observation of a half-field transition implies triplet excitons are present in the 2D perovskite sample. The full-field signal at $g_1$ is not detected as a conventional EPR triplet spectrum. The lack of resolution even at Q-Band makes the interpretation of the signal difficult.

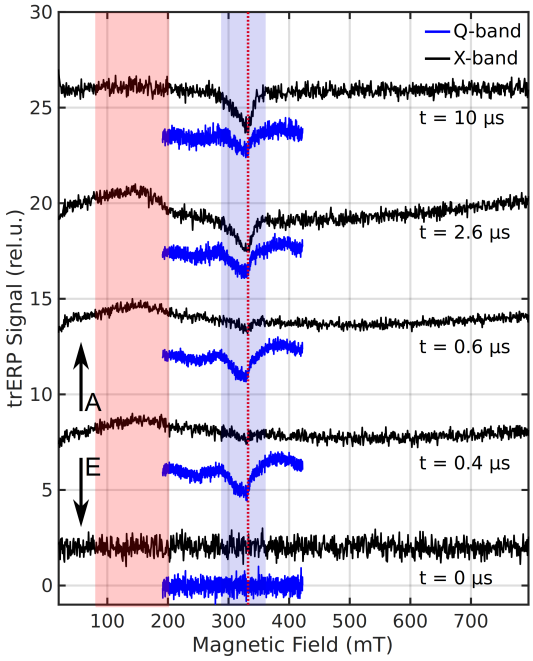


**Figure 7.9:** Times slices of Figure 7.8 plotted on the same magnetic-field axis. Red and blue shaded areas mark the same transitions as in Figure 7.8 with the red-dashed line marking $g_1 = 2.065$.

The trEPR detection involved some difficulties induced by a large photo-induced non-resonant background coming from the perovskite sample. It is expected that due to generation of a large number of charge carriers upon photoexcitation, the perovskite film becomes extremely conductive, causing additional electric fields that distort the cavity modes. These additional fields interact with the electric field of the microwave, resulting in a non-resonant microwave absorption. This causes the resonator $Q$-factor to drop, thereby reducing the detection sensitivity.

A control trEPR experiment was performed to demonstrate the decrease in detection sensitivity due to an increased off-resonant background. Two individual substrates were fabricated: one containing a thick film of 5,6,11,12-tetraphenyltetracene, referred to as rubrene (an organic semiconductor known to undergo singlet fission [171, 172]) and one only containing $CH_3NH_3PbI_3$ (MAPI), which is expected to quench resonant signals. A schematic structure of MAPI, which is a 3D perovskite is shown in Figure 7.7a. Figure 7.10a shows in red the trEPR spectrum detected at 0.5 $\mu$s DAF for the rubrene film. The spectrum contains two peaks and the spectral shape resembles one of a thermalized triplet. The blue spectrum, displays the trEPR detection also at 0.5 $\mu$s DAF through a rubrene film, however for a sample containing both the rubrene and MAPI substrates. This shows that the inclusion of the MAPI film in the resonator quenches the resonance signals of rubrene.

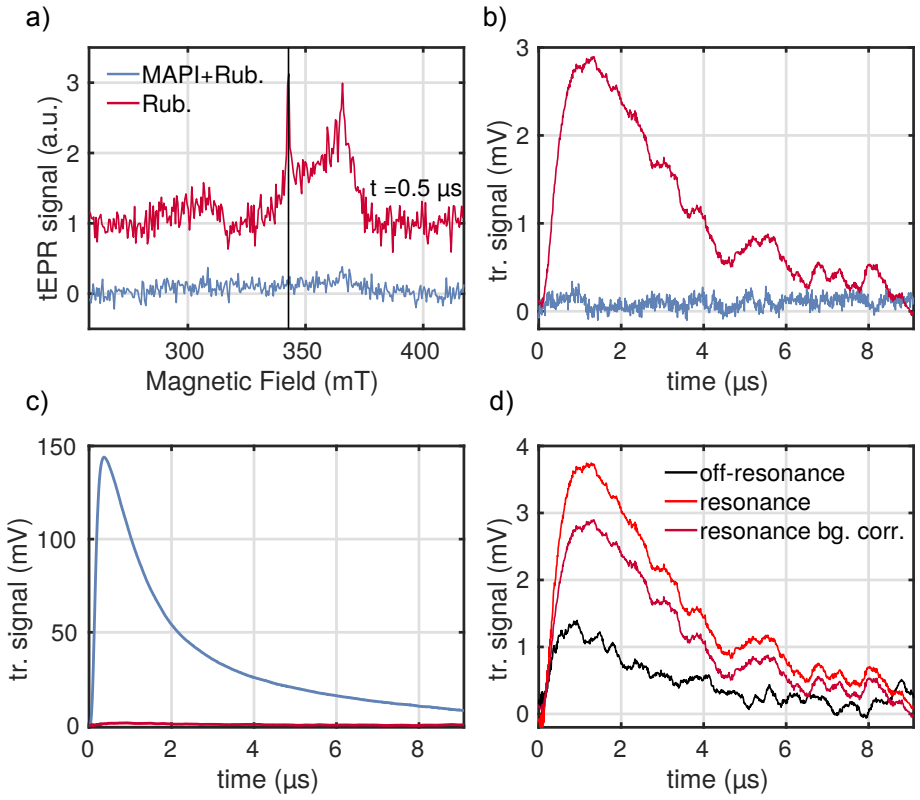


**Figure 7.10:** The transient response of the rubrene sample with and without MAPI: a) trEPR signal detected at 0.5 $\mu$s DAF with two absorptive signals. The black line marks the magnetic field position of one of the signals with b) showing the signal response with time at the marked field. c) The off-resonant background for the rubrene and MAPI-rubrene sample. d) Comparison of the transient response of the rubrene sample (at the marked field position) with and without subtraction of the off-resonant background. The off-resonant background is given in black for comparison.

Figure 7.10c displays the signal response of the sample when detecting off resonance, demonstrating the significantly large difference of more than two orders of magnitude in the intensity of the off-resonant background between the rubrene (red) and the MAPI-rubrene sample (blue). The off-resonant background is subtracted to obtain a background corrected trEPR spectrum. Figure 7.10b shows the result of the background correction at the magnetic field position marked by the black line in Figure 7.10a. The rubrene sample indicates a clear rise and decay of the absorption signal, whereas the time trace obtained for the MAPI-rubrene sample at the same field position is flat. For comparison Figure 7.10d demonstrates the difference between off-resonant and resonant signal response for the rubrene sample, and the resulting transient after background correction.

From the performed control experiment we concluded that different strategies need to be used for the investigation of photoconductive perovskite samples. To overcome the cavity losses, a resonator designed to investigate polar liquid samples (known

to be highly conductive), such as cylindrical mode resonators, can be used [71, 76]. With the help of special sample holders, the sample position in the cavity can be optimized, such that it is placed in the magnetic field maximum and electric field minimum.

Furthermore, to bypass the large photo-induced non-resonant background an excitation saturation experiment can be considered. This entails photoexciting the material close to saturation with a continuous wave laser, creating a high concentration of photogenerated charge carriers. This would presumably eliminate the off-resonant background. Conventional trEPR measurement can then be performed, where now only a small charge-carrier ensemble is created by the laser flash and detected in EPR.

## 7.4 Conclusion and Outlook

This chapter has demonstrated first attempts at studying perovskite-based materials and solar cells with EPR techniques. In the first part, it was shown that spin-dependent processes can be detected in the transport layers of the Sn-Pb based PSCs. In the second part, the 2D perovskite MAPSI, reported to exhibit long-lived triplet excitons, was investigated with trEPR, where signatures at full-field and half-field were detected implying the existence of triplets.

It was proposed that, due to the strong SOC in systems consisting of heavy atoms, such as Pb in perovskite, EPR spectroscopy can become challenging. The perovskite samples used for the presented studies all contained some amounts of Pb. Furthermore, the paramagnetic lead cations $Pb^{+}$ and $Pb^{3+}$ have been observed previously with EPR techniques [173–175] in Pb-containing compounds. It is therefore hypothesized that the reason for the lack of success of the EPR technique for the investigation of perovskite materials should be less related to the presence of Pb and more connected to the overall perovskite framework. This hypothesis is discussed in the following.

In a crystal lattice, a symmetry breaking perturbation such as local strains or internal electric fields in the presence of SOC, will cause a splitting of energy bands (Rashba splitting) [176–178]. If the perturbation is not homogeneous across the sample, which is often the case for materials of structural disorder, it can lead to extreme inhomogeneous broadening of the EPR lines [179, 180]. This was for instance the case for p-type silicon, where initially observation of paramagnetic resonance was only possible under application of external stress [179].

Studies have identified lattice strains in polycrystalline perovskite films [178, 181–183]. Lattice strain is directly associated with enhanced defect concentrations in

perovskite films [184] and is therefore a source of instability and worsens device performance. It was observed that the strain was formed by the high temperature annealing process and caused by the thermal expansion mismatch between the perovskite material and substrate. Strain engineering can be exploited to tailor optoelectronic functionalities or for the purpose of EPR studies, unstrained perovskite films can aid the investigations with spin resonance techniques.

Strategies to reduce internal strains in disordered materials include the application of external stress [179], for instance in the form of pressure [181]. It was also shown that by increasing crystalline quality [185, 186] strains are reduced. Zhoa et al. fabricated strain-free control samples that consisted of millimeter-sized single crystals and powders created by scratching the perovskite film prepared on a substrate [178].

From the perspective of device optimization, techniques that ensure the fabrication of strain-free and the growth of highly crystalline perovskite films enable the enhancement of solar cell stability and performance. For the prospect of EPR investigations, unstrained perovskite films may provide the accessibility to the spin degree of freedom, thus allowing to shed light on spin relevant interactions and processes in the material.

Chapter 8

# Conclusion and Outlook

The studies discussed in this thesis aimed to advance our understanding of the fundamental processes in organic and perovskite materials for photovoltaic applications. By using EPR spectroscopy and the EDMR technique we were able to investigate the microscopic nature and dynamics of charge carriers in disordered materials.

The small organic molecule spiro-OMeTAD is one of the most frequently used hole transport material in PSCs. To increase its conductivity, spiro-OMeTAD is p-doped. However, since the conductivity is influenced not only by the charge carrier concentration but also by the charge carrier mobility, conductivity measurements cannot give conclusive information on the effectivness of doping. EPR allows to quantitatively investigate the effect of doping independent from mobility effects. The prerequisite for doping studies in EPR is the knowledge of the EPR spectrum. Therefore, a detailed analysis of the detected EPR signal in doped spiro-OMeTAD solution and disordered film samples was performed using a multi-frequency EPR approach. The origin of the EPR spectrum was clearly identified as the hole on the molecule and the nature of the EPR-active charge carrier was shown to be independent of the dopant. A difference in spectral shape between solutions and films was found. DFT based EPR simulations showed that the difference in spectral shape is a consequence of the different charge carrier distribution on the molecule in different environments: while in the liquid phase the charge carrier distribution extends over the entire molecule, it becomes localized on a single arm of spiro-OMeTAD in the solid state. The charge carrier distribution on the spiro-OMeTAD molecule in a disorder environment will have consequences on the charge transport.

The spiro-OMeTAD doping study conducted with quantitative EPR revealed that the main doping agent is FK209, with a doping efficiency of $\sim 81\%$ compared to Li-TFSI with an efficiency of less than 2%. Doping by means of both additives will not enhance the efficiency and instead keeps it constant at the level achieved by FK209 alone. However, Li-TFSI seems as an efficient p-dopant in conductivity measurements. We conclude that the significant increase in conductivity is rather connected to an improved charge mobility. Nevertheless, the inclusion of Li-TFSI might still be required for an efficiently operating PSC, as it is known that $Li^+$ ion migration towards the TCO surface under device operation facilitates photocurrent generation [112]. This shows that although we investigated the role of the additives

on spiro-OMeTAD as an individual material, it is still necessary to consider the complete device under operation to explore the microscopic interactions affecting the charge transport and hence, device performance.

EDMR is a convenient method that allows the investigation of charge carrier transport processes under device operation. In EDMR the spin is used as a probe for the identification of current influencing processes and the type of spin species they involve under microwave resonance. However, the requirement for the proper evaluation of EDMR spectra is the knowledge about the origin of the EPR signatures. Therefore a detailed EPR spectral analysis is essential for understanding EDMR data.

The usefulness of simultaneously conducting EPR and EDMR measurements was demonstrated for a PSBTBT-8:PCBM BHJ solar cell. A similar material blend (Si-PCPDTBT:PCBM) has been previously investigated by Kraffert et al. [84], where the evolution of light-induced EPR signals from excitons at the CT-state to uncoupled $P^+$ and $P^-$ polarons was identified using trEPR. In this thesis, this study was extended by the simultaneous measurement of trEDMR on the BHJ device under variable operation conditions and allowed the correlation between the polarons detected in trEPR and their involvement in spin-dependent processes detected in trEDMR. We were able to separate their dynamics with an SVD approach. This allowed us to study the temporal evolution of both $P^+$ and $P^-$ individually. The spectral signatures remained unchanged under variation of the bias voltage, while the dynamics of the trEDMR signals changed markedly after exciton generation. For short delays after optical excitation, similar dynamics for $P^+$ and $P^-$ were measured, indicating that the signal in EDMR originates from a resonant decrease in recombination at the CT-state (at the polymer/fullerene interface). For longer delays after excitation we found that the evolution of the $P^+$ polaron (in PSBTBT-8) and the $P^-$ polaron (in PCBM) signals differ on the detected time scale. We concluded that the detected signals stem from different spin-dependent processes, that exclusively involve $P^+$ and $P^-$ in their respective layers. Such processes can be related to the transport of the polarons in the disordered environment and aided by spin resonance. This study has provided valuable insight into the spin-dependent dynamics of light-induced charge carriers. The employed strategy can serve as a tool to study transport processes and loss mechanisms affecting photovoltaic energy conversion in related material systems, such as PSCs.

One of the key questions in this work was whether spin-dependent dynamics can be measured in perovskite materials and solar cells. This includes the dynamics of triplet states, charge transport through CT-states, as well as spin-dependent transport and recombination. Therefore, part of this work focused on the investigation of spin-dependent physics in perovskite materials and solar cells. First attempts at detecting EPR signals in state-of-the-art perovskite materials were unsuccessful.

Although the reason so far is unclear, it is believed to be connected to the strong SOC in the perovskite building block.

Reports have shown that the SOC can be reduced by substitution of Pb in the perovskite by Sn. We decided to follow this strategy and conduct EDMR experiments on Sn-based perovskite solar cells. In addition, polymers and fullerenes, similar to the ones used in the organic BHJ investigated in chapter 6, were employed as transport layers and resulted in a PSC with a PCE of $\sim$ 13%. Since the detection of EDMR signals was only possible at temperatures $< 80\,\mathrm{K}$, the question was raised wether this is connected to the emergence of the S-shape in the $I$-$V$ curves at low temperatures. This is an interesting aspect to consider and compare to OSCs, where EDMR signals are detectable at any given temperature including room temperature. The relation between the solar cell $I$-$V$ characteristics and EDMR signals will be addressed in future work. We were able to identify the origin of the main signals in the EDMR spectrum as the $P^+$ polarons in the HTL PEDOT and the $P^-$ in the ETL $C_{60}$. These polarons are unlikely to be coupled and thus undergo different spin-dependent processes in their respective layers. Moreover, we showed that while the polarons are detected in their respective transport layers, they are indeed photogenerated in the perovskite layer. Hence, further experimental work aims at determining the polaron transport pathways or mechanisms from the perovskite to the transport layers. The success of EDMR detection on Sn-based PSCs provides the prospect to explore the connection between the perovskite material and the absence of spin resonance signals.

Motivated by recent reports on the observation of long-lived triplets in the 2D perovskite MAPSI, a multi-frequency trEPR study was conducted to determine the population mechanism and depopulation of the triplet state, as well as spectroscopic parameters such as the $g$-value and ZFS parameters. X-band results indicated two features: one at $g_1 = 2.065$ and one at approximately half-field of $g_1$. The observation of a half-field transition implies triplet excitons are present in MAPSI. Several challenges were faced during measurements. We observed a large off-resonant background coming from the perovskite samples, which is likely connected to the high photoconductivity of the material. Highly conductive samples can result in non-resonant absorption of microwaves, causing a drop in the resonator sensitivity. This makes the detection of resonant changes on top of a large off-resoant background extremely difficult. We conclude that this complication can be overcome by employing microwave resonators (Bruker flat-cell resonators) designated for highly conductive samples.

Insight gained from organic materials and devices can partly be applied to PSCs. Particularly, the organic materials either used as polymer/fullerene blends in BHJ or charge-selective layers in perovskite solar cells indicate that spin-dependent processes play a significant role in charge transport. It is, however, the perovskite/organic interface that remains unexplored in EPR so far, due to the complications caused by

the perovskite material in the resoantor. From the challenges confronted with we learned that different strategies need to be used when investigating perovskite samples. This includes the development of an experimental setup equipped to withstand highly conductive samples, as well as sample engineering for the purpose of EPR investigations. Future experimental efforts will be devoted to identifying transport pathways at the organic/perovskite junction.

Within the range of materials investigated in this work, we were able to shed light on fundamental properties of organic materials for the application of OSC and PSC that further our understanding of how charge carriers interact in their disordered environment and under device operating conditions. With the experimental strategies presented here, there is potential to further explore the fundamental physics in devices based on organic and perovskite materials for photovoltaic application. The contribution of this work is part of a larger field of research, invested in third generation solar cells, allowing us to move closer to large scale use of clean energy conversion devices.

# Appendices

Appendix A

# Results of Spiro-OMeTAD Doping Series

Table A.1: Doping ratio vs. spin concentration of FK209-doped spiro-OMeTAD.

| Doping Ratio | $V_{\text{sample}}$ [$\mu$l] | $V_{\text{film}}$ [m$^3$] | $C_1$ [m$^{-3}$] | $C_2$ [m$^{-3}$] | $C_3$ [m$^{-3}$] |
|---|---|---|---|---|---|
| Batch 1 | | | | | |
| 1 : 1 | 30 | $4.9 \cdot 10^{-10}$ | $3.3 \cdot 10^{26}$ | $3.6 \cdot 10^{26}$ | $3.7 \cdot 10^{26}$ |
| 1 : 10 | 30 | $5.9 \cdot 10^{-10}$ | $4.6 \cdot 10^{25}$ | | |
| 1 : 100 | 30 | $5.0 \cdot 10^{-10}$ | $9.9 \cdot 10^{24}$ | | |
| 1 : 1000 | 30 | $5.0 \cdot 10^{-10}$ | $1.2 \cdot 10^{24}$ | | |
| Batch 2 | | | | | |
| 1 : 5 | 30 | $5.8 \cdot 10^{-10}$ | $1.3 \cdot 10^{26}$ | | |
| 1 : 50 | 30 | $5.8 \cdot 10^{-10}$ | $1.5 \cdot 10^{25}$ | | |
| 1 : 500 | 30 | $5.8 \cdot 10^{-10}$ | $1.8 \cdot 10^{24}$ | | |
| 1 : 5000 | 30 | $5.8 \cdot 10^{-10}$ | $2.4 \cdot 10^{23}$ | | |
| 1 : 50 000 | 30 | $5.8 \cdot 10^{-10}$ | $4.0 \cdot 10^{22}$ | | |

Table A.2: Doping ratio vs. spin concentration of FK209-doped spiro-OMeTAD.

| Doping Ratio | $V_{\text{sample}}$ [$\mu$l] | $V_{\text{film}}$ [m$^3$] | $C_1$ [m$^{-3}$] | $C_2$ [m$^{-3}$] | $C_3$ [m$^{-3}$] |
|---|---|---|---|---|---|
| Batch 3 | | | | | |
| 1 : 10 | 30 | $1.2 \cdot 10^{-9}$ | $7.4 \cdot 10^{25}$ | | |
| 1 : 100 | 30 | $1.2 \cdot 10^{-9}$ | $2.7 \cdot 10^{24}$ | | |
| 1 : 1000 | 60 | $2.3 \cdot 10^{-9}$ | $7.9 \cdot 10^{22}$ | | |
| 1 : 10 000 | 60 | $2.3 \cdot 10^{-9}$ | $4.3 \cdot 10^{22}$ | | |
| 1 : 100 0000 | 60 | $2.3 \cdot 10^{-9}$ | $4.6 \cdot 10^{22}$ | | |
| Batch 4 | | | | | |
| 1 : 10 | 60 | $1.8 \cdot 10^{-10}$ | $8.8 \cdot 10^{25}$ | $8.4 \cdot 10^{25}$ | |
| 1 : 100 | 60 | $1.8 \cdot 10^{-10}$ | $6.2 \cdot 10^{24}$ | $5.9 \cdot 10^{24}$ | |
| 1 : 1000 | 60 | $1.8 \cdot 10^{-10}$ | $4.4 \cdot 10^{23}$ | $3.7 \cdot 10^{23}$ | |
| 1 : 10 000 | 60 | $9.2 \cdot 10^{-10}$ | $1.1 \cdot 10^{23}$ | $9.7 \cdot 10^{22}$ | |
| 1 : 100 0000 | 60 | $9.2 \cdot 10^{-10}$ | $1.3 \cdot 10^{23}$ | $1.4 \cdot 10^{23}$ | |

Table A.3: Doping ratio vs. mean spin concentration $\overline{C}$ and standard deviation $\sigma$ of FK209 doped spiro-OMeTAD.

| Doping Ratio | $\overline{C}$ [m$^{-3}$] | $\sigma$ [m$^{-3}$] |
|---|---|---|
| 1 : 1 | $3.4 \cdot 10^{26}$ | $6.3 \cdot 10^{25}$ |
| 1 : 10 | $7.1 \cdot 10^{25}$ | $1.7 \cdot 10^{25}$ |
| 1 : 100 | $6.4 \cdot 10^{24}$ | $2.6 \cdot 10^{24}$ |
| 1 : 1000 | $7.3 \cdot 10^{23}$ | $2.8 \cdot 10^{23}$ |
| 1 : 10 000 | $1.0 \cdot 10^{23}$ | $1.8 \cdot 10^{22}$ |
| 1 : 100 000 | $8.3 \cdot 10^{22}$ | $6.0 \cdot 10^{22}$ |

Table A.4: Spin concentration of pristine spiro-OMeTAD.

| Sample nr. | $V_{\text{sample}}$ [$\mu$l] | $V_{\text{film}}$ [m$^3$] | $C_1$ [m$^{-3}$] | $C_2$ [m$^{-3}$] | $C_3$[m$^{-3}$] |
|---|---|---|---|---|---|
| 1 | 60 | $2.3 \cdot 10^{-9}$ | $3.2 \cdot 10^{22}$ | $1.5 \cdot 10^{22}$ | $2.3 \cdot 10^{22}$ |
| 2 | 60 | $2.2 \cdot 10^{-9}$ | $1.4 \cdot 10^{22}$ | – | $9.9 \cdot 10^{21}$ |
| 3 | 100 | $2.0 \cdot 10^{-9}$ | $3.8 \cdot 10^{22}$ | – | $3.8 \cdot 10^{22}$ |
| $\overline{C}$ [m$^{-3}$] | $2.4 \cdot 10^{22}$ | | | | |
| $\sigma$ [m$^{-3}$] | $1.0 \cdot 10^{22}$ | | | | |

Table A.5: Doping ratio vs. mean spin concentration of Li-TFSI-doped spiro-OMeTAD.

| Doping Ratio | $V_{\text{sample}}$ [$\mu$l] | $V_{\text{film}}$ [m$^3$] | $C_1$ [m$^{-3}$] | $C_2$ [m$^{-3}$] | $C_3$ [m$^{-3}$] |
|---|---|---|---|---|---|
| Batch 1 | | | | | |
| 1 : 1 | 30 | $6.0 \cdot 10^{-10}$ | $6.2 \cdot 10^{23}$ | | |
| 1 : 2 | 30 | $6.0 \cdot 10^{-10}$ | $3.6 \cdot 10^{23}$ | | |
| Batch 2 | | | | | |
| 1 : 1 | 30 | $4.9 \cdot 10^{-10}$ | $2.0 \cdot 10^{24}$ | | |
| Batch 3 | | | | | |
| 1 : 10 | 60 | $1.8 \cdot 10^{-10}$ | $8.8 \cdot 10^{25}$ | $8.4 \cdot 10^{25}$ | |
| 1 : 100 | 60 | $1.8 \cdot 10^{-10}$ | $6.2 \cdot 10^{24}$ | $5.9 \cdot 10^{24}$ | |
| 1 : 1000 | 60 | $1.8 \cdot 10^{-10}$ | $4.4 \cdot 10^{23}$ | $3.7 \cdot 10^{23}$ | |
| 1 : 10 000 | 60 | $9.2 \cdot 10^{-10}$ | $1.1 \cdot 10^{23}$ | $9.7 \cdot 10^{22}$ | |
| 1 : 100 0000 | 60 | $9.2 \cdot 10^{-10}$ | $1.3 \cdot 10^{23}$ | $1.4 \cdot 10^{23}$ | |
| Batch 4 | | | | | |
| 1 : 10 | 50 | $1.6 \cdot 10^{-9}$ | $4.9 \cdot 10^{23}$ | $5.2 \cdot 10^{23}$ | |
| 1 : 25 | 50 | $1.6 \cdot 10^{-9}$ | $4.0 \cdot 10^{23}$ | $4.1 \cdot 10^{23}$ | $4.5 \cdot 10^{23}$ |
| 1 : 50 | 50 | $1.6 \cdot 10^{-9}$ | $2.9 \cdot 10^{23}$ | $5.0 \cdot 10^{23}$ | $6.2 \cdot 10^{23}$ |
| 1 : 75 | 50 | $1.6 \cdot 10^{-9}$ | $1.9 \cdot 10^{22}$ | $2.1 \cdot 10^{23}$ | $2.1 \cdot 10^{23}$ |
| 1 : 100 | 50 | $1.6 \cdot 10^{-9}$ | $1.6 \cdot 10^{23}$ | $1.7 \cdot 10^{23}$ | $1.5 \cdot 10^{23}$ |
| 1 : 200 | 50 | $1.6 \cdot 10^{-9}$ | $1.3 \cdot 10^{22}$ | $1.3 \cdot 10^{23}$ | $1.2 \cdot 10^{23}$ |

Table A.6: Doping ratio vs. mean charge density $\overline{C}$ and standard deviation $\sigma$ of Li-TFSI doped spiro-OMeTAD.

| Doping Ratio | $\overline{C}\,[\mathrm{m}^{-3}]$ | $\sigma\,[\mathrm{m}^{-3}]$ |
|---|---|---|
| 1 : 1 | $1.6 \cdot 10^{24}$ | $6.9 \cdot 10^{23}$ |
| 1 : 2 | $4.4 \cdot 10^{23}$ | $3.7 \cdot 10^{23}$ |
| 1 : 10 | $1.1 \cdot 10^{24}$ | $6.5 \cdot 10^{23}$ |
| 1 : 25 | $4.1 \cdot 10^{23}$ | $3.9 \cdot 10^{22}$ |
| 1 : 50 | $5.1 \cdot 10^{23}$ | $1.7 \cdot 10^{23}$ |
| 1 : 75 | $2.1 \cdot 10^{23}$ | $1.3 \cdot 10^{22}$ |
| 1 : 100 | $1.8 \cdot 10^{23}$ | $2.1 \cdot 10^{22}$ |
| 1 : 200 | $1.3 \cdot 10^{23}$ | $5.4 \cdot 10^{21}$ |
| 1 : 1000 | $9.1 \cdot 10^{22}$ | $1.1 \cdot 10^{23}$ |

Table A.7: Doping ratio vs. mean spin concentration of Li-TFSI-doped spiro-OMeTAD.

| Doping Ratio FK209 | Doping Ratio Li-TFSI | $V_{\mathrm{sample}}\,[\mu\mathrm{l}]$ | $V_{\mathrm{film}}\,[\mathrm{m}^3]$ | $C_1\,[\mathrm{m}^{-3}]$ | $C_2\,[\mathrm{m}^{-3}]$ |
|---|---|---|---|---|---|
| 1 : 10 | 1 : 2 | 30 | $5.8 \cdot 10^{-9}$ | $6.2 \cdot 10^{25}$ | $7.1 \cdot 10^{25}$ |
| $\overline{C}\,[\mathrm{m}^{-3}]$ | $6.6 \cdot 10^{25}$ | | | | |
| $\sigma\,[\mathrm{m}^{-3}]$ | $5.7 \cdot 10^{24}$ | | | | |
| 1 : 1 | 1 : 1 | 30 | $5.8 \cdot 10^{-9}$ | $3.1 \cdot 10^{26}$ | $4.5 \cdot 10^{26}$ |
| $\overline{C}\,[\mathrm{m}^{-3}]$ | $3.8 \cdot 10^{26}$ | | | | |
| $\sigma\,[\mathrm{m}^{-3}]$ | $9.9 \cdot 10^{25}$ | | | | |

Appendix B

# Results of Conductivity Measurements

Table B.1: Results obtained from conductivity measurements by mercury probe: $c1$ was measured directly after fabrication, $c2$ after 24 hours, and $c3$ after 48 hours.

| Material and doping ratio | $c1\,[S\mathrm{m}^{-1}]$ | $c2\,[S\mathrm{m}^{-1}]$ | $c3\,[S\mathrm{m}^{-1}]$ |
|---|---|---|---|
| (i) pristine spiro-OMeTAD | $7.7 \cdot 10^{-8}$ | $2.2 \cdot 10^{-7}$ | $3.4 \cdot 10^{-7}$ |
| (ii) pristine spiro-OMeTAD | $6.5 \cdot 10^{-8}$ | $2.0 \cdot 10^{-7}$ | $4.7 \cdot 10^{-7}$ |
| (iii) Li-TFSI:spiro-OMeTAD (1:0) | $2.1 \cdot 10^{-4}$ | $7.7 \cdot 10^{-5}$ | $1.7 \cdot 10^{-4}$ |
| (iv) Li-TFSI:spiro-OMeTAD (1:0) | $1.7 \cdot 10^{-4}$ | $7.0 \cdot 10^{-5}$ | $9.4 \cdot 10^{-5}$ |

Appendix C

# DFT Results

Table C.1: Parameters obtained from DFT for the symmetrized spiro-OMeTAD molecule. The nitrogens are labeled as in Figure 5.5 of the main text.

| | $A$-tensor principle values [MHz] | $a_{\mathrm{iso}}$ [MHz] | Euler angles [Deg] |
|---|---|---|---|
| N1 | (0.7661 0.7796 15.5320) | 5.6926 | (-34.6 21.5 -24.0) |
| N2 | (0.4669 0.4853 11.4889) | 4.1470 | (-27.8 33.8 -19.9) |
| N3 | (0.4704 0.4890 11.5330) | 4.1641 | (27.4 34.0 20.5) |
| N4 | (0.7688 0.7820 15.5963) | 5.7157 | (34.8 21.1 23.8) |
| | $g$-tensor principal values | $g_{\mathrm{iso}}$ | |
| | (2.0029560 2.0030603 2.0036711) | 2.0032291 | |

Table C.2: Parameters obtained from DFT for the single crystal spiro-OMeTAD molecule.

| | $A$-tensor principle values [MHz] | $a_{\mathrm{iso}}$ [MHz] | Euler angles [Deg] |
|---|---|---|---|
| N1 | (-0.0018 -0.0153 0.0270) | 0.0033 | (27.4 36.0 6.2) |
| N2 | (1.9944 2.0627 14.4481) | 6.1684 | (-21.5 37.4 -69.5) |
| N3 | (-0.0091 -0.0158 0.0188) | -0.0020 | (-2.8 15.1 67.9) |
| N4 | (4.4404 4.4808 50.4474) | 19.7895 | (-7.1 69.9 -43.5) |
| | $g$-tensor principal values | $g_{\mathrm{iso}}$ | |
| | (2.0028628 2.0030380 2.0037071) | 2.0032026 | |

Appendix D

# PEDOT:PSS

The preparation of the sample took place outside of the glove box, as PEDOT:PSS is not air sensitive. The PEDOT:PSS suspension was put inside an ultrasonic bath for 5 min. Adequate amounts of the suspension were filled in an EPR quartz tube (3.9 mm outer diameter). The solution was dried under vacuum leaving a film on the wall of the tube. The film was annealed for $\sim 10$ min. at 100° C. Afterwards the tube was filled with helium and sealed by blow torch.

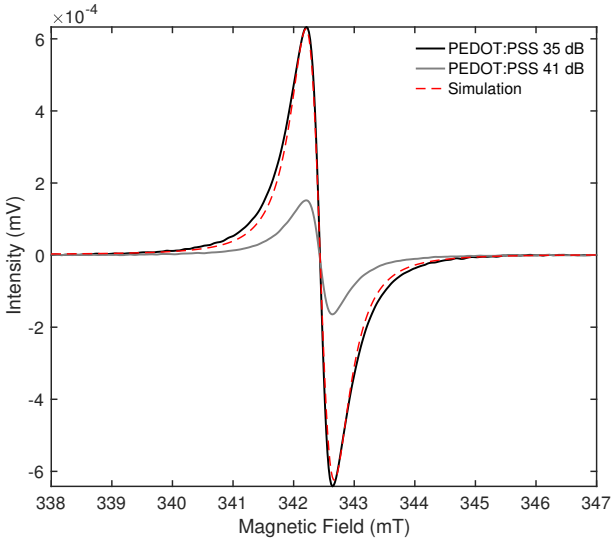


**Figure D.1:** PEDOT:PSS EPR spectrum measured at room temperature with the indicated microwave attenuation and 1 G modulation amplitude.

X-band spectra were recorded on Lyra at microwave attenuations of 35 and 41 dB, 100 kHz modulation frequency and 1 G modulation amplitude. The spectra are shown in Figure D.1 in black and grey. The spectrum recorded at 41 dB, 100 kHz is 4 times lower in intensity compared to the spectrum obtained at 35 dB. This indicates that the spectrum is not saturated at either microwave powers.

The simulation was obtained by fitting the experimental spectrum with the (least-squares fitting) function esfit *esfit* and the simulation function for solid-state EPR spectra provided by the Easyspin toolbox in Matlab [82]. A $g$-value of 2.0029(4) was

determined. A Lorentzian line shape of 0.80 mT was found to describe the spectrum at best. The Lorentzian shape accounts for increased spin-spin interaction in the sample, due to the highly p-doped $\pi$-conjugated thiophene chains [161].

Appendix E

# Modulation Frequency

The dependence of the modulation frequency on the cwEDMR spectrum was examined. Spectra were recorded under illumination at 20 dB microwave attenuation, open circuit conditions, and 80 K. These are shown in Figure E.1. The assignment

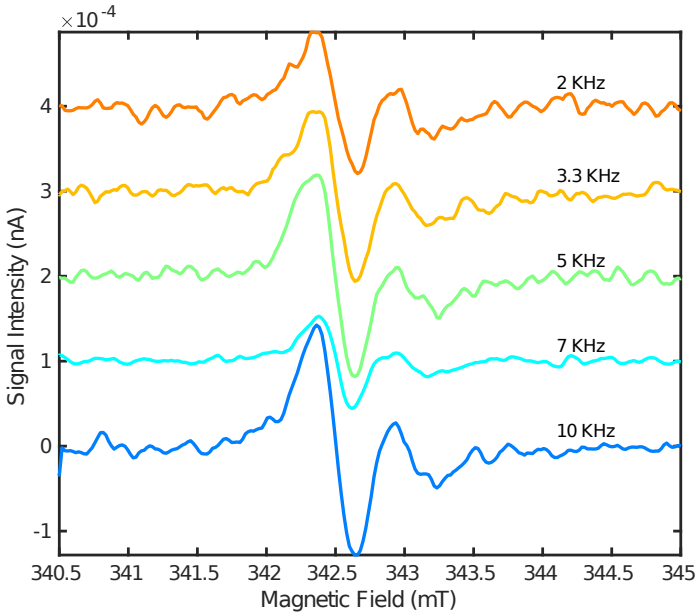


**Figure E.1:** CwEDMR vs. applied modulation frequency measured on a SnPb-based perovskite solar cell. The spectra were measured at 80 K, 20 dB under illumination at open circuit conditions $U \approx 0$. The spectra were all recorded with a 0.26 mT modulation amplitude, except the 7 KHz spectrum, which was measured with a modulation amplitude of 0.12 mT.

of the signatures can be found in section 7.2. The CR signal and the $P^-$ signal grow in intensity with faster modulation frequencies. Low frequencies between $2-5$ kHz indicate a shoulder on the low field side of the spectrum which is ascribed to PEDOT. This shoulder does not grow in intensity when modulating faster, compared to the other signals. At 10 kHz the highest signal intensity is obtained with respect to the CR signal and the $P^-$ signal.

In order to resolve the signals in the spectrum, a modulation amplitude of 4 kHz was selected for the bias-dependent study (section 7.2.2). In the wavelength dependent investigation (section 7.2.3) a modulation frequency of 10 kHz was chosen.

Appendix F

# Sn-Pb PSC EDMR Spectrum Simulations

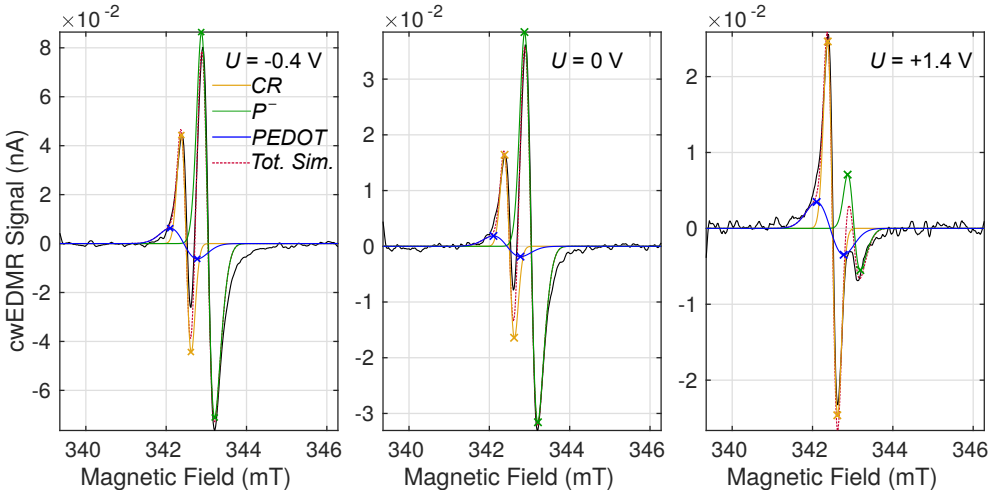


**Figure F.1:** EDMR spectra of Sn-Pb PSC measured under different applied bias voltages and using cw diode laser with $\lambda = 532\,\text{nm}$ as the illumination source (black). The total simulation (red dashed line) consists of the CR-line (yellow), PEDOT-line (blue), and $P^-$-line (green). The crosses in the respective colors indicate the maximum and minimum of the simulated signature.

Bias-dependent EDMR spectra shown in black in Figure F.1 are simulated using the Easyspin toolbox in Matlab [82]. The simulation parameters can be found in Table 7.2. The total simulation indicated by the red-dashed line consists of the individual simulation of the CR line (yellow), PEDOT (blue), and $P^-$ in $C_{60}$ (green). The crosses on the simulations mark the maxima and minima of the signature. These values are used to determine the peak-to-peak intensity. The peak-to-peak intensity of each spectral feature gives the absolute spin-dependent EDMR current $\Delta I_{\text{EDMR}}$. This value is used to calculate $\xi_{\text{EDMR}}$ according to equation 7.1.

# Bibliography


[1] O. Morton. "A new day dawning?: Silicon Valley sunrise". In: *Nature* 443 (2006), pp. 19–22.

[2] E. W. McFarland. "Solar energy: setting the economic bar from the top-down". In: *Energy Environ. Sci.* 7 (3 2014), pp. 846–854.

[3] M. Green. *Third Generation Photovoltaics*. Springer-Verlag/Berlin, 2006.

[4] L. E. Chaar, L. A. Iamont, and N. E. Zein. "Review of photovoltaic technologies". In: *Renewable and Sustainable Energy Reviews* 15.5 (2011), pp. 2165–2175.

[5] H. Shirakawa et al. "Synthesis of electrically conducting organic polymers: halogen derivatives of polyacetylene, $(CH)_x$". In: *J. Chem. Soc., Chem. Commun.* (16 1977), pp. 578–580.

[6] C. W. Tang. "Two-layer organic photovoltaic cell". In: *Applied Physics Letters* 48.2 (1986), pp. 183–185.

[7] J. C. Hummelen et al. "Preparation and Characterization of Fulleroid and Methanofullerene Derivatives". In: *The Journal of Organic Chemistry* 60 (3 1995), pp. 532–538.

[8] G. Yu et al. "Polymer Photovoltaic Cells: Enhanced Efficiencies via Network of Internal Donor-Acceptor Heterojunctions". In: *Science* 270 (1995), pp. 1789–1791.

[9] L. Meng et al. "Organic and solution-processed tandem solar cells with 17.3% efficiency". In: 361.6407 (2018), pp. 1094–1098.

[10] A. Kojima et al. "Organometal Halide Perovskites as Visible- Light Sensitizers for Photovoltaic Cells". In: *J Am Chem Soc* 131 (2009), pp. 6050–6051.

[11] H.-S. Kim et al. "Lead Iodide Perovskite Sensitized All-Solid-State Submicron Thin Film Mesoscopic Solar Cell with Efficiency Exceeding 9%". In: *Scientific Reports* 2.591 (2012), pp. 1–7.

[12] *NREL Efficiency chart*. Accessed: 2019-01-30. 2018.

[13] P. Würfel. *Physics of Solar Cells*. Wiley-VCH, 2005.

[14] A. Köhler and H. Bässler. *Electronic Processes in Organic Semiconductors*. Vol. 1. 2015.

[15] L. Schmidt-Mende and J. Weickert. *Organic and Hybrid Solar Cells*. De Gruyter, 2016.

[16] U. Würfel, A. Cuevas, and P. Würfel. "Charge Carrier Separation in Solar Cells". In: *IEEE Journal of Photovoltaics* 5.1 (2015), pp. 461–469.

[17] C. J. Brabec et al. "Polymer-Fullerene Bulk-Heterojunction Solar Cells". In: *Adv. Mater.* 22.34 (2010), pp. 3839–3856.

[18] C. Deibel and V. Dyakonov. "Polymer-fullerene bulk heterojunction solar cells". In: *Reports Prog. Phys.* 73.9 (2010).

[19] C. Brabec, Ullrich Scherf, and Vladimir Dyakonov. *Organic Photovoltaics*. second. Wiley-VCH, 2014.

[20] C. Deibel, T. Strobe, and V. Dyakonov. "Role of the charge transfer state in organic donor-acceptor solar cells". In: *Adv. Mater.* 22.37 (2010), pp. 4097–4111.

[21] J. J.M. Halls et al. "Exciton diffusion and dissociation in a poly(p-phenylenevinylene)/C60 heterojunction photovoltaic cell". In: *Applied Physics Letters* 68.22 (1996), pp. 3120–3122.

[22] D. E. Markov et al. "Accurate Measurement of the Exciton Diffusion Length in a Conjugated Polymer using a Heterostructure with a Side-Chain Cross-Linked Fullerene Layer". In: *Journal of Physical Chemistry A* 109.24 (2005), pp. 5266–5274.

[23] X. Gong et al. "Bulk heterojunction solar cells with large open-circuit voltage: Electron transfer with small donor-acceptor energy offset". In: *Adv. Mater.* 23.20 (2011), pp. 2272–2277.

[24] J. Liu et al. "Fast charge separation in a non-fullerene organic solar cell with a small driving force". In: *Nat. Energy* 1.7 (2016), pp. 1–7.

[25] Z. Zhang et al. "Energy-level modulation of non-fullerene acceptors to achieve high-efficiency polymer solar cells at a diminished energy offset". In: *J. Mater. Chem. A* 5.20 (2017), pp. 9649–9654.

[26] A. Wagenpfahl et al. "S-shaped current-voltage characteristics of organic solar devices". In: *Phys. Rev. B - Condens. Matter Mater. Phys.* 82.11 (2010), pp. 1–8.

[27] Daniel Rauh et al. "Relation of open circuit voltage to charge carrier density in organic bulk heterojunction solar cells". In: *Appl. Phys. Lett.* 98.13 (2011).

[28] S. Wang, W. Yuan, and Y. S. Meng. "Spectrum-Dependent Spiro-OMeTAD Oxidization Mechanism in Perovskite Solar Cells". In: *ACS Appl. Mater. Interfaces* (2015), acsami.5b07703.

[29] H. Méndez et al. "Doping of organic semiconductors: Impact of dopant strength and electronic coupling". In: *Angewandte Chemie - International Edition* 52.30 (2013), pp. 7751–7755.

[30] I. Salzmann et al. “Intermolecular hybridization governs molecular electrical doping”. In: *Physical Review Letters* 108.3 (2012), pp. 1–5.

[31] I. Salzmann et al. “Molecular Electrical Doping of Organic Semiconductors: Fundamental Mechanisms and Emerging Dopant Design Rules”. In: *Accounts of Chemical Research* 49.3 (2016), pp. 370–378.

[32] J. Burschka. “High performance solid-state mesoscopic solar cells”. PhD thesis. 2013, p. 163.

[33] V. I. Arkhipov et al. “Charge carrier mobility in doped semiconducting polymers”. In: *App. Phys. Lett.* 82.19 (2003), pp. 3245–3247.

[34] H. J. Snaith and M. Grätzel. “Enhanced charge mobility in a molecular hole transporter via addition of redox inactive ionic dopant: Implication to dye-sensitized solar cells”. In: *App. Phys. Lett.* 89.26 (2006).

[35] P. Pingel, R. Schwarzl, and D. Neher. “Effect of molecular p-doping on hole density and mobility in poly(3-hexylthiophene)”. In: *Applied Physics Letters* 100.14 (2012), pp. 1–4.

[36] M. Saliba et al. “Cesium-containing triple cation perovskite solar cells: improved stability, reproducibility and high efficiency”. In: *Energy Environ. Sci.* 9.6 (2016), pp. 1989–1997.

[37] W. J. Yin, Tingting Shi, and Yanfa Yan. “Unique properties of halide perovskites as possible origins of the superior solar cell performance”. In: *Advanced Materials* 26.27 (2014), pp. 4653–4658.

[38] F. Brivio, Alison B. Walker, and Aron Walsh. “Structural and electronic properties of hybrid perovskites for high-efficiency thin-film photovoltaics from first-principles”. In: *APL Materials* 1.4 (2013).

[39] J. H. Noh et al. “Nanostructured $TiO_2/CH_3NH_3PbI_3$ heterojunction solar cells employing spiro-OMeTAD/Co-complex as hole-transporting material”. In: *J. Mater. Chem. A* 1.38 (2013), p. 11842.

[40] S. A. Kulkarni et al. “Band-gap tuning of lead halide perovskites using a sequential deposition process”. In: *Journal of Materials Chemistry A* 2.24 (2014), pp. 9221–9225.

[41] M. E. Kamminga et al. “Confinement Effects in Low-Dimensional Lead Iodide Perovskite Hybrids”. In: *Chemistry of Materials* 28.13 (2016), pp. 4554–4562.

[42] G. E. Eperon et al. “Formamidinium lead trihalide : a broadly tunable perovskite for efficient planar heterojunction solar”. In: *Energy & Environmental Science* 7 (2014), pp. 982–988.

[43] Kenichiro T. et al. “Comparative study on the excitons in lead-halide-based perovskite-type crystals CH3NH3PbBr3 CH3NH3PbI3”. In: *Solid State Communications* 127.9 (2003), pp. 619–623.

[44] V. D'Innocenzo et al. "Excitons Versus Free Charges in Organo-Lead Tri-Halide Perovskites". In: *Nature Communications* 5 (2014), pp. 1–6.

[45] T. J. Savenije et al. "Thermally activated exciton dissociation and recombination control the carrier dynamics in organometal halide perovskite". In: *Journal of Physical Chemistry Letters* 5.13 (2014), pp. 2189–2194.

[46] M Samiee et al. "Defect density and dielectric constant in perovskite solar cells". In: *Appl. Phys. Lett.* 105.153502 (2014), pp. 1–4.

[47] S. D Stranks et al. "Electron-Hole Diffusion Lengths Exceeding". In: *Science* 342.2013 (2013), pp. 341–344.

[48] G. W.P. Adhyaksa et al. "Carrier Diffusion Lengths in Hybrid Perovskites: Processing, Composition, Aging, and Surface Passivation Effects". In: *Chemistry of Materials* 28.15 (2016), pp. 5259–5263.

[49] Q. Dong et al. "Electron-hole diffusion lengths > 175 m m in solution-grown CH 3 NH 3 PbI 3 single crystals". In: *Science* 347.6225 (2015), pp. 967–970.

[50] F. Li et al. "Ambipolar solution-processed hybrid perovskite phototransistors". In: *Nature Communications* 6 (2015), pp. 1–8.

[51] J. You et al. "Moisture assisted perovskite film growth for high performance solar cells". In: *Applied Physics Letters* 105.18 (2014).

[52] P. Tiwana et al. "Electron mobility and injection dynamics in mesoporous ZnO, $SnO_2$, and $TiO_2$ films used in dye-sensitized solar cells". In: *ACS Nano* 5.6 (2011), pp. 5158–5166.

[53] L. Meng et al. "Recent Advances in the Inverted Planar Structure of Perovskite Solar Cells". In: *Accounts of Chemical Research* 49.1 (2016), pp. 155–165.

[54] S. Zhang et al. "Interface Engineering of Solution-Processed Hybrid Organohalide Perovskite Solar Cells". In: *ACS Applied Materials and Interfaces* 10.25 (2018), pp. 21681–21687.

[55] P. Docampo et al. "Lessons learned: From dye-sensitized solar cells to all-solid-state hybrid devices". In: *Advanced Materials* 26.24 (2014), pp. 4013–4030.

[56] F. Hou et al. "Efficient and stable planar heterojunction perovskite solar cells with an MoO3/PEDOT:PSS hole transporting layer". In: *Nanoscale* 7 (21 2015), pp. 9427–9432.

[57] J. C. Yu et al. "Highly efficient and stable inverted perovskite solar cell employing PEDOT:GO composite layer as a hole transport layer". In: *Scientific Reports* 8.1 (2018), p. 1070.

[58] C. Bi et al. "Non-wetting surface-driven high-aspect-ratio crystalline grain growth for efficient hybrid perovskite solar cells". In: *Nat. Commun.* 6 (2015), pp. 1–7.

[59] C. Xu, Zhihai Liu, and Eun Cheol Lee. "High-performance metal oxide-free inverted perovskite solar cells using poly(bis(4-phenyl)(2,4,6-trimethylphenyl)amine) as the hole transport layer". In: *Journal of Materials Chemistry C* 6.26 (2018), pp. 6975–6981.

[60] C. Bi et al. "Non-wetting surface-driven high-aspect-ratio crystalline grain growth for efficient hybrid perovskite solar cells". In: *Nature Communications* 6 (2015), pp. 1–7.

[61] M. Neophytou et al. "High mobility, hole transport materials for highly efficient PEDOT:PSS replacement in inverted perovskite solar cells". In: *J. Mater. Chem. C* 5 (20 2017), pp. 4940–4945.

[62] L. Kegelmann et al. "Mixtures of Dopant-Free Spiro-OMeTAD and Water-Free PEDOT as a Passivating Hole Contact in Perovskite Solar Cells". In: *ACS Appl. Mater. Interfaces* 11 (2019), pp. 9172–9181.

[63] E. L. Unger et al. "Hysteresis and transient behavior in current-voltage measurements of hybrid-perovskite absorber solar cells". In: *Energy and Environmental Science* 7.11 (2014), pp. 3690–3698.

[64] O. Almora et al. "Capacitive dark currents, hysteresis, and electrode polarization in lead halide perovskite solar cells". In: *Journal of Physical Chemistry Letters* 6.9 (2015), pp. 1645–1652.

[65] Y. Shao et al. "Origin and elimination of photocurrent hysteresis by fullerene passivation in $CH_3NH_3PbI_3$ planar heterojunction solar cells". In: *Nature Communications* 5 (2014), pp. 1–7.

[66] N. E. Courtier et al. "How transport layer properties affect perovskite solar cell performance: insights from a coupled charge transport/ion migration model". In: *Energy & Environmental Science* 12 (2019), pp. 396–409.

[67] J. Xu et al. "Perovskite-fullerene hybrid materials suppress hysteresis in planar diodes". In: *Nature Communications* 6.May (2015), pp. 1–8.

[68] H. S. Kim and N. G. Park. "Parameters affecting I-V hysteresis of CH3NH3PbI3perovskite solar cells: Effects of perovskite crystal size and mesoporous TiO2layer". In: *Journal of Physical Chemistry Letters* 5.17 (2014), pp. 2927–2934.

[69] L. Zheng et al. "Morphology control of the perovskite films for efficient solar cells". In: *Dalton Transactions* 44.23 (2015), pp. 10582–10593.

[70] T. S. Sherkar et al. "Recombination in Perovskite Solar Cells: Significance of Grain Boundaries, Interface Traps, and Defect Ions". In: *ACS Energy Letters* 2.5 (2017), pp. 1214–1222.

[71] F. Gerson and W. Huber. *Electron spin resonance spectroscopy of organic radicals*. Wiley-VCH, 2003.

[72] A.J. Hoff, ed. *Advanced EPR*. 1st ed. Elsevier Science, 1989.

[73] J. A. Weil and J. R. Bolton. *Electron Paramagnetic Resonance: Elementary Theory and Practical Applications*. second. Hoboken, New Jersey: Wiley & Sons, Inc., 1994.

[74] A. Schweiger and G. Jeschke. *Principles of Pulse Electron Paramagnetic Resonance*. Oxford University Press, 2001.

[75] M. Brustolon and E. Giamello. *Electron Paramagnetic Resonance*. John Wiley & Sons, Inc., 2009.

[76] G. R. Eaton et al. *Quantitative EPR*. Springer-Verlag/Wien, 2010.

[77] P. J. Mohr, D. B. Newell, and B. N. Taylor. "CODATA recommended values of the fundamental physical constants : 2014 *". In: 88.September (2016), pp. 1–73.

[78] J. M. Lupton and C. Boehme. "Magnetoresistance in organic semiconductors". In: *Nature Materials* 7.8 (2008), p. 598.

[79] G. Joshi et al. "High-Field Magnetoresistance of Organic Semiconductors". In: *Physical Review Applied* 10.2 (2018), p. 1.

[80] J. Even et al. "Importance of Spin-Orbit Coupling in Hybrid Organic/Inorganic Perovskites for Photovoltaic Applications". In: *Journal of Physical Chemistry Letters* 4.17 (2013), pp. 2999–3005.

[81] C. Zhang et al. "Magnetic field effects in hybrid perovskite devices". In: *Nature Physics* 11.5 (2015), pp. 427–434.

[82] S. Stoll and A. Schweiger. "EasySpin, a comprehensive software package for spectral simulation and analysis in EPR". In: *J. Magn. Reson.* 178.1 (2006), pp. 42–55.

[83] J. Behrends et al. "Direct Detection of Photoinduced Charge Transfer Complexes in Polymer:Fullerene Blends". In: *Phys. Rev. B* 125206 (2012), pp. 1–6.

[84] F. Kraffert et al. "Charge separation in PCPDTBT:PCBM blends from an EPR perspective". In: *J. Phys. Chem. C* 118.49 (2014), pp. 28482–28493.

[85] A. H. Devir-Wolfman et al. "Short-lived charge-transfer excitons in organic photovoltaic cells studied by high-field magneto-photocurrent". In: *Nature Communications* 5 (2014), pp. 1–7.

[86] N. J. Turro. "Influence of nuclear spin on chemical reactions: Magnetic isotope and magnetic field effects (A Review)". In: *Proceedings of the National Academy of Sciences* 80.2 (1982), pp. 609–621.

[87] D. Kaplan, I. Solomon, and N. F. Mott. "Explanation of the Large Spin-Dependent Recombination Effect in Semiconductors". In: *Journal der Physique Letters* 4.39 (1978), pp. 51–54.

[88] T. Eickelkamp, S. Roth, and M. Mehring. "Electrically detected magnetic resonance in photoexcited fullerenes". In: *Molecular Physics* 95.5 (1998), pp. 967–972.

[89] C. Boehme and Klaus Lips. "The Investigation of Charge Carrier Recombination and Hopping Transport with Pulsed Electrically Detected Magnetic Resonance Techniques". In: *Charge Transport in Disordered Solids*. Ed. by Sergei Baranovski. John Wiley & Sons, Ltd, 2006, pp. 179–218.

[90] T. W. Herring et al. "Experimental discrimination of geminate and non-geminate recombination in a-Si:H". In: *Physical Review B - Condensed Matter and Materials Physics* 79.19 (2009), pp. 1–5.

[91] G. Abowitz and E. Arnold. "Simple Mercury Drop Electrode for MOS Measurements". In: *Rev. Sci. Instrum.* 38 (1967), pp. 564–565.

[92] C. M. Wolff et al. "Reduced Interface-Mediated Recombination for High Open-Circuit Voltages in $CH_3NH_3PbI_3$ Solar Cells". In: *Advanced Materials* 29.28 (2017), pp. 1–8.

[93] *GitHub Spincounting Toolbox for Matlab*. Accessed: 2019-02-25.

[94] I. K. Ding et al. "Pore-filling of spiro-OMeTAD in solid-state dye sensitized solar cells: quantification, mechanism, and consequences for device performance". In: *Advanced Functional Materials* 19.15 (2009), pp. 2431–2436.

[95] S. Y. Lee et al. "Modulation frequency dependence of continuous-wave optically/electrically detected magnetic resonance". In: *Physical Review B - Condensed Matter and Materials Physics* 86.11 (2012), pp. 1–17.

[96] F. Neese. "The ORCA program system". In: *Wiley Interdiscip. Rev. Comput. Mol. Sci.* 2.1 (2012), pp. 73–78.

[97] *GitHub Libint: high-performance library for computing Gaussian integrals in quantum mechanics*. Accessed: 2019-03-06.

[98] D. Shi et al. "Spiro-OMeTAD single crystals: Remarkably enhanced charge-carrier transport via mesoscale ordering". In: *Sci. Adv.* 2.4 (2016), e1501491–e1501491.

[99] Y.-S. Lin et al. "Long-Range Corrected Hybrid Density Functionals with Improved Dispersion Corrections". In: *Journal of Chemical Theory and Computation* 9.1 (2013), pp. 263–272.

[100] S. Grimme et al. "A consistent and accurate ab initio parametrization of density functional dispersion correction (DFT-D) for the 94 elements H-Pu". In: *The Journal of Chemical Physics* 132.15 (2010), p. 154104.

[101] S. Grimme, S. Ehrlich, and L. Goerigk. "Effect of the damping function in dispersion corrected density functional theory". In: *Journal of Computational Chemistry* 32.7 (2011), pp. 1456–1465.

[102] V. Barone. *Recent Advances in Density Functional Methods, Part 1*. Singapore: World Scientific, 1995.

[103] N. J. Jeon et al. “Solvent engineering for high-performance inorganic–organic hybrid perovskite solar cells”. In: *Nat. Mater.* 13.9 (2014), pp. 897–903.

[104] J. Burschka et al. “Sequential deposition as a route to high-performance perovskite-sensitized solar cells”. In: *Nature* 499.7458 (2013), pp. 316–319.

[105] M. M. Lee et al. “Efficient Hybrid Solar Cells Based on Meso-Superstructured Organometal Halide Perovskites”. In: *Science* 338.6107 (2012), pp. 643–647.

[106] D. B. Mitzi. “Synthesis, Structure, and Properties of Organic-Inorganic Perovskites and Related Materials”. In: *Progress in Inorganic Chemistry*. Wiley-Blackwell, 2007, pp. 96–111.

[107] H. Zhou et al. “Interface engineering of highly efficient perovskite solar cells”. In: *Science* 345.6196 (July 2014), 542 LP –546.

[108] L. Kegelmann et al. “It Takes Two to Tango - Double-Layer Selective Contacts in Perovskite Solar Cells for Improved Device Performance and Reduced Hysteresis”. In: *ACS Appl. Mater. Interfaces* 9.20 (2017), pp. 17245–17255.

[109] D. Bi et al. “Polymer-templated nucleation and crystal growth of perovskite films for solar cells with efficiency greater than 21%”. In: 1 (Sept. 2016), p. 16142.

[110] Z. Hawash, L. K. Ono, and Y. Qi. “Recent Advances in Spiro-MeOTAD Hole Transport Material and Its Applications in Organic-Inorganic Halide Perovskite Solar Cells”. In: *Adv. Mater. Interfaces* 5 (2017), p. 1700623.

[111] D.-Yi. Chen et al. “Application of F4TCNQ doped spiro-MeOTAD in high performance solid state dye sensitized solar cells”. In: *Phys. Chem. Chem. Phys.* 14.33 (2012), p. 11689.

[112] A. Abate et al. “Lithium salts as "redox active" p-type dopants for organic semiconductors and their impact in solid-state dye-sensitized solar cells”. In: *Phys. Chem. Chem. Phys.* 15.7 (2013), p. 2572.

[113] W. H. Nguyen et al. “Enhancing the hole-conductivity of spiro-OMeTAD without oxygen or lithium salts by using spiro(TFSI)2 in perovskite and dye-sensitized solar cells”. In: *J. Am. Chem. Soc.* 136.31 (2014), pp. 10996–11001.

[114] M. Namatame et al. “Direct observation of dramatically enhanced hole formation in a perovskite-solar-cell material spiro-OMeTAD by Li-TFSI doping”. In: *Appl. Phys. Lett.* 110.12 (2017).

[115] J. Burschka et al. “Tris(2-(1 H -pyrazol-1-yl)pyridine)cobalt(III) as p-type dopant for organic semiconductors and its application in highly efficient solid-state dye-sensitized solar cells”. In: *J. Am. Chem. Soc.* 133.45 (2011), pp. 18042–18045.

[116] T. Matsui et al. "Room-Temperature Formation of Highly Crystalline Multication Perovskites for Efficient, Low-Cost Solar Cells". In: *Advanced Materials* 29 (2017), pp. 2–6.

[117] R. Schölin et al. "Energy level shifts in spiro-OMeTAD molecular thin films when adding Li-TFSI". In: *Journal of Physical Chemistry C* 116.50 (2012), pp. 26300–26305.

[118] P. Pingel et al. "P-Type Doping of Poly(3-hexylthiophene) with the Strong Lewis Acid Tris(pentafluorophenyl)borane". In: *Adv. Electron. Mater.* 2.10 (2016), pp. 1–7.

[119] A. Sperlich et al. "Reversible and irreversible interactions of poly(3-hexylthiophene) with oxygen studied by spin-sensitive methods". In: *J. Phys. Chem. B* 115.46 (2011), pp. 13513–13518.

[120] D. K. Susarova et al. "ESR spectroscopy as a powerful tool for probing the quality of conjugated polymers designed for photovoltaic applications". In: *Chem. Commun.* 51.12 (2015), pp. 2239–2241.

[121] H. J. Snaith and M. Grätzel. "Enhanced charge mobility in a molecular hole transporter via addition of redox inactive ionic dopant: Implication to dye-sensitized solar cells". In: *Applied Physics Letters* 89.26 (2006), p. 262114.

[122] H. J. Snaith and Michael Grätzel. "Electron and hole transport through mesoporous TiO2 infiltrated with spiro-MeOTAD". In: *Adv. Mater.* 19.21 (2007), pp. 3643–3647.

[123] V. I. Arkhipov et al. "Effect of doping on the density-of-states distribution and carrier hopping in disordered organic semiconductors". In: *Phys. Rev. B* 71 (4 Jan. 2005), p. 045214.

[124] L. Yang et al. "Initial light soaking treatment enables hole transport material to outperform spiro-OMeTAD in solid-state dye-sensitized solar cells". In: *J. Am. Chem. Soc.* 135.19 (2013), pp. 7378–7385.

[125] A. Abrusci et al. "Influence of ion induced local Coulomb field and polarity on charge generation and efficiency in poly(3-hexylthiophene)-based solid-state dye-sensitized solar cells". In: *Adv. Funct. Mater.* 21.13 (2011), pp. 2571–2579.

[126] F. Giordano et al. "Enhanced electronic properties in mesoporous TiO2 via lithium doping for high-efficiency perovskite solar cells". In: *Nat. Comm.* 7.10379 (2016), pp. 1–6.

[127] J. M. Holland et al. "Steric effects on the electronic and molecular structures of nickel(II) and cobalt(II) 2,6-dipyrazol-1-ylpyridine complexes". In: *Polyhedron* 20 (2001), pp. 2829–2840.

[128] A. Abragam and B. Bleaney. *Electron Paramagnetic Resonance of Transition Ions*. Clarendon Press, Oxford, 1970.

[129] Y. Li et al. “Characterization of intrinsic hole transport in single-crystal spiro-OMeTAD”. In: *npj Flex. Electron.* 1.1 (2017), p. 2.

[130] J. J.M. Halls et al. “Efficient photodiodes from interpenetrating polymer networks”. In: *Nature* 376.6540 (1995), pp. 498–500.

[131] S. H. Park et al. “Bulk heterojunction solar cells with internal quantum efficiency approaching 100%”. In: *Nat. Photonics* 3.5 (2009), pp. 297–303.

[132] M. C. Scharber and N. S. Sariciftci. “Efficiency of bulk-heterojunction organic solar cells”. In: *Prog. Polym. Sci.* 38.12 (2013), pp. 1929–1940.

[133] L. Ye et al. “Toward efficient non-fullerene polymer solar cells: Selection of donor polymers”. In: *Org. Electron. physics, Mater. Appl.* 17 (2015), pp. 295–303.

[134] S. J. Lou et al. “Effects of additives on the morphology of solution phase aggregates formed by active layer components of high-efficiency organic solar cells”. In: *J. Am. Chem. Soc.* 133.51 (2011), pp. 20661–20663.

[135] S. Holliday et al. “High-efficiency and air-stable P3HT-based polymer solar cells with a new non-fullerene acceptor”. In: *Nat. Commun.* 7 (2016), pp. 1–11.

[136] D. R. McCamey et al. “Spin Rabi flopping in the photocurrent of a polymer light-emitting diode”. In: *Nat. Mater.* 7.9 (2008), pp. 723–728.

[137] J. Behrends et al. “Bipolaron formation in organic solar cells observed by pulsed electrically detected magnetic resonance”. In: *Phys. Rev. Lett.* 105.17 (2010), pp. 12–15.

[138] D. R. McCamey et al. “Hyperfine-field-mediated spin beating in electrostatically bound charge carrier pairs”. In: *Phys. Rev. Lett.* 104.1 (2010), pp. 1–4.

[139] A. J. Kupijai et al. “Bipolar polaron pair recombination in polymer/fullerene solar cells”. In: *Phys. Rev. B* 92.24 (2015), pp. 1–8.

[140] K. J. Van Schooten et al. “Probing long-range carrier-pair spin-spin interactions in a conjugated polymer by detuning of electrically detected spin beating”. In: *Nat. Commun.* 6 (2015), pp. 1–9.

[141] W. Harneit et al. “Room temperature electrical detection of spin coherence in C60”. In: *Phys. Rev. Lett.* 98.21 (2007), pp. 1–4.

[142] J. Behrends et al. “Persistent spin coherence and bipolarons”. In: *Nat. Nanotechnol.* 8.12 (2013), pp. 884–885.

[143] C. Boehme and J. M. Lupton. “Challenges for organic spintronics”. In: *Nat. Nanotechnol.* 8.9 (2013), pp. 612–615.

[144] I. Solomon. “Spin-dependent recombination in a silicon p-n junction”. In: *Solid State Communications* 20 (1976), pp. 215–217.

[145] M. Eckardt. "Electrically Detected Magnetic Resonance on Fullerene-Based Organic Semiconductor Devices and Microcrystals". PhD thesis. 2016, p. 123.

[146] F. Kraffert et al. "Transport-related triplet states and hyperfine couplings in organic tandem solar cells probed by pulsed electrically detected magnetic resonance spectroscopy". In: *J. Magn. Reson.* 282 (2017), pp. 10–17.

[147] F. Kraffert et al. "Transient electrically detected magnetic resonance spectroscopy applied to organic solar cells". In: *Appl. Phys. Lett.* 107.4 (2015).

[148] N. Sariciftci et al. "Photoinduced Electron Transfer from a Conducting Polymer to Buckminsterfullerene." In: *Science.* 258.November (1992), pp. 1474–1476.

[149] B. Y. Finck and B. J. Schwartz. "Understanding the origin of the S-curve in conjugated polymer/fullerene photovoltaics from drift-diffusion simulations". In: *Appl. Phys. Lett.* 103.5 (2013).

[150] J. Niklas et al. "Highly-efficient charge separation and polaron delocalization in polymer-fullerene bulk-heterojunctions: a comparative multi-frequency EPR and DFT study". In: *Phys. Chem. Chem. Phys.* 15 (2013), pp. 9562–9574.

[151] E. L. Frankevich et al. "Polaron-pair generation in poly(phenylene vinylenes)". In: *Phys. Rev. B* 46.15 (1992), pp. 9320–9324.

[152] P. A. Bobbert et al. "Bipolaron mechanism for organic magnetoresistance". In: *Phys. Rev. Lett.* 99.21 (2007), pp. 1–4.

[153] J. De Ceuster et al. "High-frequency (95 GHz) electron paramagnetic resonance study of the photoinduced charge transfer in conjugated polymer-fullerene composites". In: *Phys. Rev. B* 64.19 (2001), pp. 17–19.

[154] P. Odenthal et al. "Spin-polarized exciton quantum beating in hybrid organic-inorganic perovskites". In: *Nature Physics* 13.9 (2017), pp. 894–899.

[155] Y. C. Hsiao et al. "Magneto-optical studies on spin-dependent charge recombination and dissociation in perovskite solar cells". In: *Adv. Mater.* 27.18 (2015), pp. 2899–2906.

[156] J. Zhang et al. "Exploring spin-orbital coupling effects on photovoltaic actions in Sn and Pb based perovskite solar cells". In: *Nano Energy* 38.May (2017), pp. 297–303.

[157] B. Zhao et al. "High Open-Circuit Voltages in Tin-Rich Low-Bandgap Perovskite-Based Planar Heterojunction Photovoltaics". In: *Adv. Mater.* 29.2 (2017).

[158] G. Kapil et al. "Highly Efficient 17.6% Tin-Lead Mixed Perovskite Solar Cells Realized through Spike Structure". In: *Nano Lett.* 18.6 (2018), pp. 3600–3607.

[159] C. Uhrich et al. “Origin of open circuit voltage in planar and bulk heterojunction organic thin-film photovoltaics depending on doped transport layers thin-film photovoltaics depending on doped transport layers”. In: *Journal of Applied Physics* 104 (2008), p. 043107.

[160] Chong Liu et al. “Highly Efficient Perovskite Solar Cells with Substantial Reduction of Lead Content”. In: *Sci. Rep.* 6 (2016), pp. 1–8.

[161] A. Elschner et al. *PEDOT: Principles and Applications of Intrinsically Conductive Polymer*. Taylor & Francis, 2011.

[162] V. S. Pavlovich Shpilevsky and E. M. “Journal of Applied Spectroscopy, Vol. 77, No. 3, 2010”. In: *J. Appl. Spectrosc.* 77.3 (2010), pp. 335–342.

[163] J. Niklas, K. L. Mardis, and O. G. Poluektov. “Spin Signature of the $C_{60}$ Fullerene Anion: A Combined X- and D-Band EPR and DFT Study”. In: *The Journal of Physical Chemistry Letters* 9 (2018), pp. 3915–3921.

[164] J. Stinchcombe et al. “Buckminsterfulleride(1-) Salts: Synthesis, EPR, and the Jahn-Teller Distortion of $C_{60}^{-}$”. In: *J. Am. Chem. Soc.* 115.12 (1993), pp. 5212–5217.

[165] W. Bietsch et al. “Jahn-Teller distortion and merohedral disorder of $C_{60}^{-}$ as observed by ESR”. In: *Chem. Phys. Lett.* 324.1-3 (2000), pp. 37–42.

[166] A. Zykwinska et al. “In situ EPR spectroelectrochemical studies of paramagnetic centres in poly(3,4-ethylenedioxythiophene) (PEDOT) and poly(3,4-butylenedioxythiophene) (PBuDOT) films”. In: *Chem. Phys.* 292.1 (2003), pp. 31–45.

[167] T. Kato. “Absorption and Emission Spectra for $C_{60}$ Anions”. In: *Laser Chem.* 14.C (1994), pp. 155–160.

[168] Angelo Alberti, Laura Favaretto, and Giancarlo Seconi. “Radical Cations and Anions from Some Simple Polythiophenes: an ESR Investigation”. In: *J. Chem. Soc. Perkin Trans.* 2 (1990).

[169] R. Younts et al. “Efficient Generation of Long-Lived Triplet Excitons in 2D Hybrid Perovskite”. In: *Advanced Materials* 29.9 (2017), pp. 1–7.

[170] D. Sapori et al. “Quantum confinement and dielectric profiles of colloidal nanoplatelets of halide inorganic and hybrid organic–inorganic perovskites”. In: *Nanoscale* 8 (12 2016), pp. 6369–6378.

[171] L. Ma et al. “Singlet fission in rubrene single crystal: Direct observation by femtosecond pump-probe spectroscopy”. In: *Phys. Chem. Chem. Phys.* 14.23 (2012), pp. 8307–8312.

[172] G. B. Piland et al. “Magnetic field effects on singlet fission and fluorescence decay dynamics in amorphous rubrene”. In: *J. Phys. Chem. C* 117.3 (2013), pp. 1224–1236.

[173] M. Witwicki et al. “Influence of Pb(II) ions on the EPR properties of the semiquinone radicals of humic acids and model compounds: High field EPR and relativistic DFT studies”. In: *J. Phys. Chem. A* 113.51 (2009), pp. 14115–14122.

[174] V. P. Solntsev et al. “EPR study of coordination of Ag and Pb cations in BaB2 O4 crystals and barium borate glasses”. In: *Phys. Chem. Miner.* 35.6 (2008), pp. 311–320.

[175] I. Shkrob and T. W. Marin. “Charge trapping in photovoltaically active perovskites and related halogenoplumbate compounds”. In: *J. Phys. Chem. Lett.* 5.7 (2014), pp. 1066–1071.

[176] F. Zheng et al. “Rashba spin-orbit coupling enhanced carrier lifetime in CH3NH3PbI3”. In: *Nano Letters* 15.12 (2015), pp. 7794–7800.

[177] T. Etienne, E. Mosconi, and F. De Angelis. “Dynamical Origin of the Rashba Effect in Organohalide Lead Perovskites: A Key to Suppressed Carrier Recombination in Perovskite Solar Cells?” In: *J. Phys. Chem. Lett.* 7.9 (2016), pp. 1638–1645.

[178] J. Zhao et al. “Strained hybrid perovskite thin films and their impact on the intrinsic stability of perovskite solar cells”. In: *Sci. Adv.* 3.11 (2017), eaao5616.

[179] G. Feher, J. C. Hensel, and E. A. Gere. “Paramagnetic resonance absorption from acceptors in silicon”. In: *Phys. Rev. Lett.* 5.7 (1960), pp. 309–311.

[180] A. R. Stegner et al. “Isotope effect on electron paramagnetic resonance of boron acceptors in silicon”. In: *Phys. Rev. B - Condens. Matter Mater. Phys.* 82.11 (2010), pp. 1–11.

[181] T. Wang et al. “Indirect to direct bandgap transition in methylammonium lead halide perovskite”. In: *Energy Environ. Sci.* 10.2 (2017), pp. 509–515.

[182] D. P. McMeekin et al. “Crystallization Kinetics and Morphology Control of Formamidinium–Cesium Mixed-Cation Lead Mixed-Halide Perovskite via Tunability of the Colloidal Precursor Solution”. In: *Adv. Mater.* 29.29 (2017).

[183] C. Zhu et al. “Strain engineering in perovskite solar cells and its impacts on carrier dynamics”. In: *Nat. Commun.* 10.1 (2019).

[184] T. W. Jones et al. “Lattice strain causes non-radiative losses in halide perovskites”. In: *Energy Environ. Sci.* 12.2 (2019), pp. 596–606.

[185] H. Neubrand. “ESR from boron in silicon at zero and small external stress. I. Line Positions and Line Structure”. In: *Phys. Status Solidi* 86.1 (1978), pp. 269–275.

[186] H. Neubrand. “ESR from boron in silicon at zero and small external stress. II. Linewidth and crystal defects”. In: *Phys. Status Solidi* 90.1 (1978), pp. 301–308.

# Conference Contributions

1. Ula Yasin, Felix Kraffert, Robert Steyrleuthner, and Jan Behrends. *Investigating Spin-Dependent Transport in Perovskite Solar Cells with EDMR.* SPP1601-Young Researchers Workshop, Konstanz, Germany, 2016, **poster and talk**.

2. Ula Yasin, Felix Kraffert, and Jan Behrends. *Bias Dependence of Transient EDMR Signals from Organic Solar Cells.* Spin Chemistry Meeting 2017, Schluchsee, Germany, 2017, **poster** (poster prize winner).

3. Ula Yasin, Claudia Tait, Lukas Kegelmann, Felix Kraffert, Robert Steyrleuthner, Steve Albrecht, and Jan Behrends. *Quantitative EPR Analysis of Doped Spiro-OMeTAD.* $11^{\text{th}}$ International Conference on Hybrid and Organic Photovoltaics, Rome, Italy, 2019, **poster**.

4. Ula Yasin, Felix Kraffert, and Jan Behrends. *Bias Dependence of Transient EDMR Signals from Organic Solar Cells.* $14^{\text{th}}$ International Symposium on Functional $\pi$-Electron Systems, Berlin, Germany, 2019, **poster**.

# Acknowledgements

This thesis would have not been possible without the contribution of many people and helping hands.

First and foremost, I would like to thank my supervisor Jan Behrends for giving me the chance to realize my doctoral thesis in his group. You've introduced me to the intriguing field of photovoltaics and encouraged me at various stages of my studies. You've always given me the freedom to find my research path and guided me through the struggles. Your expertise is invaluable for successfully completing this thesis.

I thank Bernd Rech for agreeing to be second supervisor on this thesis.

A special thanks to Robert Bittl. I still remember the day I started as a bachelor student in your working group. It has opened many doors for me ever since. The valuable discussions and constructive criticism have contributed immensely to my scientific knowledge.

A warm thank you to all members of AG Bittl and AG Behrends for the fun and pleasant working environment. I'm grateful for all my former and current office colleagues for the wonderful time we shared, as well as Christian T., Johann, Kelvin, Thomas, Ilia, Daria, and Naitik who accompanied me through this journey.

I especially would like to thank Felix Kraffert for the generous time spent helping out in the lab, his support and advice in realization of experiments, as well as his assistance in formulating the research topics. Together with Jan, he has guided me through my projects. Moreover, thanks to Robert Steyrleuthner for imparting his valuable knowledge on organic semiconductors and always taking the time to consult me and show me the ropes. I am very much thankful to Claudia Tait for all the brilliant input that helped shape this work, and for always lending a helping hand. No matter what the problem was, you always knew how to fix it. You are an inspiration to me.

I would also like to acknowledge my colleagues at the HZB. Special thanks to Steve Albrecht and the fruitful collaboration. His innovative mind set has motivated me to not give up on perovskites just yet. Thanks to Christian Wolff, Aboma Merdasa and Lukas Kegelmann, for our numerous scientific discussions and of course for providing

happy distractions outside the lab. I would also like to extend my deepest gratitude to Rowan McQueen for his insightful input, all the brainstorming sessions, and his support during long lab days trying to figure out the mystery behind perovskites.

I humbly extend my thanks to Sama and Andreas. You didn't have a choice but to join me on this roller coaster ride. You've showed me nothing but unconditional support and I'm extremely grateful for having you in my life. Finally, I want to express my gratitude to Nabil and Eman. I am deeply indebted with you and I wouldn't have come this far without you. You've showed me that the sky is the limit.

# Declaration of Authorship

I hereby declare that I have completed the presented work independently and that I have not used any sources other than those listed and identified as references. Furthermore, I confirm that this thesis has not been submitted, either whole or in part, to any other examination committee and has not been published elsewhere.

Ich erkläre hiermit, dass ich die vorliegende Arbeit selbständig und nur unter Verwendung der aufgelisteten und als Referenz identifizierten Literatur angefertigt habe. Darüber hinaus erkläre ich, dass ich die Arbeit in keinen anderen Promotionsverfahren eingereicht habe oder hatte.

Berlin, den 29. November 2019 .....